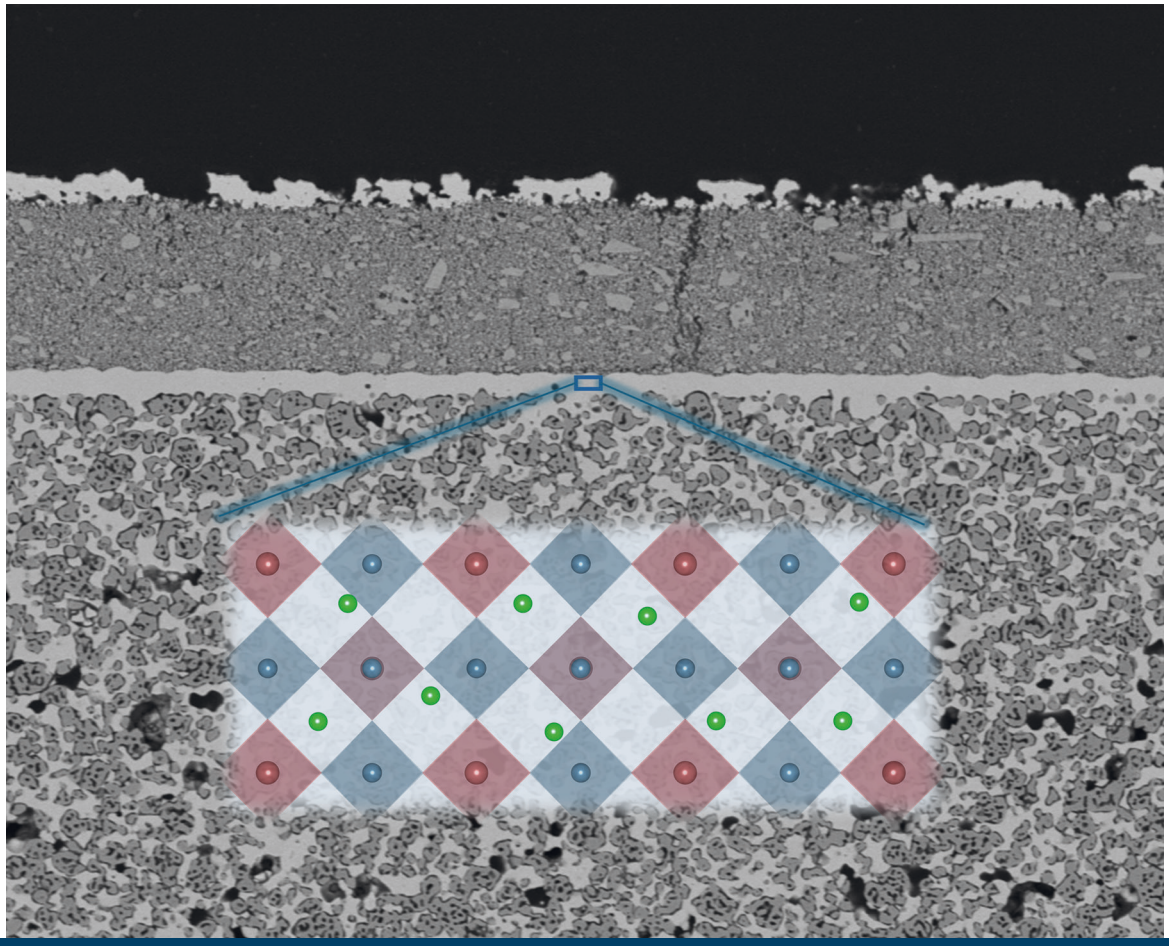

Materials Design, Processing and Application of Proton-Conducting Oxides for Electrochemical Energy Conversion

Yuan Zeng

Energie & Umwelt / Energy & Environment
Band / Volume 700
ISBN 978-3-95806-899-5

Mitglied der Helmholtz-Gemeinschaft

JÜLICH
Forschungszentrum

Schriften des Forschungszentrums Jülich
Reihe Energie & Umwelt / Energy & Environment Band / Volume 700

Forschungszentrum Jülich GmbH
Institute of Energy Materials and Devices (IMD)
Werkstoffsynthese und Herstellungsverfahren (IMD-2)

Materials Design, Processing and Application of Proton-Conducting Oxides for Electrochemical Energy Conversion

Yuan Zeng

Schriften des Forschungszentrums Jülich
Reihe Energie & Umwelt / Energy & Environment Band / Volume 700

ISSN 1866-1793 ISBN 978-3-95806-899-5

Bibliografische Information der Deutschen Nationalbibliothek.
Die Deutsche Nationalbibliothek verzeichnet diese Publikation in der
Deutschen Nationalbibliografie; detaillierte Bibliografische Daten
sind im Internet über http://dnb.d-nb.de abrufbar.

Herausgeber und Vertrieb:	Forschungszentrum Jülich GmbH Zentralbibliothek, Verlag 52425 Jülich Tel.: +49 2461 61-5368 Fax: +49 2461 61-6103 zb-publikation@fz-juelich.de www.fz-juelich.de/zb
Umschlaggestaltung:	Grafische Medien, Forschungszentrum Jülich GmbH
Druck:	Grafische Medien, Forschungszentrum Jülich GmbH
Copyright:	Forschungszentrum Jülich 2026

Schriften des Forschungszentrums Jülich
Reihe Energie & Umwelt / Energy & Environment, Band / Volume 700

D 82 (Diss. RWTH Aachen University, 2026)

ISSN 1866-1793
ISBN 978-3-95806-899-5

Vollständig frei verfügbar über das Publikationsportal des Forschungszentrums Jülich (JuSER)
unter www.fz-juelich.de/zb/openaccess.

Abstract

The growing demand for renewable energy and the need for efficient energy conversion technologies have spurred significant interest in solid oxide cells (SOCs). Recently, proton-conducting ceramic cells (PCCs) have gained considerable attention due to their potential to operate at lower temperatures than oxygen-ion-conducting SOCs. However, their widespread adoption faces challenges related to material stability, mechanical integrity, electrolyte densification, and fabrication compatibility. This dissertation seeks to overcome these challenges through a systematic investigation, from material design to fabrication, aimed at developing mechanically robust and high-performance PCCs. The results are presented in four main sections:

First, a systematic study was conducted on $BaZr_{0.8-x}Ce_{0.2}Y_xO_{3-\delta}$ (BZCY, x = 0.1–0.3) proton conductors, targeting high Zr/Ce ratios for enhanced thermochemical stability. The effect of Y substitution on phase formation, grain boundary characteristics, proton conductivity, and hydration behavior was evaluated. Electrochemical impedance spectroscopy revealed that proton mobility in the bulk remained nearly constant for Y ≤ 25%, indicating a complex interplay between Y-trapping and percolation effects. Meanwhile, grain boundary conductivity was enhanced through Y segregation, supporting the space charge layer model. A substitution level of 20 at% Y was found to be optimal, maximizing conductivity by promoting both bulk and grain boundary proton transport while avoiding secondary phase formation due to solubility saturation.

Second, the mechanical performance of BZCY/NiO fuel electrode supports was analyzed across different sintering and reduction conditions. Ring-on-ring testing, SEM-based fractography, and Weibull statistics demonstrated that sintering temperature and NiO-to-Ni reduction strongly influenced the porosity, flaw population, and ultimately the mechanical strength. Compared to YSZ/NiO composites, BZCY-based supports showed lower strength, underscoring the need for improved structural design for large-area PCCs applications.

Third, to address the fabrication of thin electrolyte layers, a binder-free wet powder spraying (WPS) method was developed using ethanol-based suspensions without organic additives. By reducing the solid content and spraying rate, individual wet layers were dried between successive passes, minimizing tensile stress and preventing crack formation. Systematic optimization of solid content, particle size distribution, and spray distance led to the successful deposition of crack-free electrolyte films. This work proved that WPS can be a scalable and cost-effective method for effectively fabricating thin electrolyte for large scale PCCs.

Finally, co-sintering of the thin electrolyte with different fuel electrode substrates was investigated, revealing critical correlations between substrate shrinkage behavior, Ba evaporation, and electrolyte densification. Zr-rich Ba-based substrates with poor shrinkage failed to retain Ba during sintering, leading to secondary phase formation and incomplete densification. While Ce rich Ba-based substrate demonstrated more substantial shrinkage before Ba evaporation occurred, greatly facilitating electrolyte densification. Meanwhile, Sr-based fuel electrodes introduced Sr diffusion that partially compensated for Ba loss and promoted sintering at lower temperatures. By leveraging an optimized wet powder spraying process to deposit an uniform, ultra-thin electrolyte layer and applying insights from half-cell co-sintering studies, gas-tight half-cells with an electrolyte thickness below 3 µm were successfully fabricated. The best fabricated full cell with Ce-rich fuel electrode exhibited power densities exceeding 1000 $mW \cdot cm^{-2}$ at 600 °C and 0.7 V in fuel cell mode, along with a current density of 2911 mA/cm^2 at an applied voltage of 1.3 V in electrolysis mode.

In summary, this work not only contributes new insights into the structure-processing-property relationships of Ba-based proton conductors but also establishes scalable fabrication routes and innovative design strategies for next-generation protonic ceramic devices. The demonstrated combination of advanced processing techniques with fundamental materials understanding paves the way for large-scale deployment of these technologies in renewable energy conversion and storage systems.

Kurzfassung

Der wachsende Bedarf an erneuerbaren Energien und die Notwendigkeit effizienter Energiewandlungstechnologien haben das Interesse an Festoxid-Zellen (SOCs) erheblich gesteigert. In jüngster Zeit haben protonenleitende keramische Zellen (PCCs) aufgrund ihres Potenzials, bei niedrigeren Temperaturen als sauerstoffionenleitende SOCs zu arbeiten, große Aufmerksamkeit erlangt. Ihre weitverbreitete Anwendung steht jedoch vor Herausforderungen in Bezug auf Materialstabilität, mechanische Integrität, Elektrolytverdichtung und Fertigungskompatibilität. Diese Dissertation zielt darauf ab, diese Herausforderungen durch eine systematische Untersuchung von der Materialentwicklung bis zur Herstellung zu überwinden, mit dem Ziel, mechanisch robuste und leistungsstarke PCCs zu entwickeln. Die Ergebnisse werden in vier Hauptabschnitten dargestellt:

Erstens wurde eine systematische Untersuchung an $BaZr_{0.8-x}Ce_{0.2}Y_xO_{3-\delta}$ (BZCY, x = 0.1–0.3) Protonenleitern durchgeführt, wobei hohe Zr/Ce-Verhältnisse zur Verbesserung der thermochemischen Stabilität angestrebt wurden. Der Einfluss der Y-Substitution auf Phasenbildung, Korngrenzeneigenschaften, Protonenleitfähigkeit und Hydratationsverhalten wurde bewertet. Die elektrochemische Impedanzspektroskopie zeigte, dass die Protonenbeweglichkeit im Volumen für Y ≤ 25 % nahezu konstant blieb, was auf ein komplexes Zusammenspiel zwischen Y-Bindung und Perkolation hinweist. Gleichzeitig wurde die Korngrenzenleitfähigkeit durch Y-Anreicherung erhöht, was das Modell der Raumladungszone unterstützt. Ein Substitutionsgrad von 20 at% Y erwies sich als optimal, da er sowohl den Protonentransport im Volumen als auch an den Korngrenzen förderte und gleichzeitig die Bildung von Sekundärphasen durch Löslichkeitsübersättigung vermied.

Zweitens wurde die mechanische Leistung von BZCY/NiO-Brennstoffelektroden-Trägern unter verschiedenen Sinter- und Reduktionsbedingungen analysiert. Ring-auf-Ring-Prüfungen, REM-gestützte Bruchflächenanalyse und Weibull-Statistik zeigten, dass Sintertemperatur und die NiO-zu-Ni-Reduktion die Porosität, Fehlstellenverteilung und letztlich die mechanische Festigkeit stark beeinflussten. Im Vergleich zu YSZ/NiO-Verbundwerkstoffen zeigten BZCY-basierte Träger eine geringere Festigkeit, was die Notwendigkeit einer verbesserten Strukturgestaltung für Anwendungen mit großflächigen PCCs unterstreicht.

Drittens wurde zur Herstellung dünner Elektrolytschichten ein bindemittelfreies Nasspulverspritzverfahren (WPS) entwickelt, das ethanolbasierte Suspensionen ohne organische Zusatzstoffe verwendet. Durch die Reduzierung des Feststoffgehalts und der Sprührate sowie das Zwischentrocknen einzelner nasser Schichten zwischen den Sprühdurchgängen konnten Zugspannungen minimiert und Rissbildungen vermieden werden. Die systematische Optimierung von Feststoffgehalt, Partikelgrößenverteilung und Sprühabstand führte zur erfolgreichen Abscheidung

rissfreier Elektrolytfilme. Diese Arbeit zeigte, dass WPS eine skalierbare und kosteneffiziente Methode zur effektiven Herstellung dünner Elektrolyte für großflächige PCCs darstellt.

Schließlich wurde das Kosintern des dünnen Elektrolyten mit unterschiedlichen Brennstoffelektroden-Substraten untersucht, wodurch entscheidende Zusammenhänge zwischen dem Schwindungsverhalten des Substrats, der Ba-Verdampfung und der Elektrolytverdichtung aufgedeckt wurden. Zr-reiche, Ba-basierte Substrate mit geringer Schrumpfung konnten während des Sinterns kein Ba zurückhalten, was zur Bildung von Sekundärphasen und unvollständiger Verdichtung führte. Ce-reiche, Ba-basierte Substrate zeigten hingegen ein stärkeres Schrumpfen, bevor Ba-Verdampfung eintrat, was die Elektrolytverdichtung erheblich erleichterte. Sr-basierte Brennstoffelektroden führten zu einer Sr-Diffusion, die den Ba-Verlust teilweise ausglich und das Sintern bei niedrigeren Temperaturen förderte. Durch die Anwendung eines optimierten Nasspulverspritzverfahrens zur Abscheidung einer gleichmäßigen, ultradünnen Elektrolytschicht und die Nutzung der Erkenntnisse aus Kosinteruntersuchungen von Halbzellen konnten gasdichte Halbzellen mit einer Elektrolytdicke von unter 3 µm erfolgreich hergestellt werden. Die beste gefertigte Vollzelle mit Ce-reicher Brennstoffelektrode erreichte Leistungsdichten von über 1000 $mW \cdot cm^{-2}$ bei 600 °C und 0,7 V im Brennstoffzellenbetrieb sowie eine Stromdichte von 2911 $mA\ cm^{-2}$ bei einer angelegten Spannung von 1,3 V im Elektrolysebetrieb.

Zusammenfassend trägt diese Arbeit nicht nur zu neuen Erkenntnissen über die Struktur-Verarbeitungs-Eigenschafts-Beziehungen von Ba-basierten Protonenleitern bei, sondern etabliert auch skalierbare Herstellungsverfahren und innovative Designstrategien für Protonenkeramik-Bauteile der nächsten Generation. Die gezeigte Kombination aus fortschrittlichen Verarbeitungstechniken und grundlegendem Materialverständnis ebnet den Weg für die großtechnische Einführung dieser Technologien in Systemen zur Umwandlung und Speicherung erneuerbarer Energien.

Table of contents

1 Introduction and Objectives

The ever-growing global demand for energy has significantly accelerated the consumption of fossil fuels, which, in turn, has led to a range of serious environmental issues. In response, countries worldwide are actively working to increase the share of renewable energy in their energy portfolios [1–3]. Renewable energy sources such as solar, wind, and hydro are promising, but their intermittent nature and geographical dependence limit their ability to provide a stable and continuous energy supply. In contrast, hydrogen, which can be generated through various methods, is a storable and transportable energy carrier, making it a highly attractive option. Among these, hydrogen produced from renewable sources is considered the cleanest fuel available. Realizing a hydrogen-based energy economy, however, requires efficient technologies for converting energy between hydrogen and electricity.

Solid oxide cells (SOCs), which function as reversible electrochemical devices, either operating as fuel cells (converting hydrogen to electricity) or as electrolysis cells (converting electricity to hydrogen), have emerged as a promising solution for this energy conversion challenge [4–9].

In particular, proton-conducting ceramic cells (PCCs) have garnered increasing attention in the past decade [10–16]. Compared to oxygen-ion-conducting SOCs, PCCs exhibit higher ionic conductivity in the intermediate to high temperature range (400-600 °C). Moreover, owing to their distinct electrochemical mechanisms, PCCs offer several operational advantages, such as water formation occurring at the air electrode side, which prevents dilution of the H_2. Despite these benefits, PCCs remain at a relatively low technology readiness level. Their path to commercialization is hindered by several critical challenges, including material instability, mechanical weaknesses, fabrication difficulties, low Faradaic efficiency and so on.

This dissertation aims to contribute to the development of high-performance PCCs, beginning with a fundamental investigation of proton-conducting oxide materials. The key objectives and structure of the research are as follows:

- In-depth characterization of the $BaZr_{0.8-x}Ce_{0.2}Y_xO_{3-\delta}$ system, focusing on the role of the dopant Y on various material properties including phase composition, sinterability, microstructure, hydration behavior, proton conductivity, and mechanical strength. This study provides insight into the defect chemistry and transport properties of proton-conducting oxides, expands the material landscape, and identifies the optimal Y-doping level for enhanced performance.
- Evaluation of the mechanical properties of fuel electrode supports, which serve as the structural backbone of the full cell. This section investigates how varying the sintering temperature influences porosity and mechanical performance. Fractographic analysis is conducted to

understand failure mechanisms, offering insights into the mechanical limitations of PCCs and proposing strategies for improvement.

- Fabrication of ultrathin proton-conducting electrolyte layers, aiming to reduce the ohmic resistance of the full cell. A wet powder spraying method is adopted and optimized to achieve uniform, crack-free electrolyte coatings after drying, laying the foundation for successful co-sintering.
- Investigation of co-sintering mechanisms between the electrolyte and various types of fuel electrodes, with a focus on $BaZr_{0.65}Ce_{0.2}Y_{0.15}O_{3-\delta}$/NiO, $BaZr_{0.16}Ce_{0.64}Y_{0.1}Yb_{0.1}O_{3-\delta}$/NiO, and $SrZr_{0.5}Ce_{0.4}Y_{0.1}O_{3-\delta}$/NiO. Key aspects studied include the impact of substrate shrinkage on Ba evaporation, the compensating role of Sr diffusion for Ba loss, and finally the effect on electrolyte densification. The optimized co-sintering process enables the fabrication of dense and gas-tight half-cells with a proton-conducting electrolyte layer as thin as 3 µm, which are subsequently tested in both fuel cell and electrolysis operating modes.

2 Literature Review

2.1 Proton-Conducting Oxides

2.1.1 Materials Development

The foundational development of proton-conducting ceramics as practical electrolyte materials can be traced back to pioneering studies by Hiroyasu Iwahara and his collaborators in the early 1980s [17–19]. In their groundbreaking work published in 1981 [17], Iwahara et al. first demonstrated significant proton conductivity in sintered perovskite-type oxides. These findings opened new pathways toward utilizing ceramics for high-temperature steam electrolysis and other hydrogen-based energy technologies.

Following Iwahara's initial discovery, extensive research was rapidly directed toward exploring perovskite-based proton conductors, primarily focusing on compositions derived from $BaCeO_3$ and $BaZrO_3$ due to their favorable proton conduction characteristics [20–26]. Specifically, trivalent dopants like Y^{3+}, Gd^{3+}, and Yb^{3+} were introduced to create oxygen vacancy within the perovskite lattice [22,27–29], significantly enhancing proton conductivity through the formation of hydroxyl groups under humidified conditions.

Following this conceptual breakthrough, material development efforts focused primarily on two families of perovskite oxides: $BaCeO_3$-based and $BaZrO_3$-based systems [24,30–42]. Among these, $BaCe_{1-x}Y_xO_{3-\delta}$ (BCY) attracted attention due to its high proton conductivity, often exceeding 10^{-2} S cm^{-1} at 600 °C in humidified atmospheres [25,43,44]. However, the major limitation of cerate-based materials lies in their poor thermochemical stability [26,45,46]: $BaCeO_3$ reacts readily with CO_2 and H_2O to form non-conductive phases like $BaCO_3$ and CeO_2, which compromise long-term durability in practical applications.

To overcome this, research gradually turned toward zirconate-based perovskites, such as $BaZr_{1-x}Y_xO_{3-\delta}$ (BZY), which exhibit significantly enhanced chemical stability. Although their proton conductivity is typically lower than BCY at a given temperature, zirconates maintain phase stability even in moist CO_2-containing environments [26,47], making them more suitable for real-world applications. A key challenge, however, is that BZY materials often show high grain boundary resistance, which reduces the effective conductivity in polycrystalline samples [21,48].

The compromise strategy is the partial replacement of Ce with Zr to maintain relatively high ionic conductivity but also achieve high chemical and mechanical stability. BCY and BZY are not isostructural at room temperature [49]. The zirconate is cubic, space group Pm-3m, while for the cerate, Barium cerate undergoes three structural phase transitions up to 1000 °C [50]: crystallization in the

cubic perovskite structure (Pm-3m) occurs only at high temperature (900 °C), the transition from the room temperature orthorhombic phase (Pnma) to another orthorhombic phase (Imma) occurs at ~290°C, to a rhombohedral phase (F-32/n) at 400°C. It was reported that the structure of $BaZr_{1-x}Ce_xO_3$ evolves from cubic Pm-3m to rhombohedral R-3c, then to centered orthorhombic then to primitive orthorhombic with increasing cerium content [51]. This result is not absolute and also depends on the preparation method, the heat treatment temperature and the Y doping content, among other factors.

By increasing the ratio of Zr/Ce the thermal-chemical stability can be improved. Fig. 2.1 is the XRD pattern of the sintered $BaCe_{0.9-x}Zr_xY_{0.1}O_{2.95}$ after being tested in boiling water [52]. The XRD patterns for the pellets of $BaCe_{0.9}Y_{0.1}O_{2.95}$ and $BaCe_{0.7}Zr_{0.2}Y_{0.1}O_{2.95}$ changed significantly after being boiled in water. However, the XRD patterns for the pellets of $BaCe_{0.5}Zr_{0.4}Y_{0.1}O_{2.95}$ and $BaCe_{0.3}Zr_{0.6}Y_{0.1}O_{2.95}$ barely changed after the same stability test. Fig. 2.3 shows the XRD pattern of the calcined $BaCe_{0.8-x}Zr_xY_{0.2}O_{3-\delta}$ powders with different Zr contents after being treated at 900 °C for 3 h in flowing CO_2 [53]. The XRD pattern of the sample with x=0.8 was the same before and after the treatment in CO_2. Only a small amount of $BaCO_3$ was observed for the sample with x=0.5 after CO_2 exposure, while the formation of CeO_2 and $BaCO_3$ was verified for the samples with x=0.0 and 0.3 compositions. These results suggested that zirconium addition into barium cerates can definitely improve the chemical stability of Y doped Ba(Zr, Ce)O_3 (BZCY) compounds based on short-term tests. Therefore, the Zr/Ce ratio is a critical factor for achieving optimal conductivity while ensuring thermo-chemical stability.

Overall, among the various proton-conducting perovskites investigated so far, acceptor doped Ba(Zr, Ce)O_3 has emerged as the most promising electrolyte material due to its unique ability to combine the favorable properties of both $BaCeO_3$ and $BaZrO_3$ [54–63]. It is now widely recognized as a state-of-the-art proton-conducting electrolyte system that meets the critical performance and durability requirements for practical electrochemical energy conversion applications.

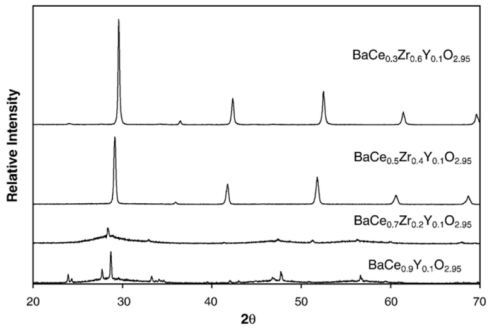

Figure 2.1. XRD patterns for sintered $BaCe_{0.9-x}Zr_xY_{0.1}O_{2.95}$, after being boiled in water for 6 h [52].

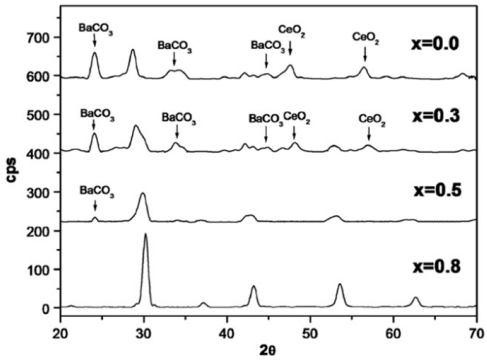

Figure 2.2. XRD patterns of $BaCe_{0.8-x}Zr_xY_{0.2}O_{3-\delta}$ powders after exposure to CO_2 atmosphere at 900 °C for 3 h [53].

2.1.2 Defect Chemistry and Proton Transport

Protons do not occupy regular lattice positions in proton-conducting oxides; instead, they are incorporated into the structure by associating with lattice oxygen ions to form hydroxyl groups, typically represented as $OH_O^{\bullet}$ in Kröger-Vink notation [64]. This incorporation process originates from the dissociative adsorption of hydrogen-containing species, such as hydrogen gas. The process can be expressed as:

$$H_2(g) + 2O_O^{\times} \leftrightarrow 2OH_O^{\bullet} + 2e' \tag{2.1}$$

where the equilibrium constant is expressed as:

$$K = \frac{[OH_O^{\bullet}]^2 n^2}{p_{H_2}[O_O^{\times}]^2} \tag{2.2}$$

When protons are one of the majority point defects, they are more commonly introduced by interaction between oxygen vacancies and water vapor according to:

$$H_2O(g) + V_O^{\bullet\bullet} + O_O^{\times} \leftrightarrow 2OH_O^{\bullet} \tag{2.3}$$

and the equilibrium constant expressed as:

$$K = \exp\frac{\Delta S^0}{R}\exp\frac{-\Delta H^0}{RT} = \frac{[OH_O^{\bullet}]^2}{[v_O^{\bullet\bullet}][O_O^{\times}]p_{H_2O}} \tag{2.4}$$

These expressions are central when addressing proton dissolution, or water uptake in oxides. The reaction is often referred to in the literature as the hydration reaction [65–76].

The Grotthuss mechanism is now the most accepted and likeliest mechanism for proton conduction in oxide at high temperature [77]. In this mechanism the conducting species are H^+ ions that are always located in the electronic cloud of an oxygen of the network, and the conduction can occur only through a jump of the proton itself from the acceptor site toward an adjacent site. The process can be split into two steps. The first one consists in the reorientation of the proton around the oxygen, which makes the

second step easy, the proton jump toward the nearest oxygen neighbor. Both steps of the Grotthuss mechanism are represented in Fig. 2.3.

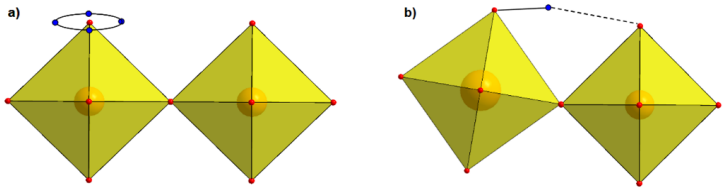

Figure 2.3. Schematic representation of the two steps of proton diffusion according to Grotthuss mechanism: (a) reorientation and (b) proton jump toward the neighbor oxygen atom [77].

It is crucial to increase the number of oxygen vacancies in order to increase the concentration of proton defects. One effective strategy to increase the number of oxygen vacancies is low valent acceptor cation doping (e.g. Y^{3+} doped BZY). The formation of oxygen vacancies can be expressed as:

$$Y_2O_3 = 2Y'_{Zr} + 3O_O^{\times} + V_O^{\bullet\bullet} \qquad (2.5)$$

In the presence of water vapor, these vacancies can be hydrated, and acceptor doping, accordingly, increases the concentration of protons. The literature of high-temperature proton conductors is dominated by systems that are to some extent acceptor doped. The concentration and the mobility of proton defect, which determine the proton conductivity, highly depends on the type of acceptor doping elements.

Yttrium is currently the most popular among various trivalent acceptor elements [78–92]. Compared to many trivalent lanthanide elements, Y substitutes very little at the A-site of the perovskite structure ABO_3 in $Ba(Zr,Ce)O_3$ [27], allowing Y substitution to form the theoretical oxygen vacancy concentration and reach nearly the theoretical saturation hydration concentration in a humid atmosphere. Additionally, the hydration enthalpy and entropy determine the hydration capability of $Ba(Zr,Ce)O_3$ at different temperatures. Kreuer et al.'s [22] research shows that $BaZrO_3$ doped with varying amounts of Y has almost constant hydration enthalpy and entropy, allowing BZY to maintain a certain proton concentration even at relatively high temperatures, which is important in high-temperature electrochemical device applications. In their work they also show that Y introduces the highest proton mobility compared to other dopants such as Gd, Sc and In. Although Sc substitution exhibits similar hydration capability to Y substitution, it has the lowest proton mobility. Because of the excellent hydration capability and high proton mobility demonstrated by Y substitution, almost all reports indicate that Y is one of the best acceptor elements regarding the proton conductivity among the other trivalent elements [28,29]. Han et al. [27] compared 14 dopants in the system $BaZrO_3$, including Sc, Y, In, Pr, Nd, Sm, Eu, Gd, Tb, Dy, Ho, Er, Tm, and Yb, and concluded that only materials substituted with Tm and Ho exhibited conductivities comparable to the one with Y.

In proton-conducting oxides, the phenomenon known as proton trapping refers to the temporary immobilization of protons in the local environment of acceptor dopants, which hinders their long-range mobility [84,93–96]. This effect originates from the strong interaction between the proton and the dopant's neighboring oxygen atoms, whose altered basicity increases the migration barrier. Protons tend to be captured in close proximity to the dopant, forming proton–dopant complexes, while regions distant from dopants remain largely trap-free.

Acceptor doping is generally employed to enhance proton conductivity by generating oxygen vacancies, which serve as hydration sites. However, as a proton hops along a network of lattice oxygen ions, it can be attracted to the localized negative potential near a B-site dopant, falling into a trap. After residing there for a finite time, the proton may be released through thermal activation. This intermittent trapping and release process delay net proton transport and, consequently, reduces the overall conductivity. Because proton conductivity in bulk electrolytes is directly governed by proton mobility via the Grotthuss mechanism, any reduction in mobility caused by trapping leads to a corresponding decrease in conductivity.

While increasing dopant concentration initially raises the number of charge carriers and oxygen vacancies, excessive substitution often introduces more trapping centers, thereby impeding transport. In some cases, high dopant levels also induce structural phase changes that further modify migration pathways. A schematic representation of possible diffusion routes influenced by proton trapping is shown in Figure 2.4.

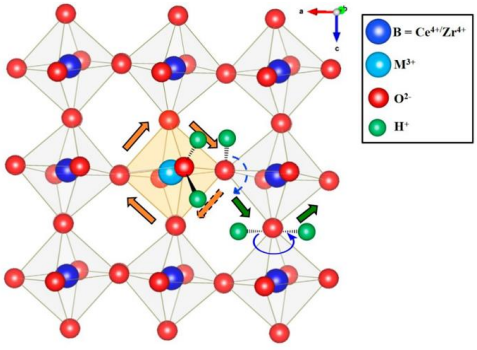

Figure 2.4. Schematic illustration of proton trapping in acceptor-doped proton conductors, highlighting potential pathways for proton migration [84].

There is also another so-called nano-percolation effect in BZY [97]. Proton transport is strongly influenced by the spatial distribution of dopants and the resulting local energy landscape. At low acceptor concentrations, protons tend to be immobilized near dopant sites due to attractive electrostatic interactions and local structural distortions, a situation that restricts their long-range mobility. These

localized regions act as trapping zones, forcing protons to spend significant time in energetically unfavorable “wells” before continuing their migration. As a result, conduction at low doping levels is largely limited by the prevalence of such traps.

When the dopant concentration increases beyond a certain threshold, the trapping regions associated with individual dopants begin to overlap at the nanometer scale. This overlap creates a continuous network of energetically favorable pathways, referred to as nano-percolation channels, through which protons can hop more efficiently. In this regime, the local trapping effect is partially offset by the increased connectivity between dopant-associated sites, enabling protons to traverse the lattice via a series of shorter, energetically accessible jumps. Computational studies, combining density functional theory and kinetic Monte Carlo simulations, have shown that such nano-scale percolating networks markedly reduce the effective migration barrier and enhance macroscopic proton conductivity [98], as show in Figure 2.5.

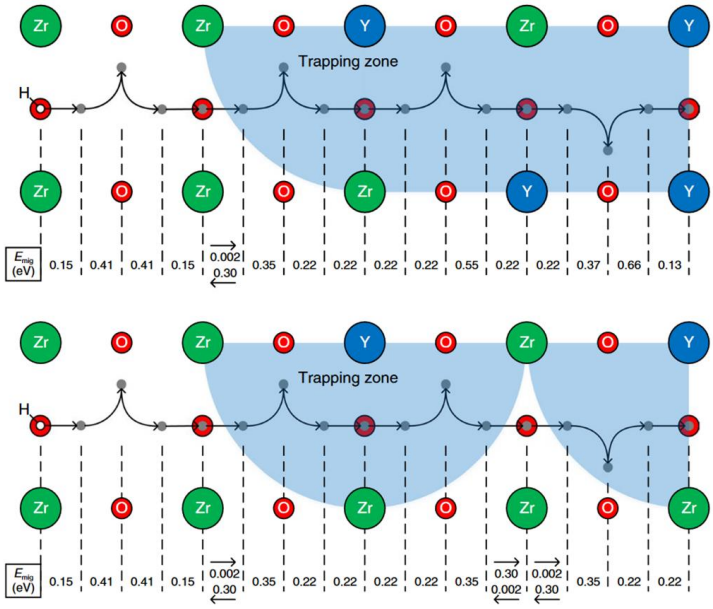

Figure 2.5. Schematic illustration of the nano-percolation effect in proton conduction [98].

The efficiency of this mechanism depends not only on dopant concentration but also on the spatial arrangement of the dopants. A more ordered dopant distribution can yield directional percolation paths, enabling anisotropic transport where certain crystallographic directions exhibit higher conductivity. Conversely, excessive dopant loading or clustering can lead to structural changes that disrupt percolating channels, once again hindering proton motion. Thus, the nano-percolation mechanism represents a

delicate balance between trap formation and network connectivity, offering a compelling explanation for the conductivity maxima often observed in intermediate-doped BZY compositions.

2.1.3 Sintering Challenges of Ba-based Proton Conductors

The densification of Ba-based proton-conducting ceramics, especially those with high zirconium content such as BZY, presents significant challenges due to their intrinsically refractory nature. Compositions rich in Zr tend to exhibit strong resistance to sintering and are often characterized by highly resistive grain boundaries. These characteristics necessitate elevated sintering temperatures and prolonged dwell times to achieve full densification and sufficient grain growth. However, such high-temperature treatments can lead to undesired evaporation of barium from the perovskite lattice. In cases of severe Ba loss, secondary phases such as Y_2O_3 may segregate from the bulk, ultimately degrading proton conductivity and altering the nominal stoichiometry of the material.

To address these sintering limitations, the incorporation of sintering aids has been actively explored as a practical route to reduce the densification temperature while maintaining phase purity and microstructural integrity. Early work by Haile et al. [99] demonstrated that the addition of ZnO could significantly lower the sintering temperature of BZY without compromising its structural or conductive properties, stimulating extensive follow-up investigations into alternative sintering additives. Various transition metal oxides, including NiO, CuO, CoO, and ZnO, have been studied for their potential to promote densification. For instance, $BaZr_{0.85}Y_{0.15}O_{3-\delta}$ sintered at 1450 °C for 8 hours with CuO as a sintering aid achieved a relative density exceeding 95% [100], a level that would otherwise require sintering at 1670 °C for 24 hours in the absence of additives, as shown in Figure 2.6. Similarly, the use of NiO, ZnO, and CuO has been shown to yield $BaCe_{0.3}Zr_{0.55}Y_{0.15}O_{3-\delta}$ ceramics with relative densities above 95% at a substantially lower sintering temperature of 1400 °C [101]. These findings underscore the critical role of carefully selected sintering aids in tailoring the densification behavior of proton-conducting oxides.

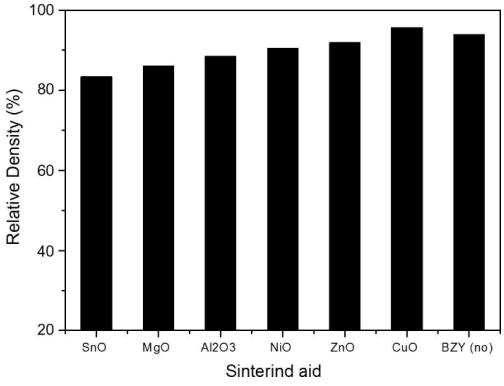

Figure 2.6. Relative densities of the sintered pellets with various sintering aids [100].

Another promising technique to facilitate densification is the solid-state reactive sintering (SSRS) approach, which integrates precursor synthesis and high-temperature sintering into a single thermal step. This method not only accelerates the formation of the desired perovskite phase but also enhances mass transport at the grain boundaries. During SSRS, transient liquid-phase formation between alkali and transition metal oxides can further assist densification through capillary-driven rearrangement and rapid diffusion. In a comprehensive comparison of 16 sintering additives using SSRS, Nikodemski et al. [102] found that the best-performing systems, those incorporating NiO, ZnO, CoO, and CuO, produced ceramics with the highest shrinkage and relative density. Fig. 2.7 shows the optical image of the $BaCe_{0.6}Zr_{0.3}Y_{0.1}O_{3-\delta}$ pellets before and after sintering with different sintering aids. A key observation was that sintering aids with ionic radii similar to Zr^{4+} tended to integrate more effectively into the lattice or grain boundary region, leading to superior densification behavior, as shown in Figure 2.8.

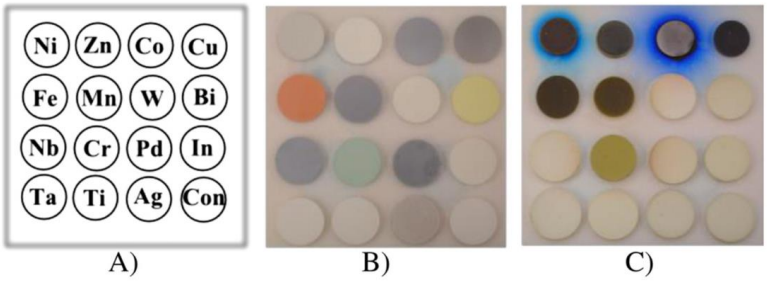

Figure 2.7. Images of BCZY proton conducting ceramic pellets sintered at 1450 °C for 12 h by SSRS. A) Legend showing the metal oxide additive (5 mol.%) added to the BCZY powder mixture. B) Pellets on alumina plate before sintering. C) Same pellets after sintering. Con is the control sample [102].

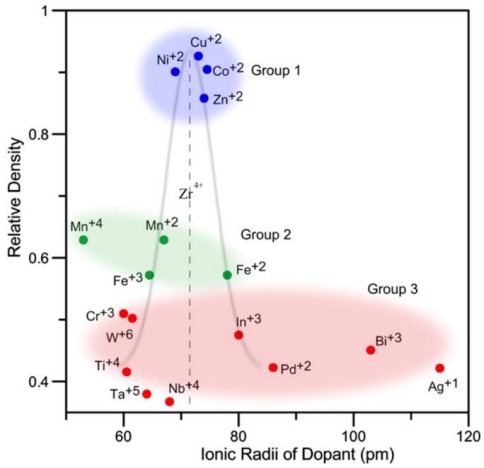

Figure 2.8. Relative density achieved after solid state reactive sintering vs. ionic radius [102].

Liquid phase sintering is another approach to make the Ba-based proton conductor to be densified at lower temperature. The available literature consistently demonstrates that performing the sintering process in the presence of a liquid phase greatly benefits densification and grain growth of ceramics [103–107]. The liquid phase forms a wetting medium around the solid grains, generating capillary forces that pull particles closer and enhance mass transport via dissolution and reprecipitation mechanisms. Consequently, grain coarsening and densification can occur at lower temperatures and in shorter sintering times compared to conventional solid-state sintering.

An example is the work by Jiao et al. [108], who successfully lowered the sintering temperature of $BaZr_{0.85}Y_{0.15}O_{3-\delta}$ to 1400 °C by introducing a $BaO\text{-}B_2O_3$ alkali composite as a sintering additive. This composite possesses a relatively low melting point around 1060 °C, which acts as the main driving force for liquid phase formation during the sintering cycle. Increasing the amount of this sintering aid up to 10 wt% resulted in improved shrinkage rates and relative densities, highlighting the additive's effectiveness in enhancing the sintering kinetics. However, the authors reported that maintaining the sintering aid below 3 wt% was critical in preserving high grain boundary conductivity, as excessive additive content led to secondary phase segregation at grain boundaries, impeding proton conduction.

Similarly, Le et al. [109] investigated the effect of 3 mol% Bi_2O_3 addition to $BaZr_{0.9}Y_{0.1}O_{3-\delta}$, finding that the sintering temperature could be reduced to 1480 °C with enhanced sinterability. Nonetheless, they observed a concomitant decrease in both bulk and grain boundary conductivities, which they attributed to the presence of Bi-rich secondary phases formed during sintering. This phenomenon underlines a critical trade-off inherent in liquid phase sintering: while densification and microstructure can be optimized, the formation and distribution of secondary phases must be carefully controlled to avoid compromising the electrolyte’s proton conduction pathways.

Typically, introducing NiO into the BZCY system during the SSRS process effectively lowers the required sintering temperature. The key to successful SSRS sintering was found to be the formation of a transient liquid phase rich in Ba, Ni, and Y, BaY_2NiO_5 [38,82,110–115], which significantly enhanced cation transport, facilitating densification, grain growth, and homogenization of B-site cation composition. This transient liquid phase forms more readily when NiO is added directly to the oxide precursors (BaO, ZrO_2, CeO_2, and Y_2O_3) than when added to pre-formed BZCY powders, as show in Figure 2.9 suggesting that in-situ formation of the liquid phase during sintering is critical.

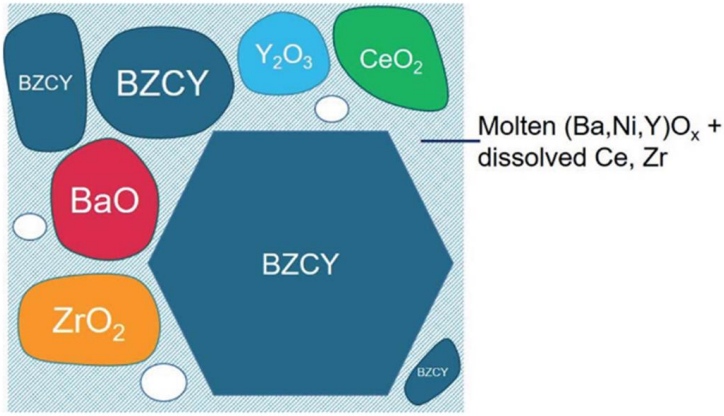

Figure 2.9. Schematics of the Liquid phase sintering mechanism of BZCY during the SSRS process.

However, the use of sintering aids must be approached with caution, as they serve only as secondary components to assist ceramic densification and often do not contribute to, or may even be detrimental to, the physicochemical properties of the ceramics. In proton conductors, the addition of sintering aids can significantly reduce hydration capability, leaving more oxygen vacancies unhydrated at certain temperature. Uda et al. [116] reported that the addition of 2 wt% NiO adversely affected the hydration behavior of the material, significantly reducing proton conductivity. Moreover, the reduced hydration capability results in higher electronic transport numbers under high oxygen partial pressure. In cell operating mode, this manifests as a lower Faradaic efficiency. Therefore, the amount of sintering aid must be carefully considered. Huang et al. [111,117] demonstrated that a lower concentration, such as 0.5 wt%, provided effective sintering assistance without substantially compromising the electrochemical performance. These studies highlight the importance of optimizing the type and amount of sintering aid to balance densification with functional properties.

Sintering aids often exhibit limited solubility in the host lattice and are therefore prone to forming secondary phases. In addition, during the sintering of proton conductors, positively charged grain boundary cores can form, leading to the segregation of low-valence cations such as Ni^{2+} at the grain boundaries. Although Huang et al. [118] reported that the accumulation of Ni^{2+} at grain boundaries does not significantly affect the grain boundary conductivity, the added complexity and unpredictability introduced by such phenomena remain one of the challenges associated with the use of sintering aids.

2.2 Proton Conducting Oxides in the Application of Fuel and Electrolysis Cells

2.2.1 Proton vs. Oxygen-ion Conductors

SOCs represent a core electrochemical technology for efficient energy conversion and storage and are primarily constructed using either oxygen-ion or proton-conducting electrolytes. Despite their similar cell architecture, typically consisting of a dense electrolyte layer sandwiched between porous electrodes, the choice of charge carrier (O^{2-} or H^{+}) leads to fundamentally different reaction mechanisms, transport behaviors, and system-level advantages.

In a conventional oxygen-ion-conducting solid oxide fuel cell (O-SOFC), as shown in Figure 2.10, oxygen molecules from air are reduced at the cathode, forming oxide ions (O^{2-}) that migrate through the electrolyte to the anode, where they oxidize hydrogen fuel to form water vapor. The water generated at the anode side as a product of hydrogen oxidation, which changes the local gas composition and may lead to a reduction in the effective hydrogen utilization. In contrast, in a proton-conducting fuel cell (PCFC), hydrogen is oxidized at the anode to produce protons and electrons. The electrons flow through the external circuit to the cathode, while the protons migrate across the electrolyte and react with oxygen at the cathode to form water vapor. As a result of this reversed water production location, an advantage of PCFCs is that water is formed at the cathode rather than the anode, which prevents local changes in gas composition at the anode side and thereby ensures stable hydrogen utilization.

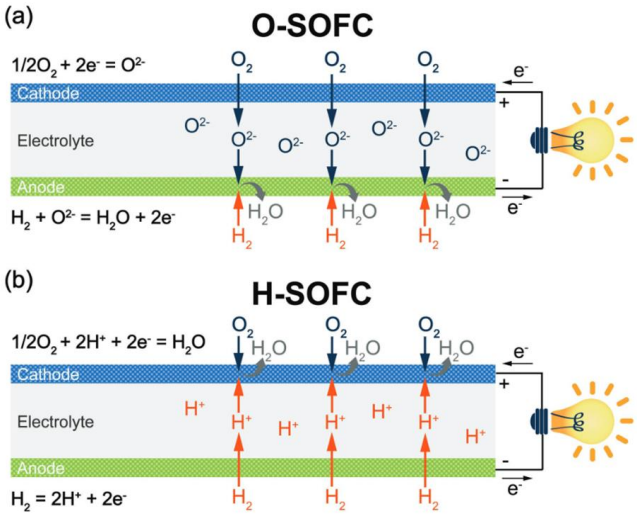

Figure 2.10. Schematic illustration of two different SOFC during their operations: a) Oxygen-ion-conducting electrolyte; b) Proton-conducting electrolyte [119].

A similar distinction exists in electrolysis mode, as shown in figure 2.11. In oxygen-ion-conducting solid oxide electrolysis cells (O-SOECs), steam is introduced at the cathode, where it is split into hydrogen and oxygen ions. The latter migrate to the cathode and release oxygen gas. In proton-conducting electrolysis cells (PCECs), however, steam is introduced at the anode, and the resulting protons are transported to the anode where hydrogen is generated. This configuration results in the production of pure, dry hydrogen at the cathode, presenting a major practical advantage in hydrogen separation and collection.

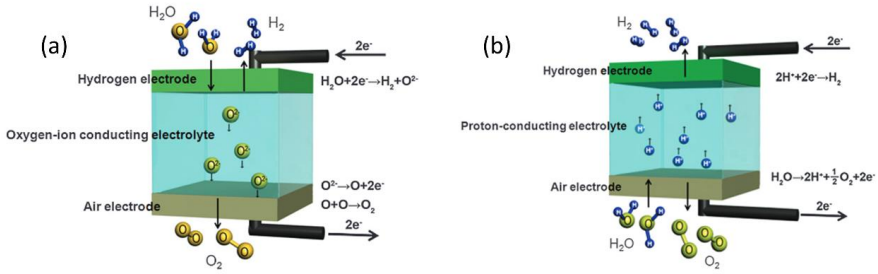

Figure 2.11. Schematic illustration of two different solid-oxide electrolysis cells (SOEC) during their operations: a) Oxygen-ion-conducting electrolyte; b) Proton-conducting electrolyte [120].

Beyond system-level benefits, proton conductors also offer important material-level advantages. As discussed earlier, proton-conducting perovskites often exhibit higher ionic conductivity than oxygen-ion conductors at intermediate temperatures. This allows for lower operational temperatures, which reduces thermal stresses, suppresses interdiffusion between cell components, and improves the chemical and mechanical stability of the device during long-term operation.

However, these advantages are not without trade-offs. A notable limitation of proton-conducting electrolytes is their inability to achieve a 100% Faradaic efficiency. This is because most proton conductors are not purely protonic but also exhibit minor but non-negligible electronic and oxygen-ion conductivity. The presence of these parasitic charge carriers can lead to internal leakage currents, thereby reducing the overall efficiency of the cell.

The hydration process of proton-conducting oxides is described by Equation 2.3, where oxygen vacancies react with water vapor to generate mobile protons in the form of hydroxide defects. The equilibrium constant for this hydration reaction can be expressed as shown in Equation 2.4, which clearly indicates that the equilibrium constant decreases with increasing temperature. This implies that the hydration reaction becomes less favorable at elevated temperatures, shifting the equilibrium to the left. Consequently, within the typical operating temperature range of proton-conducting ceramic cells (400–600 °C), the electrolyte remains only partially hydrated. Under these conditions, residual oxygen

vacancies are present, allowing a parallel transport pathway for oxide ions and contributing to non-negligible oxygen-ion conductivity.

Moreover, under oxidizing atmospheres, these oxygen vacancies can be annihilated via oxidation, as illustrated by the corresponding defect reaction 2.6. This reaction introduces additional holes (positive electronic defects) into the system, thereby giving rise to electronic conductivity. As a result, the overall transport behavior of proton-conducting oxides under realistic working conditions often involves a combination of protonic, oxygen-ionic, and electronic conduction. This intrinsic mixed conductivity complicates the achievement of ideal Faradaic efficiency, particularly under conditions of high temperature and high oxygen partial pressure.

$$\frac{1}{2}O_2 + V_O^{\bullet\bullet} \leftrightarrow 2h^{\bullet} + O_O^{\times} \qquad (2.6)$$

2.2.2 Planar Cell Configuration and Manufacturing Routes

In the development of SOCs, two primary cell configurations have been widely adopted: tubular and planar designs. Tubular SOCs are characterized by a coaxial, cylindrical geometry in which the electrodes and electrolyte are deposited concentrically. This configuration offers excellent sealing reliability and structural integrity but has relatively lower power density and limited scalability. On the other hand, planar SOCs adopt a flat, layered structure where the fuel electrode, electrolyte, and air electrode are stacked in parallel. This arrangement allows for more compact cell assemblies and higher power density. Moreover, the planar configuration is compatible with conventional ceramic processing techniques such as tape casting, screen printing, and physical vapor deposition and so on. Planar SOCs are currently the dominant configuration for high-performance, scalable energy systems.

In response to the growing demand for lower operating temperatures in SOCs, modern cell designs increasingly favor thin electrolyte layers to reduce ohmic resistance and therefore enhance power density. Among various configurations, fuel electrode supported cells have emerged as a practical architecture [121,122], which has been proven effective in systems based on oxygen-ion conductors [123–125]. In this design, the porous fuel electrode serves as a mechanically support, providing structural support for the entire cell and enabling the deposition of a thin, dense electrolyte layer on top. The combination of mechanical strength, manufacturability, and enhanced electrochemical performance makes the fuel electrode supported configuration particularly attractive for scalable planar cell fabrication.

As previously discussed, an SOC consists of a dense electrolyte layer sandwiched between two porous electrodes. In such multilayer architectures, each component requires tailored processing and sintering sequences. For fuel electrode supported planar cells, fabrication generally begins with the support layer,

which provides the primary mechanical strength for the entire structure. This layer is typically several hundred micrometers to 1 mm in thickness and must possess adequate porosity and structural integrity to support subsequent layers [123].

Due to the substantial thickness requirement, the support layer can be fabricated using mechanical pressing techniques, such as cold pressing, warm pressing, hot pressing, or isostatic methods like cold isostatic pressing and hot isostatic pressing, while these techniques are relatively inefficient for large-scale production. Moreover, the typical thickness of around 1 mm implies higher material consumption, which is not desirable from a manufacturing or cost perspective.

Among the various ceramic film-forming methods employed in the fabrication of SOCs [126–140], tape casting has become the most widely adopted technique for producing fuel electrode supports in industrial settings. This technique enables the production of large-area, uniform tapes with controlled thickness and porosity, making it especially suitable for scalable solid oxide cell manufacturing. Tape casting is a wet-forming process in which a slurry, or slip, is cast onto a moving polymeric carrier film. The slurry typically consists of a ceramic powder dispersed in a solvent (either aqueous or organic), along with a mixture of organic additives such as dispersants, binders, and plasticizers. The solvent plays a dual role: it adjusts the viscosity of the slurry to ensure proper flow during casting and facilitates homogeneous dispersion of both the ceramic particles and the organic additives. Dispersants help prevent particle agglomeration, binders maintain the structural integrity of the green tape after casting, and plasticizers enhance tape flexibility prior to sintering.

As show in figure 2.12, the slurry is deposited onto a moving film using a casting head equipped with a doctor blade, which regulates the thickness of the wet layer. As the cast tape travels, the solvent gradually evaporates, leaving behind a flexible green tape. This drying step is critical, as uneven solvent removal can lead to internal stress, cracking or surface skin formation. Therefore, careful control of temperature, humidity, and drying rate is essential to ensure uniform shrinkage and mechanical integrity. Once dried, the green tapes can be cut and used in subsequent fabrication steps.

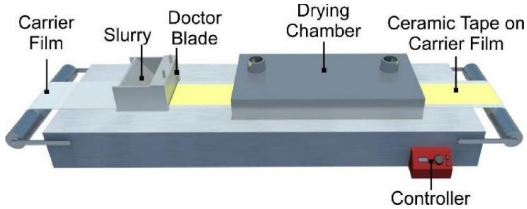

Figure 2.12. Schematic illustration of the tape casting process [124].

Following the fabrication of the fuel electrode support, the remaining layers, such as the functional layer of the fuel electrode, the electrolyte layer, and the air electrode, must be deposited sequentially. In some

cases, the fuel electrode functional layer and electrolyte layer can be co-fabricated with the support via sequential tape casting [141–143], which ensures good interfacial adhesion and structural integration. However, tape casting has limitations in achieving very thin layers: particularly for the electrolyte layer. It is technically challenging to reduce the thickness below 10 µm using this method alone, as achieving very thin layers requires extremely fine powders and carefully optimized slip formulations, which significantly increases the complexity of the process.

Given that the thickness of these layers is typically in the range of a few micrometers to a few tens of micrometers, various coating and deposition techniques are more suitable for their fabrication. Common ceramic coating methods include screen printing [144,145], wet powder spraying [146–148], drop coating [149], dip coating [150], and spin coating [151], as well as vacuum-based techniques such as physical vapor deposition and pulsed laser deposition [152]. These techniques cover a broad range of achievable film thicknesses, as illustrated in Figure 2.13.

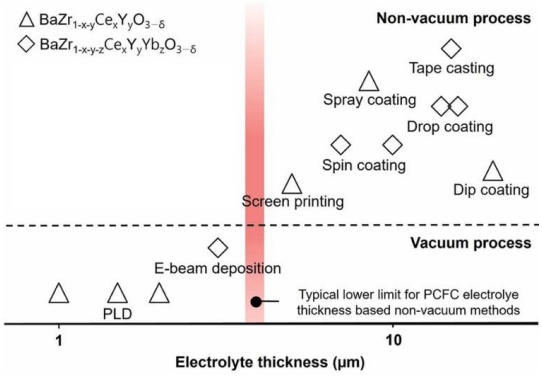

Figure 2.13. Reported thickness ranges of proton conducting electrolytes for PCCs using vacuum and non-vacuum deposition techniques [153].

Among all the coating methods, considering factors such as process scalability and industrial feasibility, screen printing and wet powder spraying are two of the most practical and cost-effective approaches for fabricating relatively thin electrolyte layers. These two methods will be discussed in more detail.

Screen printing has become a mainstream deposition technique in the fabrication of solid oxide cells, particularly for applying ceramic layers such as the electrolyte and electrode functional layers. Its widespread use stems from the balance it offers between process simplicity, material efficiency, and compatibility with large-scale manufacturing. At the core of the screen printing process is the transfer of a ceramic ink, typically a viscous slurry composed of active powder, solvent, dispersants, binders, and plasticizers, through a patterned mesh onto a flat substrate. As shown in Figure 2.14, the ink is

deposited by drawing a squeegee across the screen, which presses the ink through open areas of the mesh in direct contact with the substrate. The resulting wet film is then dried and sintered to obtain the desired ceramic layer.

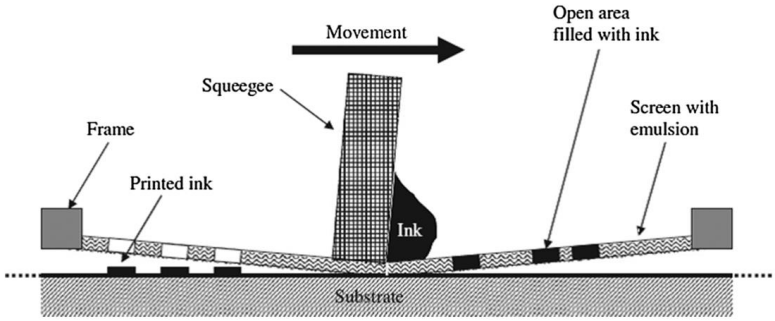

Figure 2.14. Schematic representation of screen printing, showing the deposition of a ceramic paste through a patterned mesh onto a substrate. [154].

A key strength of screen printing lies in its adaptability. By tuning the ink formulation and the mesh parameters, film thicknesses ranging from several microns up to tens of microns can be achieved, making it particularly suitable for intermediate-temperature proton-conducting cells where the electrolyte layer must be thin yet gas-tight.

Despite its advantages, the quality of printed films strongly depends on the careful control of multiple factors during printing. The interaction between the ink's rheology and the substrate surface properties determines whether a uniform, crack-free layer can be formed. In particular, adequate wetting and adhesion are necessary to avoid defects such as delamination or blistering during drying and sintering. Furthermore, the sintered layer's density and microstructure are influenced by the packing of particles during deposition, which in turn depends on the ink's particle size distribution and solid loading.

Screen printing is especially well-suited for planar cell designs with multilayer architectures. It allows for sequential deposition of functional layers directly onto the fuel electrode support, enabling integration with co-sintering processes. For instance, high-performance cells based on BZCY or BZY electrolytes have been successfully fabricated via screen printing, demonstrating good gas tightness and electrochemical performance [155–157].

Wet powder spraying (WPS) is another scalable method for the deposition of ceramic layers. In this method, a suspension, typically composed of ceramic powders dispersed in a liquid medium, is sprayed onto the substrate using a nozzle or airbrush system. The slurry, which has relatively low viscosity compared to screen printing pastes, allows for finer control over the deposited layer morphology. The suspension can be prepared with water or alcohol as the solvent, alongside dispersants and sometimes a

small amount of binder to enhance green strength. Because of the low solids content and high fluidity, the sprayed layer forms by droplet accumulation, resulting in a conformal wet film even on rough or porous substrates.

The microstructure and density of the final sintered layer depend strongly on spraying parameters, including spray distance, suspension properties, droplet size, and substrate temperature. Post-deposition drying and sintering steps are crucial to ensure the removal of residual solvents and organics while achieving proper densification and adhesion.

Recent studies have demonstrated that WPS can effectively fabricate proton conducting electrolyte layers. For instance, Feng et al. [147] conducted a systematic optimization of WPS parameters, such as spray passes, solid loading, and drying conditions, and demonstrated the ability to deposit crack-free BZCYYb films thinner than 10 µm with uniform thickness and high density, suitable for both fuel cell and electrolysis operation modes. Duan et al. [158] successfully applied the WPS method to fabricate proton-conducting cells featuring an electrolyte layer as thin as 3.5 µm, achieving outstanding electrochemical performance that highlights the method's capability for producing high-quality, low-resistance films. In addition, for the fabrication of SOCs, WPS can be used not only for preparing the electrolyte layer but also for various functional layers, such as the fuel electrode, air electrode [131,159], and the coating of metallic interconnects with protective or contact layers [160]. Therefore, the deposition of different SOC components can be highly integrated within a single WPS unit.

2.2.3 Mechanical Challenges of Planar Proton Conducting Cells

As aforementioned, most planar cell configurations still employ the strategy of using fuel electrode supports [121,150,155]. This approach has a significant advantage in that it allows for the fabrication of thinner electrolyte layers, consequently enabling the electrolyte to retain high ionic conductivity at lower temperatures. In this design, the fuel electrode support provides the mechanical strength for the entire cell. A robust support layer is necessary since the cell faces many mechanical strength challenges throughout its fabrication and operational life, including thermal cycling, and long-term service [161–164]. To ensure reliability and durability, the cells must possess sufficient mechanical strength from the outset - capable of withstanding the rigors of stack integration and long-term deployment. During operation, the cells (single or in stack) need to withstand stresses caused by high temperatures, thermal gradients, thermal cycling, and other related factors. Even minor cracks can propagate over time, ultimately leading to the failure of the entire stack and compromising overall system performance. To address these challenges, it is crucial to enhance the mechanical strength of the substrate to increase the maximum tolerable stress threshold. However, this presents a demanding design trade-off for the fuel electrode support layer, which must maintain sufficiently high porosity to ensure effective gas diffusion.

The fuel electrode support typically has the same composition as the fuel electrode, consisting of a certain proportion of electrolyte material and NiO (reduced to Ni during operation). For example, in the case of oxygen ion conductors, the fuel electrode support is composed of yttria-stabilized zirconia (YSZ) and NiO. In the research conducted over the past decades, YSZ/NiO(Ni) compound has proven its reliable mechanical performance as a support layer for solid oxide cells (SOC), even during extended operational periods [165]. However, in the case of PCCs utilizing BZCY/NiO(Ni)-based fuel electrode supports, which remain at a relatively early stage of research and development, mechanical failures are frequently observed during laboratory handling, including sample transfer and test assembly. Despite the substantial increase in research on PCC in recent years, the focus has primarily been on their material development and electrochemical performance [166–168]. In contrast, studies addressing the structural integrity and mechanical properties of BZCY/NiO(Ni)-based fuel electrode supports remain limited and relatively underexplored [14,169]. As shown in Figure 2.15, the results by Huang et al. highlight the inferior mechanical strength of the anode support in PCFCs compared with that of YSZ/NiO [169].

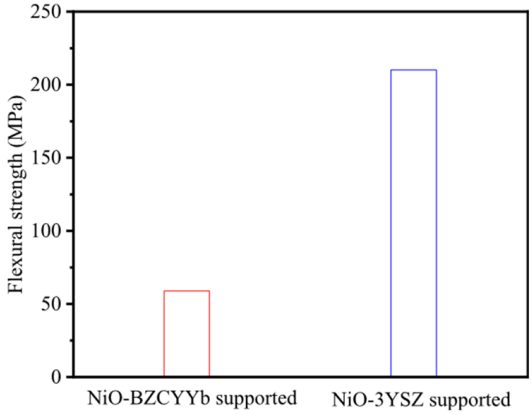

Figure 2.15. Flexural strength of the Ni-BZCYYb and Ni-3YSZ-supported half cells [169].

Bending strength is an important indicator of a material's capability to withstand mechanical loads [170,171]. It represents the maximum stress that a component can endure during a bending test before fracture or failure occurs. It is a highly relevant metric for assessing the mechanical reliability of PCCs. There are several methods for testing bending strength, such as traditional three-point or four-point bending tests [172,173]. However, these techniques all face issues with stress concentration effects, making them less suitable for thin-sheet samples. In contrast, the ring-on-ring test offers significant advantages when testing thin-sheet PCC samples [174,175]. By applying a load through ring-shaped supports, this method provides a more uniform stress distribution, making it particularly well-suited for thin, circular samples. Therefore, measuring the bending strength of the fuel electrode support using the

ring-on-ring method is highly practical and effective for the real-world application of proton conductors, and such data are also essential as a reference for their mechanical strength.

2.2.4 Co-Sintering of Thin Electrolyte with Fuel Electrode

In fuel electrode supported SOCs, the thin electrolyte layer is often co-sintered together with the thick fuel electrode support. This co-sintering approach is advantageous from a fabrication and cost perspective, allowing both structural integrity and electrochemical functionality to be realized in a single sintering step. Unlike the sintering of a standalone electrolyte, co-sintering introduces additional factors that significantly influence the densification behavior of the electrolyte.

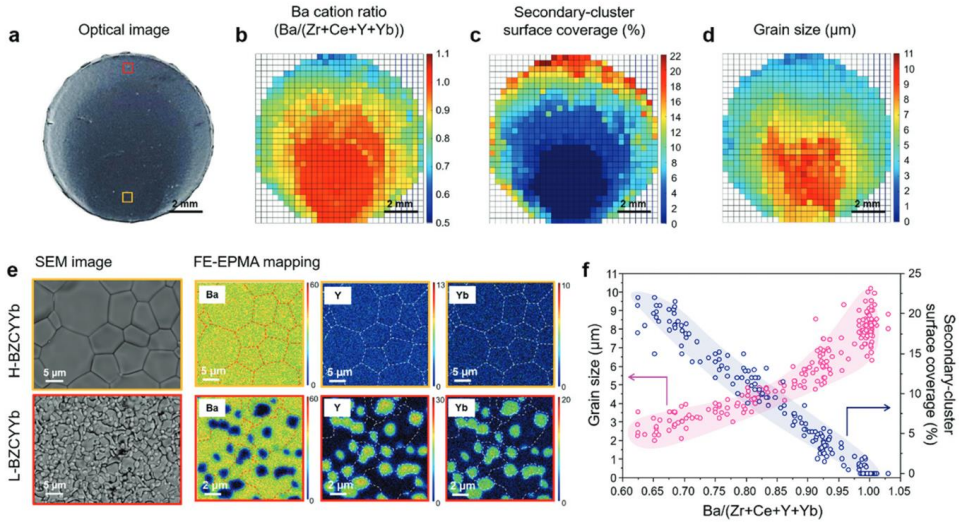

Figure 2.16. Managing the barium chemical potential at the surface of the electrolyte during sintering and its impact on the electrolyte's chemical composition and sintering behavior [177].

One of the primary concerns in the sintering of Ba-based PCCs is Ba evaporation, as discussed in previous sections. Ba evaporates at elevated temperatures (>1400 °C), leading to a deviation from the intended stoichiometry and formation of secondary phases that could hinder the electrolyte densification [176,177]. In the co-sintering process, Ba loss remains a critical issue, and is arguably even more severe, since Ba evaporation initiates at surfaces exposed to air. Given that the electrolyte in co-sintered half-cells is typically only a few micrometers thick, it becomes fully susceptible to Ba loss. Choi et al. [177] addressed this by controlling the local chemical potential of Ba at the electrolyte surface during sintering. By placing an auxiliary Ba-containing pellet above the electrolyte as a Ba vapor source, they established a lateral gradient in Ba chemical potential that counteracted evaporation. This method preserved stoichiometric composition across the electrolyte, facilitated grain growth to an average size of ~10 μm,

and eliminated the need for foreign sintering aids that could otherwise cause electronic leakage. However, in regions without Ba compensation, a substantial amount of Y- and Yb-containing secondary phases is present, and grain growth is severely inhibited, as shown in Figure 2.16.

Nevertheless, Ba evaporation issue is further complicated by interactions between the electrolyte and the underlying fuel electrode. The shrinkage mismatch between the two layers plays a crucial role. The fuel electrode typically contains a high-volume fraction of NiO, which exhibits rapid shrinkage during the initial stages of sintering. This early shrinkage may initially promote densification of the adjacent electrolyte layer through compressive stress. For example, An et al. [155] highlighted the beneficial role of the substrate's shrinkage in improving the densification of BZCY thin films, as show in Figure 2.17. They showed that when a structurally and compositionally uniform NiO–BZCY anode support was co-sintered with the electrolyte, densification occurred at a much lower temperature (1350 °C) compared to sintering the electrolyte alone (>1600 °C). This improvement was attributed to two synergistic mechanisms: (i) the mechanical assistance from anode shrinkage and (ii) the in-situ formation of a transient Ba–Y–Ni–O phase (BaY_2NiO_5, BYN) at the anode–electrolyte interface, which acted as an internal sintering aid by enhancing cation diffusion. Unlike externally added sintering aids, this internally supplied phase left no detrimental residuals or compositional inhomogeneity after sintering. By carefully matching the shrinkage behaviors of the electrode and electrolyte—achieved through controlling particle size, granule packing structure, and green density, they produced thin (< 5 μm), defect-free electrolyte layers with minimal grain boundaries in the through-thickness direction, thereby lowering grain boundary resistance and enabling ohmic resistance being as low as 0.09 Ω·cm² at 600 °C.

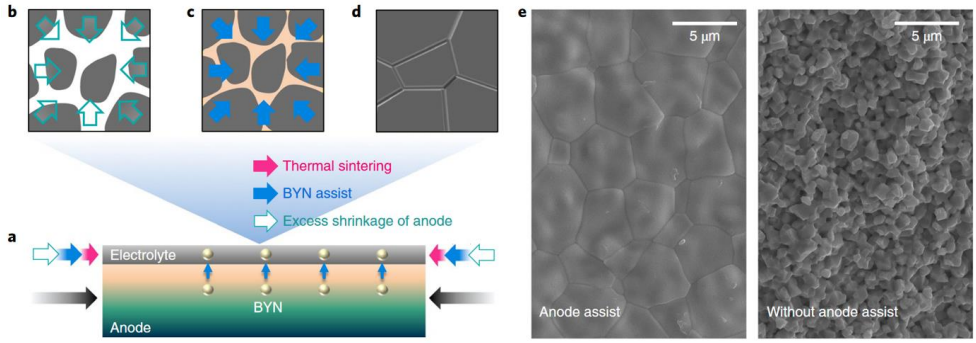

Figure 2.17. Anode-assisted densification of electrolyte.

Chemical interactions at the interface between the fuel electrode and the electrolyte also play a key role in the sintering process. For instance, NiO present in the fuel electrode can diffuse into the electrolyte layer during sintering, especially at elevated temperatures or when the electrolyte is particularly thin. While limited Ni incorporation may facilitate sintering by enhancing mass transport and promoting

densification, excessive diffusion can result in undesirable effects, including electronic conductivity and a reduction in proton conductivity [111,117,178].

Furthermore, if the electrolyte composition embedded in the fuel electrode differs from that of the main electrolyte layer, interdiffusion of cations across the interface may occur during sintering. This can potentially lead to a different chemical gradient, and therefore have influence on the phase formation and layer densification process. For example, in the work by Leonard et al., a comparison was made between different substrates, specifically $SrZr_{0.5}Ce_{0.4}Y_{0.1}O_{3-\delta}$ (SZCY) and $Ba(Zr_{0.5}Ce_{0.4})_{8/9}Y_{0.2}O_{2.9}$, to investigate their effects on electrolyte sintering. The use of a Sr-based substrate was found to reduce the sintering temperature, and the grain growth behavior differed significantly between the substrates as shown in Figure 2.18. This highlights the crucial influence of the interaction between the substrate and electrolyte during co-sintering on the sintering process.

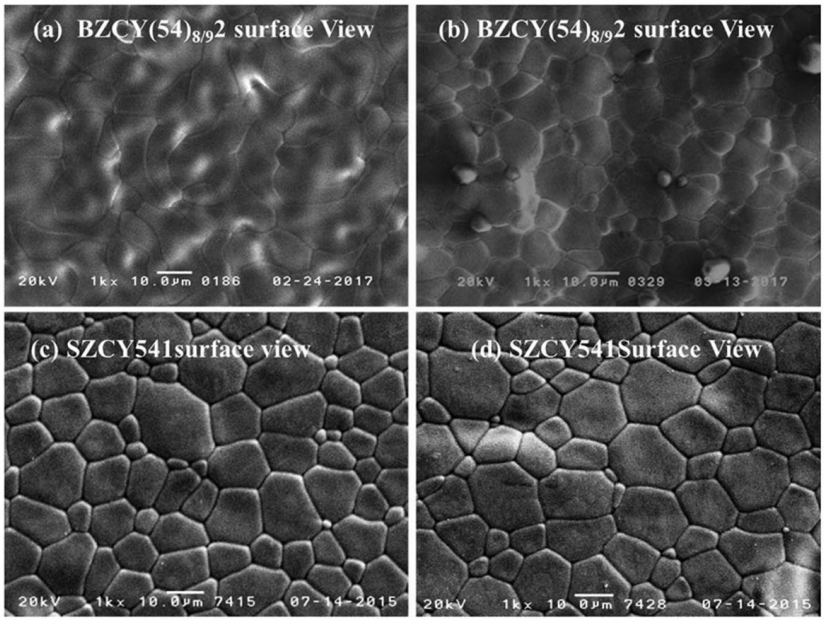

Figure 2.18. Surface morphologies of half-cells under different sintering conditions: (a) $Ba(Zr_{0.5}Ce_{0.4})_{8/9}Y_{0.2}O_{2.9}$ sintered at 1450 °C for 5 hours on a NiO–SZCY cathode. (b) $Ba(Zr_{0.5}Ce_{0.4})_{8/9}Y_{0.2}O_{2.9}$ sintered at 1550 °C for 5 hours on a Ni–$Ba(Zr_{0.5}Ce_{0.4})_{8/9}Y_{0.2}O_{2.9}$ cathode. (c) SZCY sintered at 1400 °C on a NiO–SZCY cathode and (d) SZCY sintered at 1450 °C for 5 hours on a NiO–SZCY cathode.

Liu et at., [122] demonstrated that by pairing a $BaCe_{0.4}Zr_{0.4}Y_{0.1}Yb_{0.1}O_{3-\delta}$ electrolyte with a Ba-rich $BaCe_{0.7}Zr_{0.1}Y_{0.1}Yb_{0.1}O_{3-\delta}$ + NiO negative electrode, fabricated via solid-state sintering (SSS) with a fast pre-crystallization step, it was possible to create a chemically homogeneous, single-grain–thick electrolyte (~5 µm) with grain sizes more than twice those obtained from conventional solid-state reactive sintering (SSRS), as shown in Figure 2.19. This pairing minimized Ba deficiency (49.4 at.% vs.

~46.9 at.% in SSRS), suppressed Y and Yb segregation at grain boundaries, and reduced the ohmic resistance to 0.08 Ω·cm² at 450 °C. Importantly, the SSS-processed electrode acted as a Ba reservoir during co-sintering, continuously supplying Ba to the electrolyte to compensate evaporation losses.

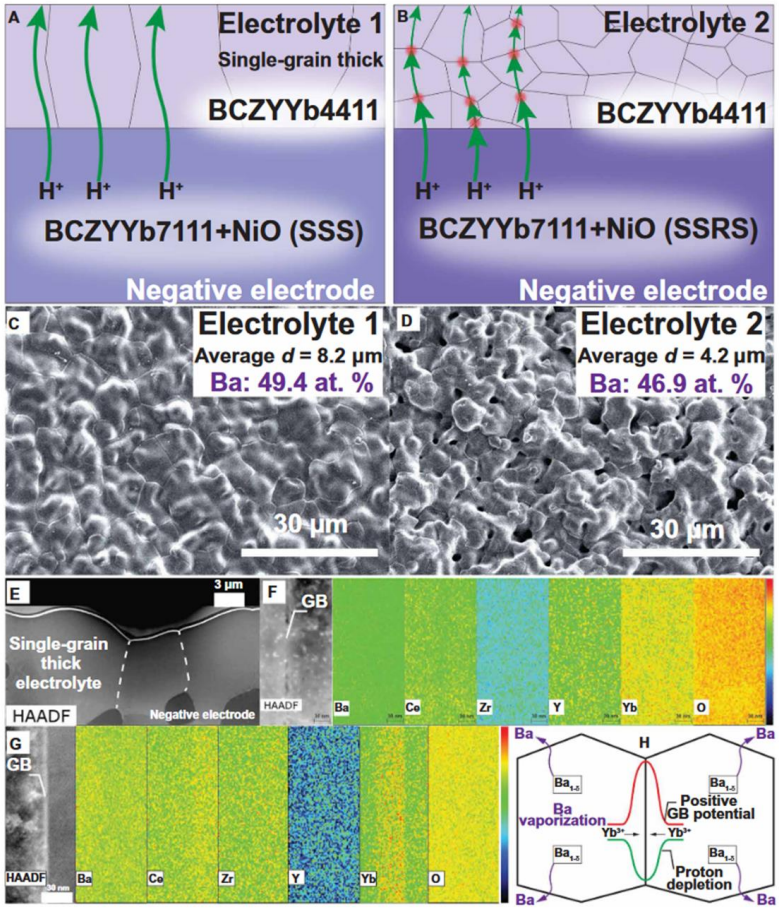

Figure 2.19. By pairing the $BaCe_{0.4}Zr_{0.4}Y_{0.1}Yb_{0.1}O_{3-\delta}$ electrolyte with a $BaCe_{0.7}Zr_{0.1}Y_{0.1}Yb_{0.1}O_{3-\delta}$ + NiO (SSS) negative electrode, a thin, chemically uniform, single-grain–thick electrolyte with high proton conductivity is achieved due to minimal grain boundary resistance. In contrast, using a $BaCe_{0.7}Zr_{0.1}Y_{0.1}Yb_{0.1}O_{3-\delta}$ + NiO (SSRS) electrode produces multi-grain–thick electrolyte exhibiting Ba deficiency and Yb segregation at grain boundaries.

The implications of these findings are that the electrode composition and pre-sintering history can be deliberately engineered to serve not only as a mechanical support but also as a chemical buffer that preserves electrolyte stoichiometry during high-temperature co-sintering. Specifically, tailoring the chemical makeup of the fuel electrode to control the availability of volatile species such as BaO can mitigate Ba loss from the electrolyte, thus preventing the formation of secondary phases and maintaining

high proton conductivity. Second, achieving a close match between the shrinkage rate and the onset of densification for the electrode and electrolyte layers is essential to avoid mechanical defects such as warping, delamination, or crack formation, issues that become more pronounced as cell dimensions increase in large-area manufacturing. Moreover, the selected processing route, whether via conventional sintering, liquid-phase–assisted densification, or solid-state reactive sintering (SSRS), exerts a direct influence on both mechanical compatibility and interfacial chemistry by modifying grain growth dynamics, phase evolution, and cation interdiffusion. Therefore, successful co-sintering of thin electrolyte layers with NiO-based fuel electrodes demands precise control over multiple processing parameters, including the shrinkage profile, interfacial reaction kinetics, atmosphere composition, and thermal gradients throughout the sintering cycle. When these strategies are combined, they enable the fabrication of thin, dense, and compositionally stable electrolytes with minimal grain boundaries and optimized microstructures, resulting in superior proton transport properties [179–192]. Such process optimization not only enhances the durability and electrochemical performance of anode-supported protonic ceramic fuel cells (PCFCs) but also offers a scalable manufacturing pathway toward commercially viable, high-efficiency energy conversion devices.

3 Materials and Methods

3.1 Sample preparation

3.1.1 Powders

Various powders with different compositions are used. Some are synthesized in-house, while others are commercial powders. First, an overall introduction to the powder synthesis methods will be given, followed by a list that details chapter by chapter, the composition, abbreviations, synthesis routes, or sources of the powders used in each section.

In this thesis, solid-state reaction (SSR) synthesis was used to prepare the powders $BaZr_{0.8-x}Ce_{0.2}Y_xO_3$ (x=0.1-0.3) and $BaZr_{0.16}Ce_{0.64}Y_{0.1}Yb_{0.1}O_3$. The raw powders $BaCO_3$, ZrO_2, CeO_2, and Y_2O_3, Yb_2O_3 (Sigma Aldrich, purity grade of 99%) were weighed according to the aimed stoichiometry and mixed in ethanol in a tumbler mixer for 24 h, followed by drying in a drying cabinet at 80 °C for 24 h. The mass ratio of powder, milling balls and ethanol is 1:2:3. The powders were collected and calcined at 1300 °C for 10 h. After calcination, the milling and drying processes were repeated. Finally, the powders were sieved using 100 μm mesh sieve to get the final powder.

$BaZr_{0.16}Ce_{0.64}Y_{0.1}Yb_{0.1}O_3$ was also prepared by Sol-gel method. The Ba, Zr, Ce, Y, Yb nitrate precursors were first dissolved in deionized water and stirred. After 10 min, citric acid was added, and the solution was heated to 80 °C and stirred again for 1 h. Ethylene glycol was then introduced, and the pH was adjusted to 7 by adding NH_4OH. The molar ratio of ethylene glycol : citric acid : total metal ions was maintained at 3 : 3 : 2. The mixture was stirred until it dried into a gel, which was subsequently calcined at 1000 °C for 5 h.

All powders used in each chapter, whether synthesized in-house or commercially obtained, are listed in Table 3.1.

Table. 3.1 Composition, abbreviation, and source of powders used in each chapter. Some compositions are not abbreviated due to their infrequent mention in the text. In Chapter 7, two types of BZCYYb powders are used: one synthesized via SSR for the substrate and fuel electrode, and the other a commercial powder for the electrolyte layer. SSR: solid-state reaction; SG: sol–gel.

	Composition	Abbreviation	Preparation method/source
Chapter 4	$BaZr_{0.7}Ce_{0.2}Y_{0.1}O_{3-\delta}$	BZCY-Y10	SSR
	$BaZr_{0.65}Ce_{0.2}Y_{0.15}O_{3-\delta}$	BZCY-Y15	SSR
	$BaZr_{0.6}Ce_{0.2}Y_{0.2}O_{3-\delta}$	BZCY-Y20	SSR
	$BaZr_{0.55}Ce_{0.2}Y_{0.25}O_{3-\delta}$	BZCY-Y25	SSR

	$BaZr_{0.5}Ce_{0.2}Y_{0.3}O_{3-\delta}$	BZCY-Y30	SSR
Chapter 5	$BaZr_{0.65}Ce_{0.2}Y_{0.15}O_{3-\delta}$	BZCY-Y15	SSR
	NiO	/	Commercial (Vogler)
Chapter 6	$BaZr_{0.16}Ce_{0.64}Y_{0.1}Yb_{0.1}O_3$	/	SG
	$BaZr_{0.7}Ce_{0.2}Y_{0.1}O_{3-\delta}$	/	Commercial (Marion Technologies, France)
	$BaZr_{0.16}Ce_{0.64}Y_{0.1}Yb_{0.1}O_3$	/	Commercial (Kusaka Rare Metal Products Co. Ltd Japan.)
Chapter 7	$BaZr_{0.65}Ce_{0.2}Y_{0.15}O_{3-\delta}$	BZCY-Y15	SSR
	$BaZr_{0.16}Ce_{0.64}Y_{0.1}Yb_{0.1}O_3$	BZCYYb	SSR
	$BaZr_{0.16}Ce_{0.64}Y_{0.1}Yb_{0.1}O_3$	BZCYYb	Commercial (Kusaka Rare Metal Products Co. Ltd Japan.)
	NiO	/	Commercial (Vogler)
	$SrZr_{0.5}Ce_{0.4}Y_{0.1}O_{3-\delta}$	SZCY	Commercial (Kusaka Rare Metal Products Co. Ltd Japan.)
	$Ba_{0.5}La_{0.5}CoO_{3-\delta}$	BLC	Commercial (Kusaka Rare Metal Products Co. Ltd Japan.)

3.1.2 Pellet Pressing and Sintering

In Chapter 4 and 7, pellet samples were fabricated for further investigation. In a typical pellet preparation process, the powders were filled in a 13 mm die and uniaxially pressed with 4 kN, and then pressed by cold isostatic pressing with 3000 MPa for 2 min.

In Chapter 4, the pellets were embedded in sacrificial powder, placed in an Al_2O_3 crucible, and then sintered in air at 1500 °C for 10h with 5 K/min heating rate and natural cooling rate.

In Chapter 7, the purpose was to investigate the surface Ba evaporation, therefore no sacrificial powder was used to cover the surface of the pellet during sintering. The sample was sintered at 1450 °C for 5h with 2 K/min heating rate and cooling rate.

3.1.3 Substrate Prepared by Tape Casting

In this thesis, the fuel electrode support layer and the functional layer were fabricated by tape casting. Chemicals used in the paste are listed in Table 3.2. The formulations of the tape casting slips are given in Table 3.3. In Chapter 5, the BZCY-Y15/NiO fuel electrode support layer paste was prepared according to the recipe without a pore former. In Chapter 7, the BZCYYb/NiO fuel electrode support

layer paste was prepared following the recipe with a pore former, whereas the functional layer paste was prepared according to the recipe without a pore former.

Table 3.2. Chemical description used for tape casting paste

Product name	Description	Manufacturer
Ethanol	-	AHK Alkohol Handelskontor GmbH
MEK	Methyl ethyl ketone	KMF Laborchemie GmbH
Nuosperse FX9086	Methoxy methyl ethyl acetate	Elementis Specialties Inc.
PVB 98	Polyvinyl butyral (98 type)	Merck KGaA
OXSOFT-3G8	2-ethylhexanoate	OXEA GmbH
PEG400	Polyethylene glycol, $M_n \approx 400$	Merck KGaA
Pore former	Starch	Sigma-Aldrich

Table 3.3 Paste formulations for tape casting

	Without pore former (mass ratio %)	With pore former (mass ratio %)
Powder (Elctrolyte powder : NiO=4:6)	68.78	63.83
Solvent (Ethanol : MEK=1:2)	19.84	22.43
Pore former	0	3.2
Nuosperse FX9086	1.05	0.95
PVB 98	4.13	3.83
OXSOFT-3G8	3.11	2.88
PEG400	3.11	2.88

The slurry preparation procedure was as follows: The solvent and dispersant (Nuosperse FX9086) were first weighed and placed in a mixing container, followed by the addition of ceramic powder and pore former (if applicable). Milling balls were then added, and the mixture was pre-mixed in a Thinky mixer at 1000 rpm for 1 min. Subsequently, the plasticizers (OXSOFT and PEG400) were added sequentially, followed by the binder (PVB98). The slurry was further mixed in the Thinky mixer at 1500 rpm for 3 min. The well-homogenized slurry was stored for 24 h prior to tape casting.

For the fabrication of the fuel electrode functional layer, the doctor blade gap was set to 70 μm, whereas for the support layer, the gap was set to 1200 μm. In Chapter 5, BZCY-Y15/NiO was used for mechanical property studies, and only the support layer was prepared (single tape casting). In contrast, in Chapter 7, BZCYYb/NiO fuel electrodes included both functional and support layers, which were fabricated by sequential tape casting: the functional layer slurry was cast first, dried for 6 h, and then the support layer slurry was cast on top.

After complete drying, the green tapes were punched into the desired dimensions. Before any subsequent processing, the tapes underwent debinding by heating at 0.5 $K \cdot min^{-1}$ to 900 °C, holding for 1 h, and then cooling at 2 $K \cdot min^{-1}$ to room temperature.

The samples for the mechanical tests in Chapter 5 were punched into round discs with a diameter of 18 mm. After debinding, they were sintered at 1400 °C, 1450 °C, and 1500 °C for 3 h on sacrificial powder in an Al_2O_3 crucible, and are hereafter referred to as 1400, 1450, and 1500, respectively. The samples sintered at 1450 °C were further subjected to a reduction treatment in an Ar + 3 vol% H_2 atmosphere and are denoted as 1450_re.

3.1.4 Deposition of Electrolyte Layer by Wet Powder Spraying

The electrolyte layer was deposited onto the pre-sintered fuel electrode via the wet powder spraying (WPS) method. The preparation of the suspension for WPS was straightforward: a given mass fraction of electrolyte powder was simply dispersed in ethanol, without the addition of any extra dispersants or binders. After adding the powder to the ethanol, the mixture was ultrasonicated in a water bath for 30 minutes, after which it was immediately used for the WPS process. Any unused suspension would sediment over time; before reuse, it was re-dispersed by repeating the 30-minute ultrasonication. Chapter 6 will focus on the influence of various WPS parameters on the properties of the deposited and dried electrolyte layer. Therefore, the specific WPS parameters are not presented here.

3.2 Characterization

3.2.1 X-ray Diffraction

X-ray diffraction (XRD) is based on the interaction between incident X-rays and the periodic atomic arrangement within a crystalline material. When a monochromatic X-ray beam impinges on a crystal, the electrons surrounding each atom scatter the incident radiation in all directions. The regular, periodic arrangement of atoms means that in certain specific directions, the scattered waves interfere constructively, producing measurable diffracted beams. This condition for constructive interference is described by Bragg's law,

$$n\lambda = 2d\sin\theta \quad (3.1)$$

where n is an integer representing the diffraction order, $\boldsymbol{\lambda}$ is the X-ray wavelength, d is the spacing between parallel lattice planes, and $\boldsymbol{\theta}$ is the angle of incidence (and reflection) with respect to these planes.

In practical measurements, the diffraction intensity is recorded as a function of $2\boldsymbol{\theta}$, producing a pattern of peaks whose positions are determined by the crystal lattice geometry and whose intensities are influenced by the atomic arrangement (structure factors) within the unit cell. Each crystalline material generates a unique set of diffraction peaks, allowing for phase identification through comparison with reference databases. Furthermore, the breadth and shape of the diffraction peaks carry additional microstructural information: peak broadening can be associated with finite crystallite size or lattice strain, while systematic variations in relative intensities can indicate preferred orientation.

Beyond phase analysis, XRD can be used to refine lattice parameters, quantify phase fractions, and evaluate structural defects. With advanced analysis methods, such as Rietveld refinement, detailed crystallographic models can be derived from the diffraction data, enabling a deeper understanding of the material's structure–property relationships. Rietveld refinement is a full-pattern fitting method used to extract detailed crystallographic information from powder diffraction data. Unlike traditional approaches that rely solely on the positions of a few diffraction peaks, this method models the entire diffraction profile by calculating the expected intensity at each step of the scan, based on an initial structural model and instrumental parameters. The calculated pattern is iteratively adjusted to minimize the weighted difference between the observed and calculated intensities, typically using the least-squares method. In this process, both structural parameters, such as lattice constants, atomic coordinates, site occupancies, and thermal displacement factors, and non-structural parameters, such as background shape, peak profile functions, preferred orientation, and instrumental broadening, can be refined simultaneously. By making use of all available diffraction data rather than selected peaks, Rietveld refinement increases the accuracy and reliability of the derived results, especially for complex or multiphase materials.

In this thesis, the phase composition for all the samples were examined by Bruker D4 Endeavour (Cu-Kα-radiation). The pellet samples in Chapter 4 were ground into powder for the XRD characterization. The 2θ range for the XRD patterns used for Rietveld refinement was 10 - 120°.

3.2.2 Electronic Microscopy and Elemental Analysis

Electron microscopy encompasses a range of imaging techniques that utilize a focused beam of high-energy electrons to examine the structure and composition of materials at much higher resolutions than possible with light microscopy. Because the de Broglie wavelength of accelerated electrons is several orders of magnitude shorter than that of visible light, electron microscopes can resolve features down to the atomic scale. By controlling how the electron beam interacts with the specimen — whether scanning the surface or transmitting through an ultrathin section — different types of information can be obtained, including surface morphology, internal microstructure, crystallography, and chemical composition.

Among the most widely used electron microscopy techniques in materials research are scanning electron microscopy (SEM) and transmission electron microscopy (TEM), often complemented by energy-dispersive X-ray spectroscopy (EDS) for compositional analysis.

SEM employs a finely focused electron beam that is raster-scanned across the specimen surface. The interaction between incident electrons and the sample generates a variety of signals, including secondary electrons, backscattered electrons, and characteristic X-rays. Secondary electron imaging is particularly sensitive to surface topography, producing high-resolution, three-dimensional-like images, whereas backscattered electrons (BSE) provide contrast related to the atomic number of the specimen's constituents. Owing to its large depth of field and wide range of magnifications, SEM is a powerful tool for examining surface morphology and microstructural features.

TEM relies on the transmission of a high-energy electron beam through an ultrathin specimen, typically less than 100 nm in thickness. The transmitted electrons are scattered by the internal atomic structure, forming images or diffraction patterns that reveal details at the nanometer or even sub-angstrom scale. TEM enables direct observation of lattice fringes, defects, and interfaces, and selected-area electron diffraction can provide crystallographic information from localized regions.

In scanning transmission electron microscopy (STEM), a highly focused electron probe, often less than 1 Å in diameter, is raster-scanned across the thin specimen. At each probe position, various detectors collect signals such as bright-field, dark-field, or high-angle annular dark-field (HAADF) images, the latter offering Z-contrast that is sensitive to the atomic number of the elements present. STEM combines the imaging principles of TEM with the analytical flexibility of scanning methods, enabling atomic-resolution mapping of both structure and composition.

Both SEM and TEM can be equipped with energy-dispersive X-ray spectroscopy (EDS) systems. EDS detects the characteristic X-rays emitted when the incident electrons displace inner-shell electrons from atoms in the sample. By measuring the energy of these X-rays, the elemental composition of the probed region can be determined. In SEM, EDS is typically used for rapid surface compositional mapping, while in TEM it allows chemical analysis with nanometer-scale spatial resolution. The combination of imaging and compositional analysis makes electron microscopy coupled with EDS a versatile approach for correlating microstructure with chemistry.

In Chapter 4, the surface microstructure and element distribution of polished samples were observed using an SEM (ZEISS ULTRA 55, Carl Zeiss NTS GmbH, Germany) equipped with EDS (Oxford Instruments, UK). The analysis of grain size is achieved through the linear intercept method. Multiple intercept lines are drawn on SEM images, and the number of grains intersected by each line is counted

to determine the average grain size along that line. Finally, the grain sizes along each intercept line are statistically summarized to obtain the overall average grain size. Samples for scanning transmission electron microscopy (STEM) were prepared using a conventional dimpling route to achieve a large area of electron transparent materials, facilitating the search for suitable grain boundaries for high resolution analysis. Bulk samples were first metallographically ground and polished to a thickness of 100 µm and afterwards dimple ground to a minimal thickness of 10 to 15 µm using a dimple grinder (Gatan Inc., USA). Afterwards the final hole was milled and thinned using an Ar ion milling device (PIPS II, Gatan Inc., USA) with a final Ar energy of 500 eV. STEM imaging and spectroscopy was done using a probe Cs-corrected Hitachi HF5000 microscope (Hitachi High-Technologies, Japan) at 200 keV equipped with an Oxford Instruments Ultrim TLE EDS detector. EDS data analysis and curation were performed with Aztec (Oxford Instruments, UK).

In Chapter 5, the microstructure of both polished specimens and fracture surfaces was observed using an SEM (TM3000, Hitachi, Japan). Porosity analysis was conducted using ImageJ/Fiji software, which identifies pores based on distinct grayscale contrast between pores and solid phases (particles), and calculates the area fraction of pore regions.

In Chapter 6, the coating quality of the electrolyte layer was characterized by SEM (EM-30 N, Coxem, Ltd. Korea). In Chapter 7, both ZEISS ULTRA 55 and EM-30 N were used to characterize the samples. Samples in Chapter 7.2 for STEM were prepared using focused ion beam (FIB) to select a specific area (containing grain boundaries), and it was also characterized by Hitachi HF5000 equipped with an Oxford Instruments Ultrim TLE EDS detector.

3.2.3 Thermogravimetric and Sintering Shrinkage Analysis

The temperature dependence of proton concentration of the materials was evaluated by thermogravimetric analysis (TGA, Netzsch STA449F3 Jupiter). The sintered pellets were ground into powder and sieved to obtain particles with a size ranging from 200 to 300 µm. The powder is initially heated to 1200 °C in dry N_2 for 1 hour to achieve complete dehydration. Subsequently, the atmosphere is switched to water-saturated nitrogen-argon mixture (1.9 vol.% H_2O-10% vol. N_2-Ar) with a flow rate of 10 mL/min of dry protective gas through a balance and 50 mL/min of gas saturated with water in a bubbler at 17 °C. During the cooling process, the powder is stabilized for two hours at each 100 °C increment. The mass changes of the powder between 1200 °C and 100 °C are continuously recorded. Finally, the buoyancy effect was corrected using data from a blank test. Then the proton concentration can be calculated according to the following equation [193]:

$$[OH_O^{\bullet}] = \frac{2 \times \Delta m / M_{H_2O}}{m_0 / M_{BZCY}} \quad (3.2)$$

Where Δm is the mass increment relative to complete dehydrated powder at each temperature stage. m_0 is the mass of the complete dehydrated powder.

The sintering shrinkage curve of the green tape was measured using a Netzsch TMA 402 F1 Hyperion in air atmosphere, with sintering conditions identical to those used in the actual sintering process. The specific set up will be further explained in Chapter 7.

3.2.4 Electrical Impedance Spectroscopy (EIS) and I-V Measurements

EIS is an essential analytical technique used to investigate the charge transport properties and interfacial phenomena in ceramic materials, particularly in the context of ionically conductive oxides such as proton- or oxygen-ion-conducting perovskites. This technique involves applying a small-amplitude sinusoidal AC voltage (typically 5–20 mV) across the sample over a wide frequency range (from MHz down to mHz) and recording the resulting current response. The measured complex impedance reflects the superposition of multiple transport processes occurring within the sample and at its interfaces, each with distinct time constants. The advantage of EIS lies in its capacity to separate these processes based on their frequency-dependent responses, offering insights that are difficult to obtain by DC techniques alone.

In polycrystalline ceramic systems, the total impedance is typically composed of contributions from bulk (grain interiors), grain boundaries, and electrode–material interfaces. To interpret such complex responses, the Brick Layer Model is widely employed [194]. This model conceptualizes the microstructure as a periodic arrangement of cubic grains ("bricks") separated by thin grain boundaries, mimicking the way grains and grain boundaries are distributed in sintered ceramics. In the Brick Layer Model framework, it is assumed that the current flows across a series of alternating high-conductivity (bulk) and low-conductivity (grain boundary) regions. Each of these regions is represented in the equivalent circuit by a resistor–capacitor element, where the resistance corresponds to the ion transport resistance, and the capacitance reflects the dielectric or space charge properties of that specific region.

A typical impedance spectrum obtained from such a system consists of two or more depressed semicircles or arcs in the Nyquist plot, each corresponding to a different conduction process, as illustrate in Figure 3.1. The high-frequency arc generally represents the response of the grain interior, characterized by relatively low resistance and low capacitance. The intermediate-frequency arc is usually attributed to grain boundary conduction, which typically exhibits higher resistance and capacitance due to defect segregation, potential barriers, or secondary phases at grain boundaries. A low-frequency tail or arc, when present, is often associated with electrode polarization and surface processes such as charge transfer, gas adsorption, or diffusion.

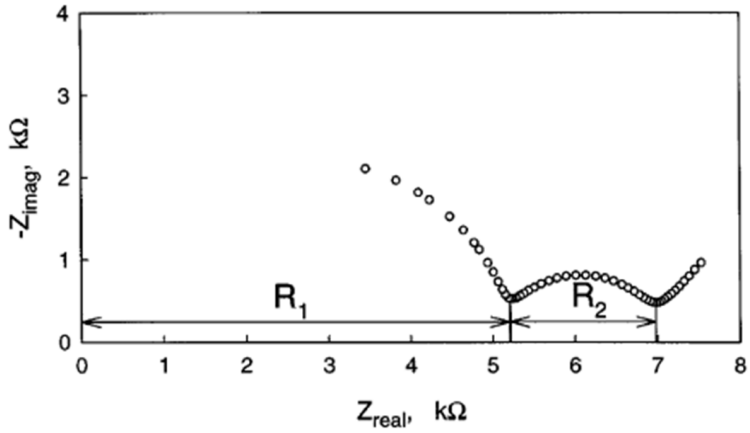

Figure 3.1. A typical Nyquist plot for a polycrystalline material [195].

The separation of these contributions becomes more distinct at elevated temperatures, where the conductivity contrast between bulk and grain boundaries increases. To quantitatively evaluate the individual components, impedance data are fitted to an equivalent circuit model (ECM) using complex nonlinear least squares fitting. From the fitted resistance values, temperature-dependent conductivities of the bulk and grain boundary phases can be extracted, and corresponding activation energies calculated using Arrhenius analysis. This information is crucial for understanding the defect chemistry, transport mechanisms, and microstructural effects on ion conduction in ceramic materials. It is to note that the ECM simply represents the form of the measured Nyquist plot but has no physical meaning.

The EIS characterizations in Chapter 4 were recorded over a temperature range of 150-700 °C using an Alpha -A frequency analyzer in the frequency range 0.1-10^6 Hz. Within the temperature range of 150-250 °C, the testing temperature intervals are set at 25 K. Sputtered Au electrodes were utilized as the current collectors, which are conducive to deconvoluting grain boundary and polarization responses. At elevated temperatures (300-650 °C), the testing temperature intervals were extended to 50 K, and more stable Pt electrodes were employed. In order to make the Pt electrode, Pt paste (EVOCHEM Advanced Materials GmbH) was brushed on the surface of the sample and then annealed at 900 °C for one hour to obtain stable Pt electrodes. The EIS results were collected from high to low temperatures. The equilibration time at each measurement temperature was set to 2 hours. The tests were conducted in wet air. The humidification of the gas was realized by bubbling the gas through water at RT resulting in ca. 3 vol.% H_2O saturation in the gas. The EIS data were finally analyzed by the RelaxIS commercial software.

The current-voltage (I-V) curves and EIS of the fabricated full cells in Chapter 7 were evaluated using a potentiostat (Bio-Logic, VMP- 250) at temperatures ranging from 500 to 700 ◦C. The impedance

spectra were measured at open circuit voltage (OCV) over a frequency range from 0.1-10^6 Hz, with an AC amplitude of 10 mV. Silver-palladium paste and platinum wires were used as current collectors and leads, respectively. Complete cells were mounted and sealed with Pyrex glass in a Probostat (NorECS, Oslo, Norway). In fuel cell mode, the fuel electrode was supplied with humidified H_2 (3 % H_2O) at a flow rate of 100 ml min^{-1}, while the air electrode was exposed to a similar flow rate of ambient air. In electrolysis mode, the air electrode was exposed to wet air (80 % H_2O).

3.2.5 Mechanical Properties and Thermochemical Stability Test

In Chapter 4, the elastic modulus and hardness of the material were determined through the load-displacement curves [196] obtained by the Vickers micro-indentation device HC100 (Fischer, Windsor, USA). 25 micro-indentation tests with 1 N load were conducted for each specimen. The specimens underwent grinding and polishing prior to testing. The thermo-chemical stability tests were carried out through high temperature exposure to various atmospheres and their reaction with the materials could be estimated by any phase composition changes. Three atmospheric conditions including Ar saturated with water vapor at 82 °C resulting in 50 vol.% H_2O, 50 vol.% Ar + 50 vol.% CO_2, and 96 vol.% Ar + 4 vol.% H_2 were applied. In a typical experiment, the sintered pellet was ground into powder and heated up to 700 °C, then the powder was subjected to a 24-hours heat treatment under a specific gas atmosphere. After that, the phase composition of the powder was identified again using XRD and compared to a reference measurement.

Elastic modulus and bending strength were evaluated using a ring-on-ring test configuration (Instron 1362-DOLI, Warren, USA). Disc-shaped samples with a diameter of around 14.5 mm were tested using a loading ring and support ring with diameters 3.43 mm and 9.99 mm, respectively. The loading rate was set to 100 N/min and a Poisson's ratio of 0.24 was assumed for the calculation. For each sample series, 25 samples were tested at room temperature to determine the average elastic modulus, average bending strength, characteristic strength, and Weibull modulus via linear regression analysis. Additionally, three samples per series were tested at elevated temperatures (500 °C and 600 °C) in both air and a reducing atmosphere (3 vol.% H_2/Ar) to determine average fracture stresses.

The ring-on-ring sample testing setup is illustrated in Figure 3.2. Following the international standard procedure ISO 20501, the global elastic modulus is calculated from the linear region of the load-displacement curve using the formula:

$$E = \frac{3(1-\nu^2)\cdot r_1^2\cdot \Delta F}{2\pi\cdot \Delta f\cdot h^3} \times \left[\left(\frac{r_2}{r_1}\right)^2 - 1 - \ln\left(\frac{r_2}{r_1}\right) + \frac{1}{2}\left(\frac{1-\nu}{1+\nu}\right) \times \left(\frac{r_2^2-r_1^2}{r_3^2}\right) \times \left(\frac{r_2^2}{r_1^2}\right)\right] \quad (3.3)$$

where ΔF is the force difference and Δf is the corresponding displacement change within the linear region; v is the Poisson's ratio, h is the specimen thickness, and r_1, $r_2$and r_3 represent the radius of the loading ring, supporting ring, and specimen, respectively.

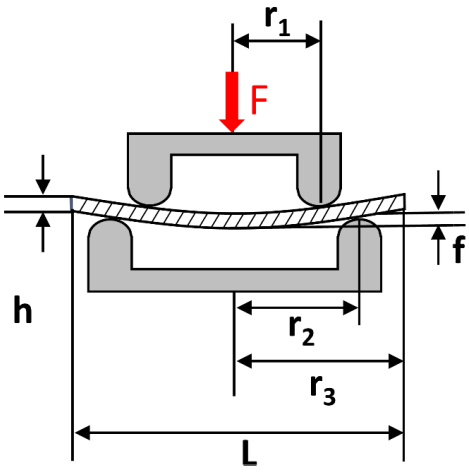

Figure 3.2. Illustration of the ring-on-ring bending test.

The maximum stress is uniformly distributed within the tensile surface area defined by the loading ring, expressed as:

$$\sigma_B = \frac{3(1+\nu)F_B}{2\pi \cdot h^2}\left[\ln\frac{r_2}{r_1} + \frac{(1-\nu)}{(1+\nu)} \times \frac{r_2^2 - r_1^2}{2r_3^2}\right] \quad (3.4)$$

where F_B denotes the fracture load.

4 Characterization of High Zr/Ce Ratio Ba(Zr,Ce,Y)O_{3-d} Proton Conductors

This Chapter comprises the systematic characterization of high Zr/Ce ratio Ba(Zr,Ce,Y)O_{3-d} proton conductors. Particularly, 20 mol.% of Ce was introduced into the lattice of $BaZrO_3$, to maintain certain stability but also counteract with the low grain boundary conductivity. And 0.5 wt.% of NiO was added as a sintering aid. The substituent Y_2O_3 varies within the range of 10-30 mol.%, in order to study the influence of Y on the phase formation, microstructure, and electrical performance. The proton conductivity divided into bulk and grain boundary is discussed separately to explore the effect of Y. In addition, mechanical performance and thermal-chemical stability are also taken into consideration to evaluate the suitability of this material for electrochemical devices.

4.1 Phase Analysis and Microstructure

Fig. 4.1a shows the XRD patterns of materials in the $BaZr_{0.8-x}Ce_{0.2}Y_xO_{3-\delta}$ series recorded at RT. All phases exhibit a cubic perovskite structure with space group Pm-3m. No apparent secondary phases were observed in the XRD patterns. The shoulder to the right of each main peak is Kα2 peak, which is more distinctly separated from the main peak at a higher angle. There is an apparent trend in the XRD patterns that with increasing the Y concentration, the peaks shift towards the smaller angles due to an obvious lattice expansion upon substitution. The reason is that the ionic radius, ri, of Zr^{4+} is 0.072 nm, which is smaller than that of Y^{3+} (ri=0.090 nm). With adding more of the larger Y^{3+}, the inter-planar crystal spacing d will increase upon substitution, and θ will correspondingly decrease, according to the Bragg's law of diffraction, $2d\sin\theta=n\lambda$.

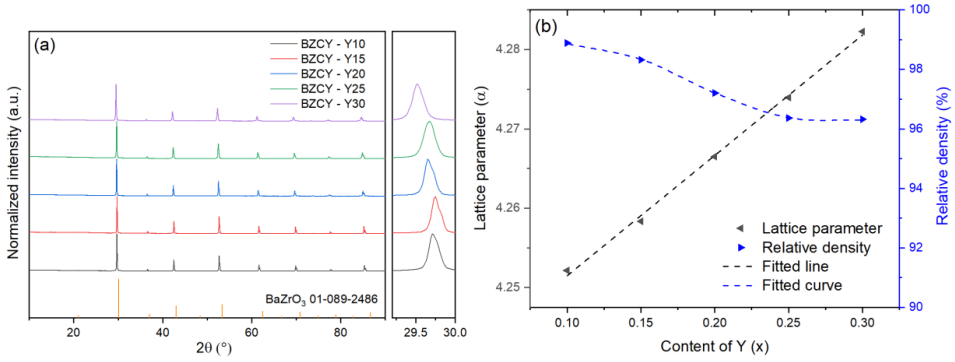

Figure 4.1 (a) XRD patterns of the $BaZr_{0.8-x}Ce_{0.2}Y_xO_{3-\delta}$ ceramics. (b) Lattice parameters and relative density with the increase of Y content. (Fitting results are only visual reference)

All XRD patterns were refined in order to obtain more accurate analysis of the results as shown in Fig. 4.2, the refinement results for all samples exhibited a low weighted profile R-factor (Rwp) and goodness

of fit (Gof), indicating a good match between the calculated results and experimental data. The refinement results provided precise lattice parameters. As mentioned earlier, the ionic radius of Y^{3+} is larger than that of Zr^{4+}, and substitution of Zr^{4+} with Y^{3+} ions will lead to an increase in the lattice parameters. Fig. 4.1b shows the changes in the lattice parameters with increasing Y_2O_3 concentration. The increase in lattice parameters with Y content exhibited a good linear relationship in accordance with the Vegard's law [197] and with single phase composition evidenced by qualitative XRD analysis, which means that even at high concentrations of Y_2O_3, Y^{3+} ions are possible to substitute into the perovskite structure at the given sintering temperature. Meanwhile, Fig. 4.1b also shows that with increasing Y content, the relative density decreased. The observed effect suggests that high concentration of Y_2O_3 had an inhibitory effect on the densification of $BaZr_{0.8-x}Ce_{0.2}Y_xO_{3-\delta}$ during sintering, which will be discussed further combined with the microstructural investigations.

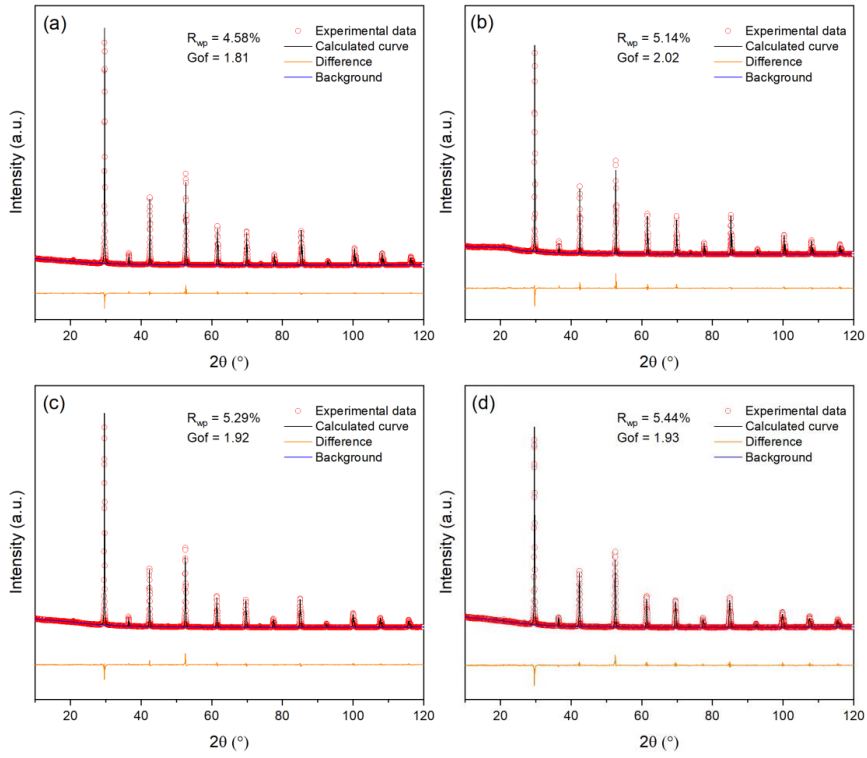

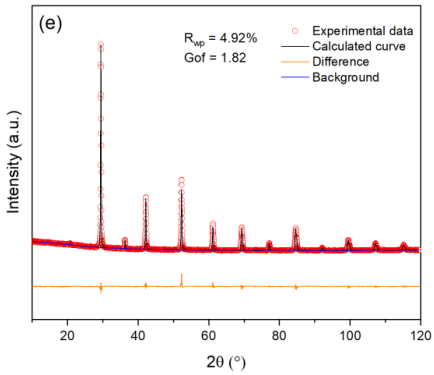

Figure 4.2. XRD patterns of the $BaZr_{0.8-x}Ce_{0.2}Y_xO_{3-\delta}$ ceramics with refined data based on Rietveld method. (a) BZCY – Y10, (b) BZCY – Y15, (c) BZCY – Y20, (d) BZCY – Y25, (e) BZCY – Y30.

The SEM images of polished $BaZr_{0.8-x}Ce_{0.2}Y_xO_{3-\delta}$ ceramics were obtained using a backscattered electron detector (BSD) as shown in Fig. 4.3. As can be seen from the images, the number of pores increases while the Y content increases, which is consistent with the results of the relative density. Moreover, when the Y content is greater than 25%, a secondary phase with different contrast compared to the main phase can be found. In the BZCY-Y30 sample, two typical regions have been identified: one is a relatively dense region, and the other is a relatively porous region. The grain size analysis in Fig. 4.3f reveals that with increasing Y content, the average grain size initially increases and then decreases. In the BZCY-Y30 sample, the grains in the dense region are smaller compared to the grains in the relatively porous region.

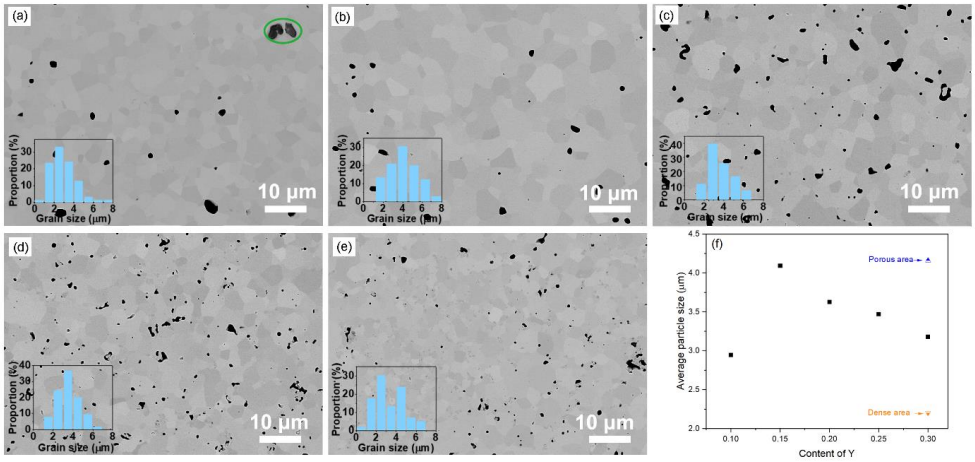

Figure 4.3. (a-e) SEM-BSD images of the polished surface of $BaZr_{0.8-x}Ce_{0.2}Y_xO_{3-\delta}$ ceramics. Inserts show the grain size distribution (a) BZCY–Y10, the marked particles are identified as residual NiO (b) BZCY–Y15, (c) BZCY–Y20, (d) BZCY–Y25, (e) BZCY–Y30. (f) Average grain size as a function of the Y content.

EDS analysis was performed on the BZCY-Y30 sample to determine the composition of the secondary phase. Elemental mapping was applied on a typical area encompassing the relatively dense and relatively porous regions, as shown in Fig. 4.4. The spectrum results show that Ba, Zr, and Ce are uniformly distributed, but there are Y-rich areas. The enrichment observed in the relatively dense and relatively porous regions differs. As shown in Fig. 4.4, the Y-rich phases in the relatively dense region exhibit smaller grain sizes but higher density. Conversely, the Y-rich phases in the relatively porous region show the opposite trend. This non-uniform segregation is likely a result of insufficient homogeneity in the calcined powder before sintering. Additionally, the presence of secondary Y-rich phases is expected to impact mass transfer during the sintering process. This is manifested in the inhibition of grain growth, as observed in the more dense region. The Y-rich particles in the porous region have larger grain size and thus have less surface energy. Owing to the lower driving force for further growth, they tend to anchor between two matrix grains, affecting densification during sintering and preventing the elimination of pores. This can be observed in Fig. 4.4, where the porous region shows large pores always adjacent to the larger Y particles. Although no apparent secondary Y-rich phases were detected in samples with lower Y content, the possibility of trace Y precipitation at grain boundaries, inhibiting grain growth, cannot be ruled out. This also explains the gradual reduction in average grain size when Y content exceeds 15 mol%. However, note that no impurity peaks belonging to the secondary phase were found in the XRD results, indicating that the proportion of the secondary phase was very low (below the XRD detection limit). In addition, the linear relationship between the lattice parameters and Y concentration shown in Fig. 4.1b also indicated that most of the Y was substituted into the main perovskite phase, and only a small amount of Y aggregated to form Y-rich secondary phases.

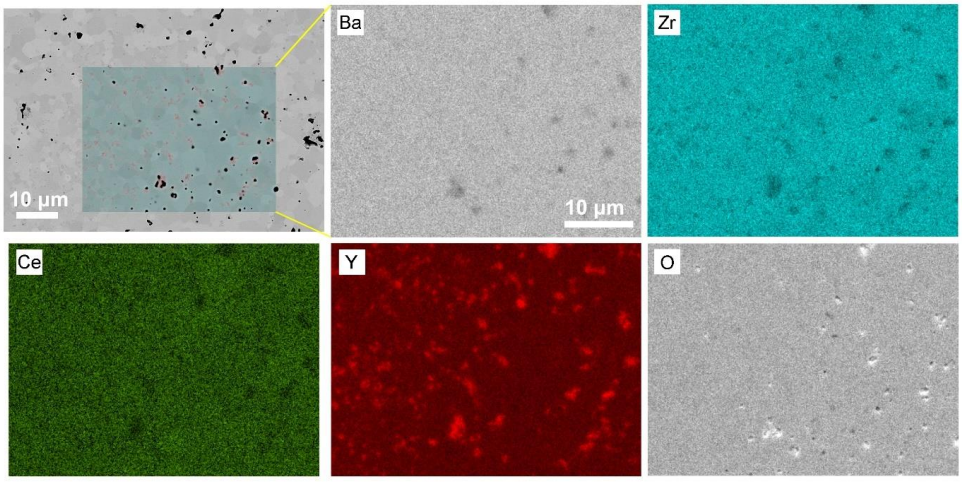

Figure 4.4. Element mapping of the polished BZCY–Y30 specimen.

4.2 Hydration Behavior

Fig. 4.5 depicts the mass change recorded versus time and temperature for the studied $BaZr_{0.8-x}Ce_{0.2}Y_xO_{3-\delta}$ materials, from which the proton concentration can be derived according to Eq. 3.2. Fig. 4.6a additionally illustrates the temperature dependency behavior of the proton concentration. As can be observed in the figure, due to the exothermal nature of the hydration process, as the temperature decreases, the degree of hydration gradually increases. It is also evident that with an increase in the Y content, the generated oxygen vacancies, the proton concentration also gradually rises. The hydration process can be expressed using the following defect equation (Eq. 4.1), from that it is seen that oxygen vacancies and proton concentration are proportionally dependent:

$$H_2O\,(g) + O_O^{\times} + V_O^{\bullet\bullet} \leftrightarrow 2OH_O^{\bullet} \quad (4.1)$$

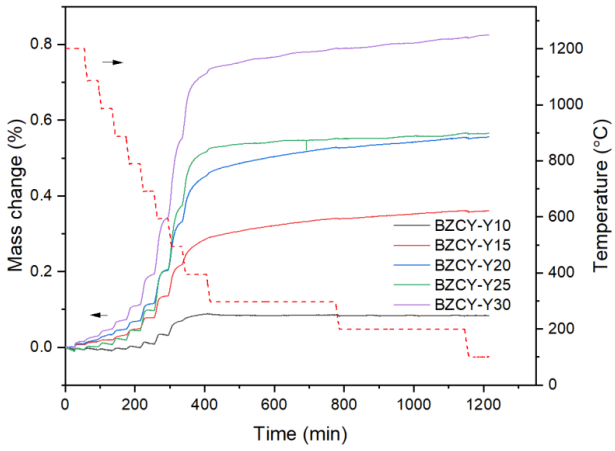

Figure 4.5. Mass change recorded versus time and temperature for materials in the $BaZr_{0.8-x}Ce_{0.2}Y_xO_{3-\delta}$ series.

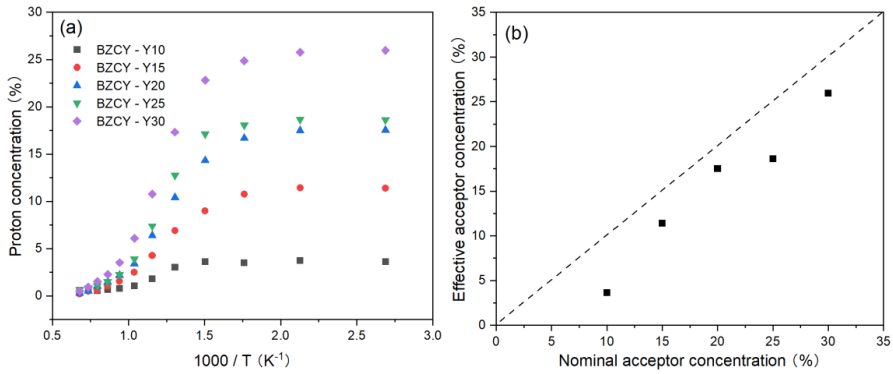

Figure 4.6. (a) Temperature dependency of the proton concentration for the materials in the $BaZr_{0.8-x}Ce_{0.2}Y_xO_{3-\delta}$ series. (b) Effective acceptor concentration versus the nominal acceptor concentration: dashed line shows the theoretical acceptor concentration, while the symbols reflect the experimentally derived effective concentration based on data collected at 100 °C.

Therefore, the proton concentration is highly dependent on the concentration of oxygen vacancies, and the concentration of oxygen vacancies is determined by the content of acceptor Y. This formation of oxygen vacancy can be expressed by the following equation:

$$Y_2O_3 = 2Y'_{Zr} + 3O_O^{\times} + V_O^{\bullet\bullet} \qquad (4.2)$$

Combining Eq. 4.1 and 4.2, it can be noted that two Y atoms generate one oxygen vacancy, and during the hydration process, one oxygen vacancy produces two protons. Therefore, the proton concentration should be theoretically equal to the nominal Y concentration after complete hydration. Here, the proton concentration at 100 °C is considered as the effective acceptor concentration and is plotted against the nominal acceptor concentration as shown in Fig. 4.6b. The dashed line represents the theoretical maximum effective acceptor substituent concentration. It can be observed that the effective substituent concentration increases with an increase in Y content. This suggests that even at high Y concentrations, most of the Y can still effectively substitute into the B-site in the perovskite lattice then generating oxygen vacancies. However, it is worth noting that the effective acceptor concentration is still lower than the theoretical concentration. There are two possible reasons. [111,178] Firstly, SEM analysis indicates that a small amount of Y tends to segregate into a secondary Y-rich phase. Secondly, several studies suggest that the addition of NiO as a sintering aid leads to a lower proton uptake. Huang et al. [117] discussed various reasons for NiO reducing proton concentration, with the most likely being the formation of a liquid phase of (Ba, Ni, Y)O_x during sintering, which consumes Y but also Ba at the A-site of the perovskite. This may lead to a small amount of Y substituting for Ba, forming $Y_{Ba}^{\bullet}$ defects, thereby reducing the effective doping concentration of the substituent.

4.3 Electrical Properties

The electrochemical impedance analysis of the sample BZCY-Y10 is presented in Fig. 4.7 to illustrate the analysis process. At a relatively low testing temperature of 150 °C, two distinct arcs can be identified at high frequencies. The fitting equivalent circuit for these two arcs is shown in Fig. 4.7a. Resistor (R) and constant phase element (CPE) are in parallel, representing the grain interiors or grain boundaries. The two of the R/CPE components are connected in series according to the brick layer model explained in detail by Haile et al. [195] The fitting resulted in obtaining the capacitances of two arcs that can be then assigned to the deconvoluted bulk and grain boundary contributions. For the first arc in the high-frequency region a capacitance of 5.74×10^{-11} F was calculated, while for the second arc the obtained value is 1.38×10^{-8} F, which typically represent the responses of bulk and grain boundary, respectively [194]. When the temperature rises to 200 °C, the fitted capacitance values show consistency (Fig. 4.7b). In this case, it is possible to obtain the resistance of both bulk and grain boundary separately. However, the arcs of bulk and grain boundary gradually overlap at higher temperatures as shown in Fig. 4.7c, and the tail of the grain boundary arc (high frequency) is the only visible part eventually. In this situation, it

is impossible to separately obtain the electrochemical responses of bulk and grain boundary. Only the total resistance value can be estimated by the intercept of the tangent line of the tail of the grain boundary arc with the real axis. The grain conductivity and the total conductivity can be calculated by the following equation:

$$\sigma = \frac{L}{RS} \quad (4.3)$$

Where L is the thickness of the sample, R is the resistance and S is the cross-sectional area. When calculating the grain boundary conductivity, there are two different definitions: one is the apparent grain boundary conductivity (σ_{gb_ap}), which is also calculated using Eq. 4.3 as mentioned above. However, the grain boundary is associated with a particular effective thickness that considering in conductivity calculation leads to the so-called specific grain boundary conductivity (σ_{gb_sp}). Assuming that the dielectric constants of the bulk and grain boundary are consistent, the specific grain boundary conductivity can be calculated using the following equation [32]:

$$\sigma_{gb\_sp} = \frac{L}{S}\left(\frac{C_g}{C_{gb}}\right)\frac{1}{R_{gb}} \quad (4.4)$$

Where C_g and C_{gb} are the capacitance of grain interior and grain boundary respectively, calculated from the fitted CPE results based on following equation:

$$C = \left(\frac{Q}{R^{\alpha-1}}\right)^{1/\alpha} \quad (4.5)$$

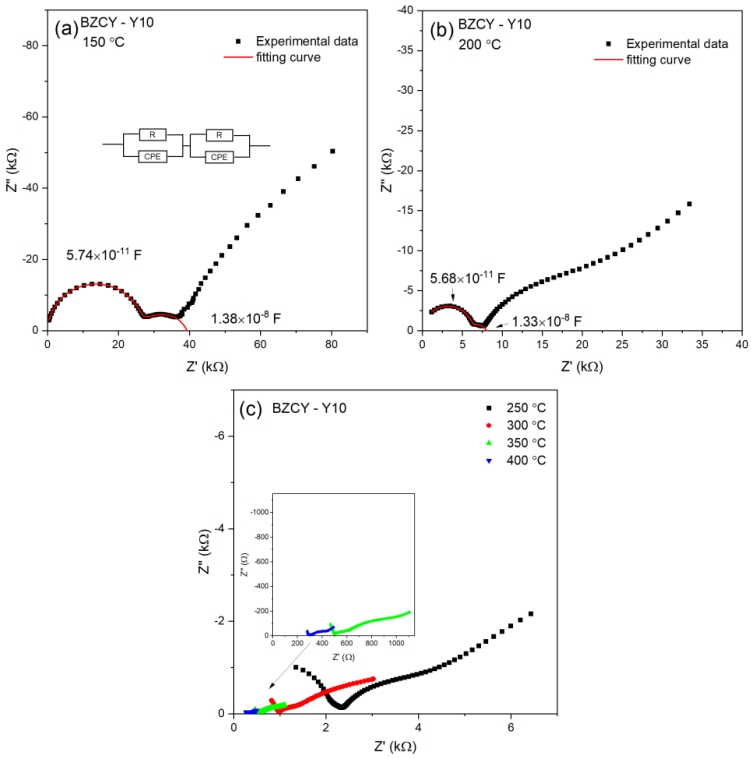

Figure 4.7. Nyquist plots of BZCY-Y10 at elevated temperature. (a) 150 °C. (b) 200 °C. (c) 250 – 400 °C.

Based on the analysis and calculation of the electrochemical impedance spectroscopy results mentioned above, an Arrhenius plot of the total conductivity of the BZCY sample can be obtained as shown in Fig. 4.8a. Data for the BZCY-30 sample above 250 °C are not available due to sample disintegration at elevated temperatures caused by chemical expansion combined with thermal expansion. Except for BZCY-30, the total conductivity of the remaining samples increases with increasing the Y content over the studied temperature range. The total conductivity data at 600 °C in humid air are summarized and presented in Table 4.1.

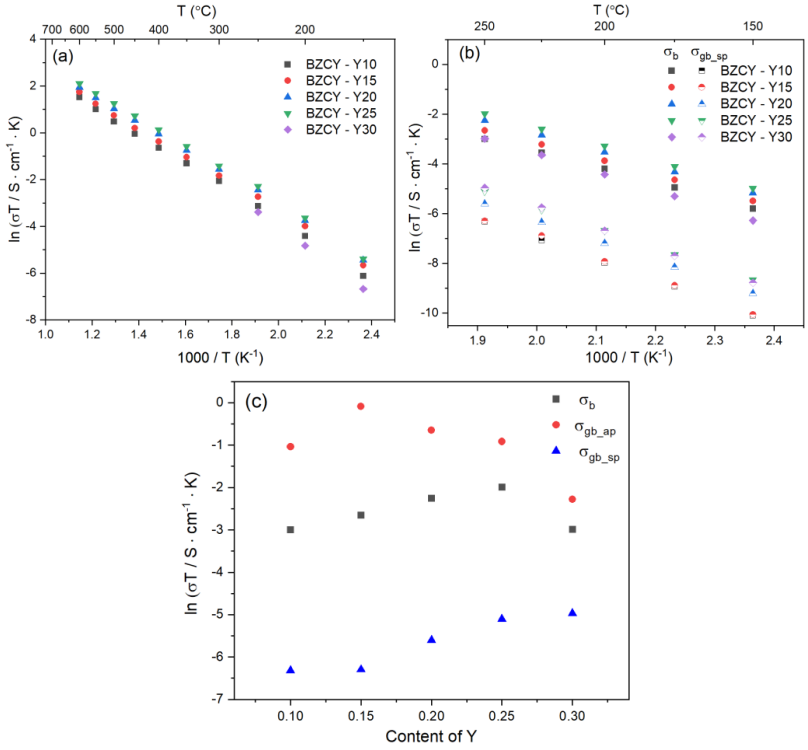

Figure 4.8. Conductivity of materials in the $BaZr_{0.8-x}Ce_{0.2}Y_xO_{3-\delta}$ series: (a) Arrhenius plots of total conductivity in the temperature range 150-600 °C under humid air, (b) Arrhenius plots of bulk (full symbol) and specific grain boundary (half symbol) conductivities in the temperature range 150-250 °C, (c) bulk, apparent and specific grain boundary conductivities as a function of Y content at 250 °C.

The conductivities of bulk and grain boundary at temperatures below 250 °C were obtained by fitting EIS. Arrhenius plots of bulk conductivity and specific grain boundary conductivity are shown in Fig. 4.8b. By linear fitting, the activation energies of bulk and grain boundary can be obtained as shown in Table 4.1. With increasing the Y content, the activation energy of the bulk increases slightly, and the activation energy of BZCY-Y30 is significantly higher than that of other low Y concentration samples. The variation in activation energy of grain boundary shows no clear compositional trend. Furthermore, three of the BZCY-Y10 samples were selected to confirm the experiment reproducibility. The result is

shown in Figure 4.9. The variation of both σ_b and σ_{gb_sp} for these three samples are in an acceptable range.

Table 4.1 Summary of conductivity and activation energy data for materials in the $BaZr_{0.8-x}Ce_{0.2}Y_xO_{3-\delta}$ series based on the EIS analysis. Total conductivity at 600 °C in humid air; activation energy of bulk and grain boundary conductivity at 100-250 °C; bulk conductivity, apparent and specific grain boundary conductivity at 250 °C.

	BZCY-Y10	BZCY-Y15	BZCY-Y20	BZCY-Y25	BZCY-Y30
Total Conductivity at 600 °C ($S \cdot cm^{-1}$)	5.3×10^{-3}	6.6×10^{-3}	8.0×10^{-3}	9.4×10^{-3}	N/A
Activation energy (from 100-250 °C) of bulk (eV)	0.54	0.54	0.56	0.57	0.63
Activation energy (from 100-250 °C) of grain boundary (eV)	0.72	0.73	0.69	0.68	0.73
σ_b at 250 °C ($S \cdot cm^{-1}$)	9.5×10^{-5}	1.3×10^{-4}	2.0×10^{-4}	2.6×10^{-4}	9.7×10^{-5}
σ_{gb_ap} at 250 °C ($S \cdot cm^{-1}$)	6.8×10^{-4}	1.7×10^{-3}	9.9×10^{-4}	7.7×10^{-4}	2.0×10^{-4}
σ_{gb_sp} at 250 °C ($S \cdot cm^{-1}$)	3.5×10^{-6}	3.5×10^{-6}	7.1×10^{-6}	1.2×10^{-5}	1.3×10^{-5}

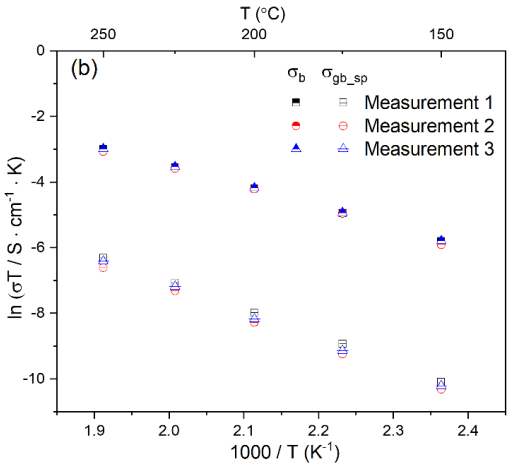

Figure 4.9. (a) Arrhenius plots of bulk and specific grain boundary conductivities of three different BZCY-Y10 samples in the temperature range 150-250 °C.

In order to better understand the effect of the employed different Y contents on the conductivity of the studied BZCY samples, one needs to consider and analyze their bulk and grain boundary conductivities in detail as depicted in Figure. 4.8c.

Bulk conductivity. Fig. 4.8c illustrates the variation of bulk conductivity with Y content at 250 °C. A significant decrease in conductivity is observed for BZCY-Y30, which is related to the excess Y-rich phases observed in the SEM images in Fig. 4.3e. BZCY-Y30 will be excluded in the subsequent discussion regarding conductivity. Except for BZCY-Y30, the bulk conductivity continues to increase with increasing the Y content. The comparison of the conductivity at 250 °C has several advantages. Firstly, as mentioned above, it is difficult to separate the conduction contributions from bulk and grain boundary in EIS at higher temperatures. Secondly, at this temperature, the degree of hydration of BZCY material is nearly at the saturation level, as shown in Figure 4.6a, providing a better reference value when considering proton concentration. Finally, at such a relatively low temperature, the conductivity contribution mainly comes from proton migration rather than other charge carriers such as electrons or oxygen ions [198]. According to the conductivity equation:

$$\sigma = nq\mu \qquad (4.6)$$

n represents the charge carrier concentration, protons in this case, q is the electron charge constant (1.6×10^{-19} C), and μ is the proton mobility. According to Eq. 4.1 and 4.2, as well as the thermogravimetric analysis shown in Fig. 4.6, the proton concentration (n) is directly correlated with the Y substituent concentration. Interestingly, as shown in Table 4.1, as the Y concentration increases, the increase in bulk conductivity follows the same multiplicative relationship with the Y content. Taking BZCY-Y10 as a reference, the bulk conductivity of BZCY-Y15, BZCY-Y20 and BZCY-Y25 is higher than that of the reference by a factor of 1.4, 2.1 and 2.7, respectively. This holds true except for BZCY-Y30. This indicates that the variation in conductivity (σ) with changing Y substituent levels is mostly attributed to the increase in proton concentration (n) due to more Y substitution. In other words, the multiplicative relationship of n directly leads to the same multiplicative relationship of σ in Eq. 4.6, which means the mobility (μ) does not significantly change with Y substitutional concentration. This is also reflected in the almost unchanged activation energy as shown in Table 4.1.

As suggested by Eq. 4.6, apart from the concentration of charge carriers, also their mobility plays an essential role. In literature, two mechanisms describing the influence of Y cations on the proton mobility in BZCY materials are discussed. The first one is the trapping effect of the dopant [93]. In this concept, Y^{3+} acts as an aliovalent dopant on e.g., Zr^{4+} site, thus forming a negative charge center. When a proton migrates to an O-site adjacent to a Y-site, it gets captured there because the energy required for this proton to rotate or migrate within the region is lower than the energy required to migrate out of it [84,199]. This confinement restricts the long-range migration capability of protons. Therefore, Y substitution will be expected to decrease the proton mobility based on the trapping effect theory.

Another mechanism discusses an alternative effect of high Y concentrations on proton long-range migration, which is called the nanoscale percolation effect [98]. The trapping effect of individual Y cation on protons is also acknowledged in this theory. However, as the concentration of Y is high, there

is a probability for Y cations to become adjacent to each other. When protons migrate within such regions formed by continuous Y-sites, the activation energy required is even lower than that for migration to other sites such as Zr-sites. This rapid pathway for protons formed by continuous Y-site is termed the nanoscale percolation effect. Such effect becomes more pronounced at higher Y concentrations. In other words, high concentrations of Y substitution facilitate an increase in proton mobility.

The competitive relationship between these two mechanisms regarding proton mobility, one having a negative impact and the other having a positive impact, collectively contributes to the effect of Y substitution on proton mobility. Considering the experimental results shown in Table 4.1, it is verified that the mobility of protons at 250 °C does not significantly change with increased Y content (from 10 at.% to 0.25 at.%). One may therefore speculate that these two effects have almost equal influence in the BZCY materials. The slight increase in bulk conductivity activation energy as shown in Table 4.1 also confirms this. In the computational work by Toyoura et al. [200], the degree of influence of the trapping effect and percolation effect of dopants on proton mobility was assessed. The authors similarly pointed out that the preferential conduction pathways formed by Y cations moderate the strong trapping effect, resulting in a minor reduction of proton diffusivity and mobility. Moreover, they also noted that interactions between protons could have a negative impact on their mobility [201], but this effect is also counteracted by the Y nanoscale percolation effect.

Most of the studies on the influence of Y on proton mobility are conducted using computational methods, for example density functional theory or molecular dynamics [98,199,200]. In this work, this influence has been demonstrated from an experimental perspective. However, it should be noted that both mechanisms are temperature-dependent [93,98]. This means that one effect may have a stronger influence than the other at different temperatures. Unfortunately, it is not possible to obtain solely bulk conductivity information from EIS at higher temperatures. It can only be demonstrated that at the relatively low temperature of 250 °C, there is a balancing among different mechanisms in this studied BZCY composition, resulting in minor changes in mobility with the increase of Y.

Grain boundary conductivity. The effect of Y content on both the apparent and specific grain boundary conductivities is depicted in Fig. 4.8c. The σ_{gb_ap} is significantly influenced by grain size, as the grain boundary density is directly affected by the average grain size. In fact, the trend of σ_{gb_ap} with Y content in Figure 4.8c matches the grain size variation shown in Fig. 4.3f very well. Therefore, comparing the σ_{gb_sp} can be more helpful for a better understanding of the grain boundary properties. As shown in Fig. 4.8c, the σ_{gb_sp} gradually increases with an increase in Y content.

Investigating the proton conduction across the grain boundary is more complex due to the unique microstructure. To gain better insights into the grain boundary chemistry, the elemental composition of BZCY-Y10 was characterized using STEM-EDS analysis, as shown in Fig. 4.10. A characterization of selected grain boundaries is done here to compare the chemical composition of interfaces discussed in this study to other reports in literature. The selected area of analysis is shown in Fig. 4.10a, b. As shown in Fig. 4.10c and d, Ba, Zr, Ce and O are relatively homogeneously distributed in the adjacent grains with a slight deficiency for Zr and O in the grain boundary areas analyzed. However, the EDS results clearly illustrate the segregation of Y and Ni to the grain boundary that can be explained by the grain boundary space charge layer model [91]. During sintering, positive charge point defects such as oxygen vacancies segregate to the grain boundary due to energetic reasons induced by the structural change of the crystal lattice, forming positive charge grain boundary cores [87]. Consequently, negative charge defects such as Y'_{Zr} and Ni''_{Zr} segregate to the grain boundary to compensate for the positive grain boundary core charge, thus forming an acceptor concentration gradient. Similar segregation effects have been observed in different $BaZrO_3$ based compositions mainly by using atom probe tomography and transmission electron microscopy techniques [87,202–206]. The electrostatic driving force is also the reason why the cations of Zr and Ce did not show obvious segregation at the grain boundaries. The same phenomenon was also confirmed for the high Y concentration sample BZCY-Y30 by STEM-EDS as shown in Fig. 4.11. However, due to the higher bulk concentration of Y on the B-site in this composition, the ratio between Y segregation and bulk concentration is lower.

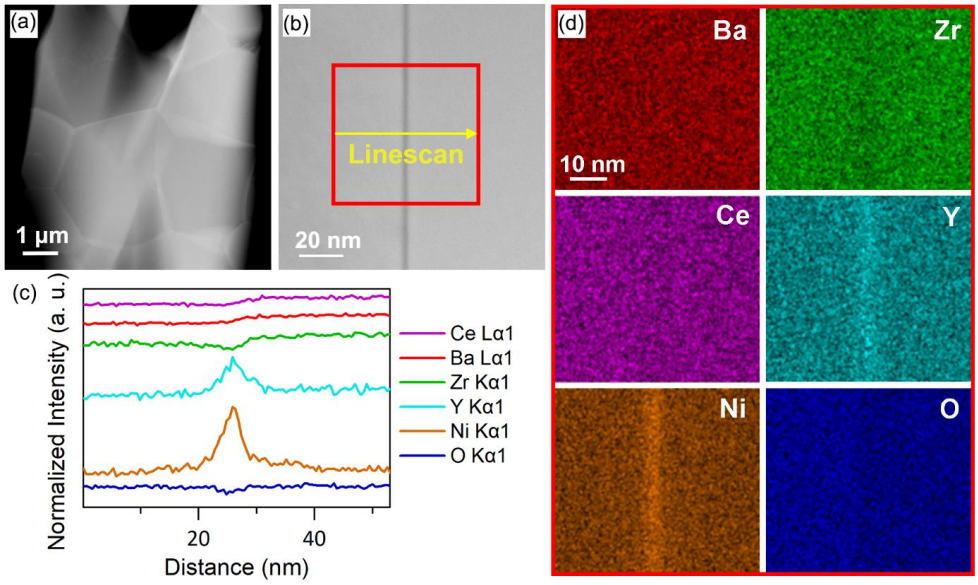

Figure 4.10. (a, b) High-angle annular dark-field images (HAADF) of the BZCY-Y10 microstructure and an edge-on grain boundary (the electron beam is parallel to the grain boundary). (c) Integrated linescan derived from the EDS element mapping in (d).

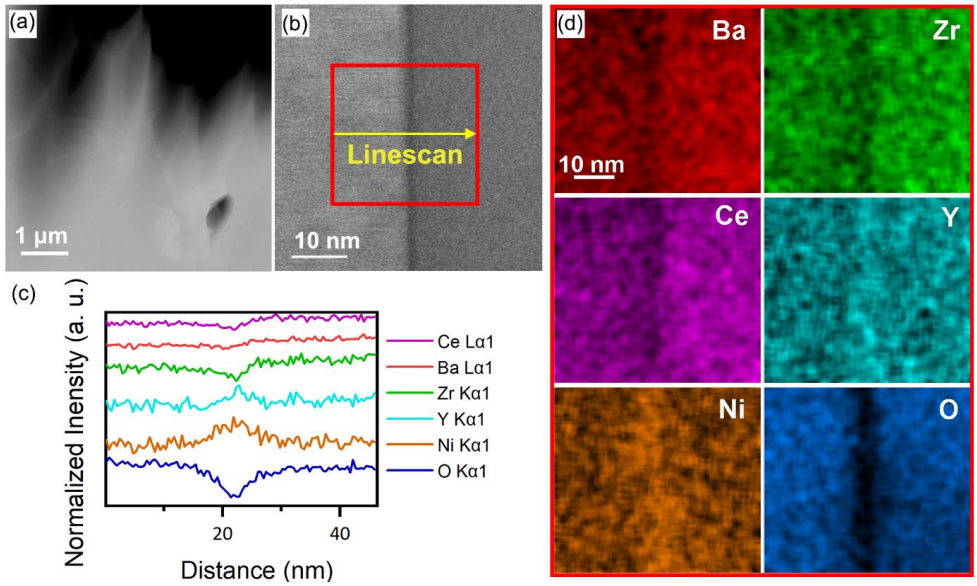

Figure 4.11. (a, b) HAADF of the BZCY-Y10 microstructure and an edge-on grain boundary (the electron beam is parallel to the grain boundary). (c) Integrated linescan derived from the EDS element mapping in (d).

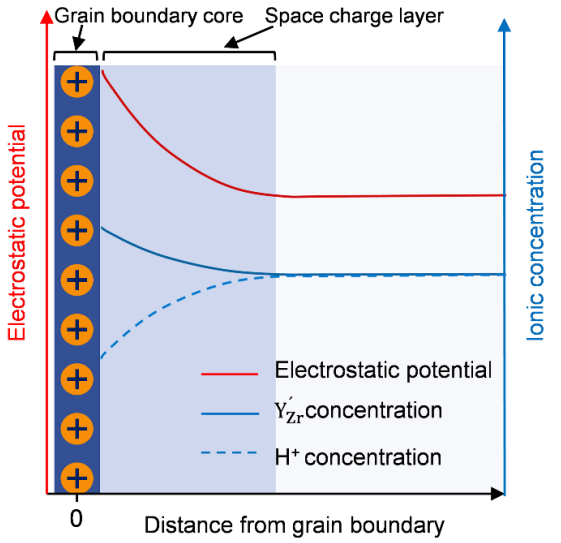

Figure 4.12. Space charge layer model and the corresponding distribution of Y'_{Zr} and $OH^{\bullet}_{o}$ concentrations.

Fig. 4.12 illustrates how such a space charge layer affects proton conduction at the grain boundaries. The positively charged grain boundary core leads to an electrostatic potential difference from the grain boundary core to the bulk, as indicated by the red curve. Under this electrostatic driving force, a

depletion of protonic defects ($OH_O^{\bullet}$) occurs within the space charge layer, as shown by the dashed blue curve. This directly leads to a decrease in grain boundary conductivity. Fortunately, the segregation of Y as shown by the solid blue line partially compensates the electrostatic potential, mitigating proton depletion at the grain boundary. This is also the reason why with increasing Y substitution content, the conductivity at grain boundaries gradually increases as shown in Fig. 4.8c.

The proton conductivity of similar compositions from the literature are plotted in Figure 4.13 to compare the conductivity in this work. For bulk conductivity, our results are within the same order of magnitude as those reported in the literature. However, for grain boundary conductivity, both our results and those from the literature span a wider range. This is because grain boundaries are more significantly affected by the ceramics processing conditions than bulk conductivity.

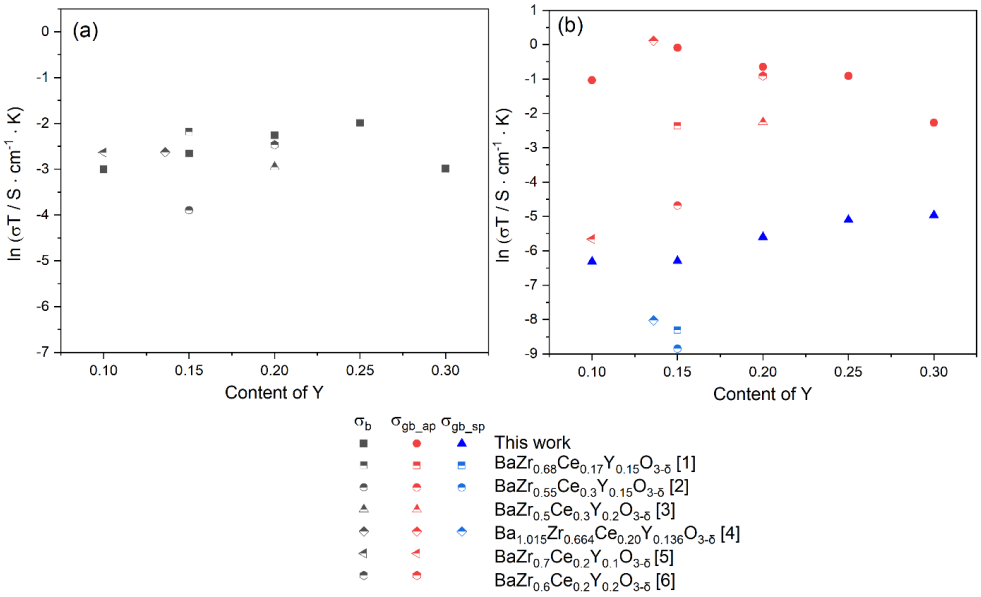

Figure 4.13. (a) Bulk, (b) apparent and specific grain boundary conductivities as a function of Y content at 250 °C, including a comparison of the results from this work with those from literature. References [1-6] in the figure refer to [62,101,118,207–209].

4.4 Mechanical Properties and Thermo-Chemical Stability

In addition to the electrochemical properties, the mechanical performance and thermo-chemical stability of BZCY materials also deserve attention from the perspective of application. Figure 4.14 shows the hardness and elastic modulus of BZCY materials with different Y content. BZCY-Y10 shows similar elastic modulus value as those reported in the literature [210,211]. With the same lattice structure, the increase in lattice parameter due to the Zr substitution with Y generally leads to a decrease in elastic

modulus [210]. Except for BZCY-Y15, the elastic modulus shown in Figure 4.14 does exhibit an overall decreasing trend. The exception for BZCY-Y15 might be related to a grain size dependency of the elastic modulus. The elastic modulus of the grain boundary might differ from that of the grain interior, and different grain sizes can affect the fraction of grain boundary within the indentation area, thus impacting the elastic modulus [212]. The hardness of ceramic materials is influenced by many factors, including grain size and porosity, in addition to the inherent properties of the material [213]. The hardness of BZCY materials remains quite constant within the studied compositional range with values ranging from 8 to 9 GPa.

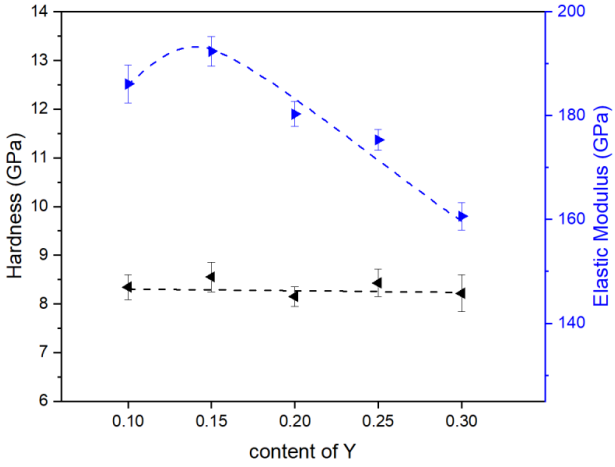

Figure 4.14. Compositional dependence of the micro-indentation hardness and the elastic modulus within the series $BaZr_{0.8-x}Ce_{0.2}Y_xO_{3-\delta}$. (Fitting results are only visual reference)

Next to mechanical properties, the chemical stability of BZCY materials in water and CO_2 containing atmospheres is of significant concern for the durable operation of electrochemical devices based on BZCY ceramics. The element Ba readily reacts with water to form $Ba(OH)_2$ [214], and $Ba(OH)_2$ can easily convert to $BaCO_3$ upon exposure to CO_2 containing atmosphere. Ba can also react directly with CO_2 to form $BaCO_3$ [46]. Fig. 4.15 shows the XRD patterns recorded for BZCY-Y20 exposed to different atmospheres at 700 °C. To better observe potential minor peaks indicating phase instabilities, the intensity is displayed on a logarithmic scale. As expected, BZCY samples with a high Zr/Ce ratio maintain their original perovskite structure after exposure to various atmospheres, with no significant secondary phases detected. Fig. 4.16 presents the XRD patterns of other compositions exposed to different atmospheres. Only the BZCY-Y30 sample exposed to water vapor showed a small amount of $BaCO_3$ phase. As observed from SEM-EDS, the Y-rich secondary phase is present in the BZCY-30 composition, which disbalance the stoichiometry. This increases the A/B ratio in the perovskite structure ABO_3, making the main perovskite phase BZCY to be Ba over-stoichiometric. The Ba over-stoichiometry makes BZCY more prone to degradation reactions [215,216]. Nevertheless, the

compositions studied in the high Zr/Ce ratio series $BaZr_{0.8-x}Ce_{0.2}Y_xO_{3-\delta}$ are proven to have high resistance to H_2, H_2O, and CO_2.

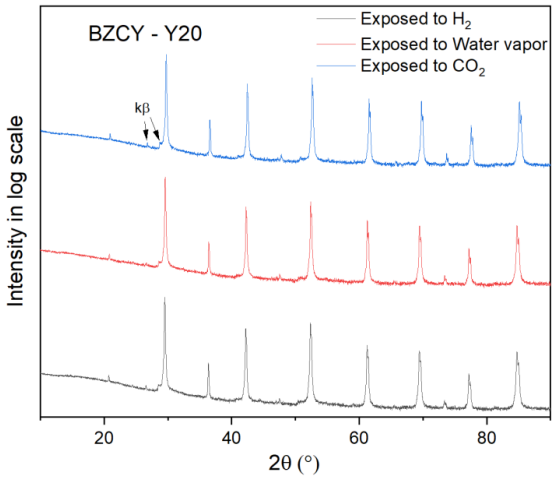

Figure 4.15. XRD patterns of BZCY-Y20 after exposure to H_2, water vapor and CO_2 containing atmospheres at 700 °C. Peak intensity is amplified by log scale.

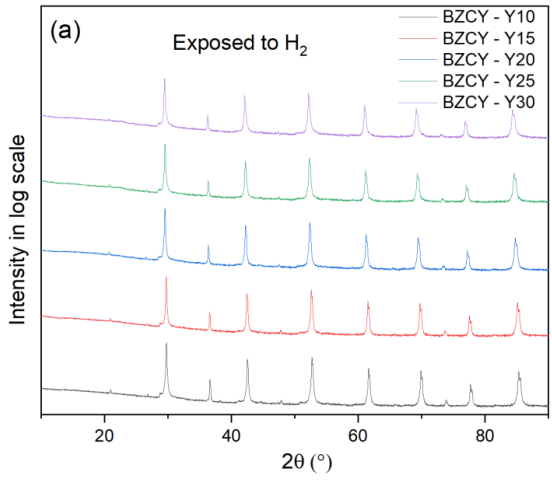

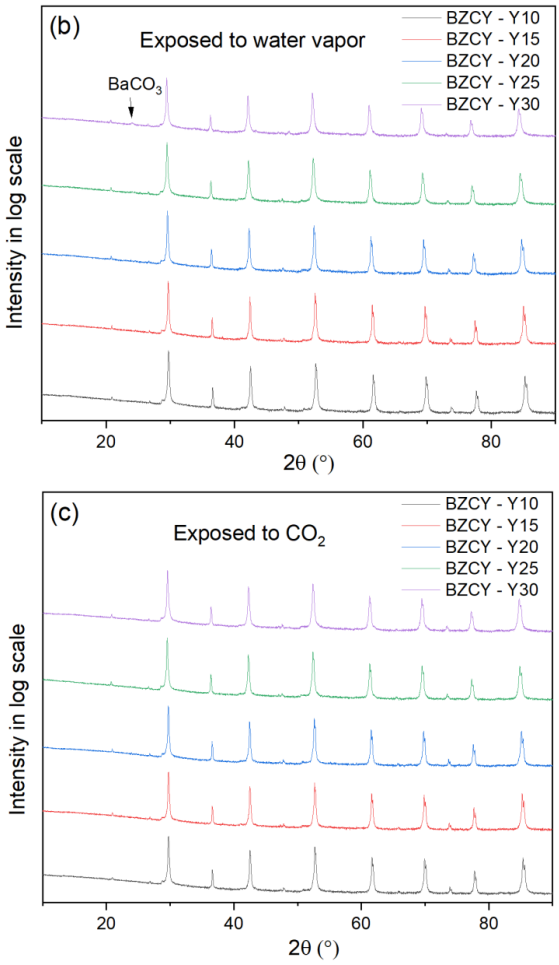

Figure 4.16. XRD patterns of materials from $BaZr_{0.8-x}Ce_{0.2}Y_xO_{3-\delta}$ series after exposure to (a) Ar / 4 vol.% H_2, Ar / 50 vol.% H_2O and Ar / 50 vol.% CO_2 at 700 °C. Peak intensity is amplified by log scale.

4.5 Summary

In this chapter, a systematic study was conducted on the phase composition, microstructure, and the resulting hydration ability and electrochemical performance of high Zr/Ce ratio $Ba(Zr,Ce)O_3$ solid solutions with different Y substitution levels (10 at.% to 30 at.%). Owing to high Zr/Ce ratio, the composition of $BaZr_{0.8-x}Ce_{0.2}Y_xO_{3-\delta}$ exhibited enough thermal-chemical stability for the potential application in electrochemical devices. Within the range of Y substitution concentrations studied, no significant secondary phases were detected in the XRD analysis. However, SEM analysis revealed the presence of Y-rich phases in samples with high Y substitution content. The proton conductivity is strongly related to the concentration of the acceptor Y. More Y means higher conductivity, primarily due to the higher proton concentration resulting from the increased Y content. From the EIS analysis

results, the proton mobility in the bulk is almost independent of the Y concentration when Y is less than 25 at.%, indicating a balance between different mechanisms influencing proton migration, such as the Y trapping effect and the Y nanoscale percolation effect. High Y substitution also contributes to higher grain boundary conductivity, as Y segregation promote the proton conduction based on the space charge layer theory. However, this does not mean that more Y is always better, as excessive Y content can lead to the formation of secondary phases due to solubility saturation, which adversely affects both conductivity and stability. Therefore, 20 at.% of Y content is the optimal substitution concentration to ensure the highest conductivity without formation of secondary phases.

5 Mechanical Properties of the Fuel Electrode Support

In this chapter, the bending strength and elastic modulus of BZCY-Y15/NiO fuel electrode supports were investigated to examine the effects of varying sintering temperature as well post-reduction conditions. Considering the superior thermochemical stability of high Zr content compositions and the reduced risk of secondary phase formation at moderate Y substitution levels [52,53,176], BZCY-Y15 was selected as the focus of this study. The influence of porosity on mechanical performance was analyzed through SEM image analysis and quantitatively modeled using exponential decay relationships. Fracture origins and microstructural failure mechanisms were further revealed through SEM-based fractography. Finally, we evaluated the mechanical reliability of the supports by Weibull statistics analysis and benchmarked their performance against conventional YSZ/NiO-based systems. This study aims to address the knowledge gap in the mechanical reliability of BZCY-based fuel electrode supports and provide practical insights and guidance for future structural optimization and material design.

5.1 Phase Analysis and Microstructure

The XRD patterns of the fuel electrode supports sintered at different temperatures and post-reduction are shown in Figure 5.1. Analysis of the diffraction patterns confirms that all samples, regardless of the sintering temperature, predominantly consist of the cubic perovskite phase BZCY alongside the NiO phase. No secondary or impurity phases were detected, indicating high phase purity. The sample sintered at 1450 °C was selected for further reduction. Post-reduction XRD analysis reveals that NiO is successfully transformed into metallic Ni, with no significant formation of any additional phases. This confirms that all samples maintain their structural integrity and can be classified as “XRD-pure”.

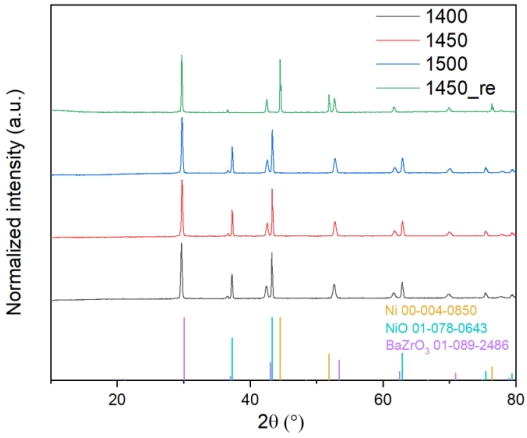

Figure 5.1. XRD patterns of BZCY/NiO fuel electrode supports sintered at 1400 °C, 1450 °C and 1500 °C. The sample labeled 1450-re refers to the 1450 °C-sintered sample after reduction in 3 vol.% H_2/Ar at 900 °C.

Figure 5.2 shows the SEM-BSE (backscattered electron) images of the BZCY-Y15/NiO(Ni) fuel electrode supports after various thermal and chemical treatment processes. In backscattered mode, regions with elements of higher atomic numbers appear brighter. Accordingly, in these micrographs, black areas represent pores, bright areas correspond to BZCY-Y15 phases, and the intermediate gray areas indicate NiO or metallic Ni phases, depending on the treatment.

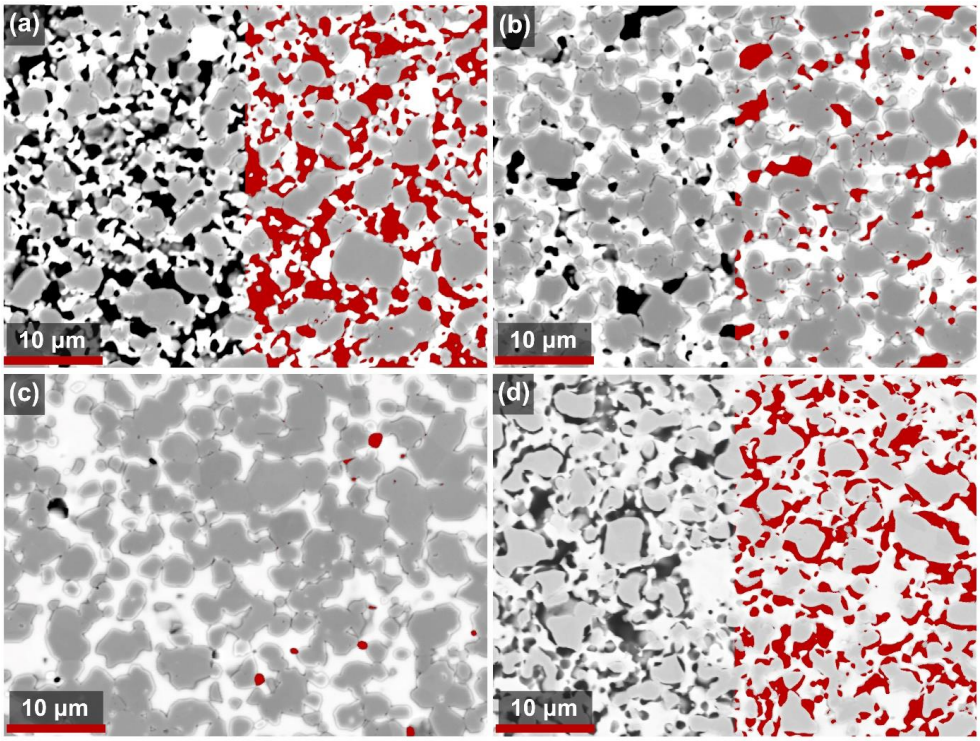

Figure 5.2. SEM images of BZCY-Y15/NiO fuel electrode supports sintered at 1400 °C, 1450 °C, and 1500 °C (a-c), and after reduction at 900 °C following sintering at 1450 °C (d). In each image, the right half is highlighted in red to indicate the pore regions identified by ImageJ/Fiji software during porosity analysis.

It can be observed that with increasing sintering temperature, the porosity gradually decreases. At these three sintering temperatures, there is no significant difference in the size and morphology of the NiO particles. The BZCY-Y15 particles seem to exhibit a better connection (enhanced necking) and densification at higher sintering temperatures, suggesting improved interparticle bonding. Furthermore, the porosity of 1450_re increases compared to the unreduced 1450 °C sample due to the reduction-induced phase transformation of NiO to metallic Ni, associated also with volume shrinkage.

Given the significant impact of porosity on mechanical performance, accurate quantification of porosity is crucial. In each SEM image, the pores on the right half are highlighted in red, illustrating the process by which ImageJ/Fiji identifies the pores based on grayscale contrast. The software then calculates the

area fraction occupied by pores and determines a porosity level. Porosity values were statistically evaluated by analyzing 10 randomly selected regions from SEM images of each sample, with the results summarized in Figure 5.3.

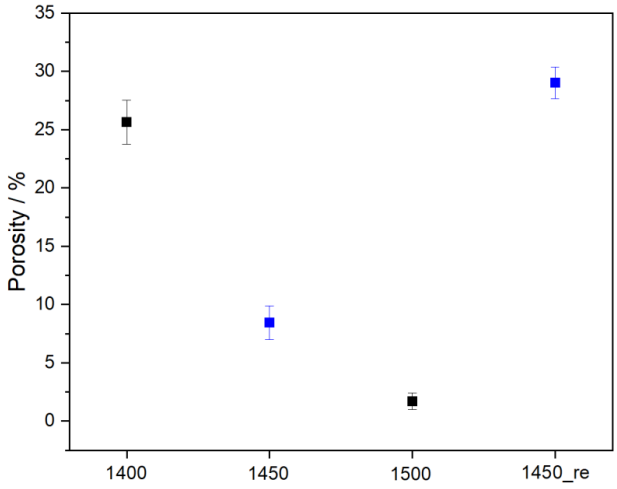

Figure 5.3. Porosity variation of BZCY/NiO fuel electrode supports under different thermal treatment histories.

5.2 Mechanical Properties and Weibull Statistical Analysis

Figure 5.4a shows the average bending strength and elastic modulus values derived from 25 room-temperature bending tests for each BZCY-Y15/NiO fuel electrode support subjected to different heat treatment histories. A clear trend emerges from these results, with both average bending strength and elastic modulus showing significant increase as the sintering temperature rises. This enhancement in mechanical properties is attributed primarily to the corresponding reduction in porosity observed at higher sintering temperature, which leads to a denser and structurally more robust material.

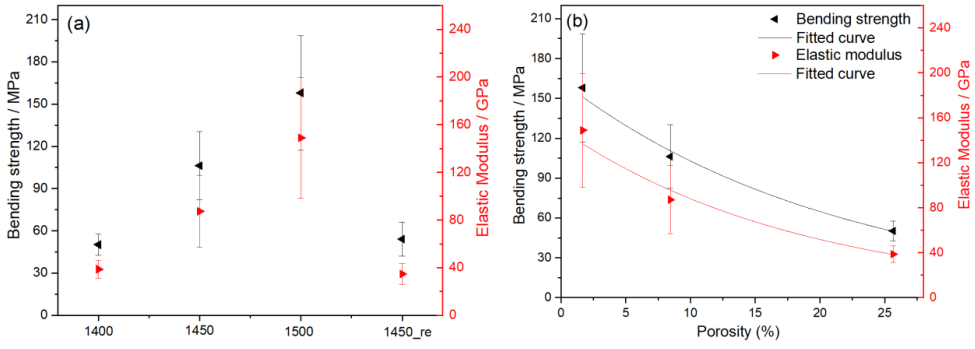

Figure 5.4. (a) Bending strength and elastic modulus variation of BZCY-Y15/NiO fuel electrode supports under different thermal treatment histories. (b) The dependence of bending strength and elastic modulus on porosity.

Conversely, the sample sintered at 1450 °C followed by reduction at 900 °C demonstrates a notable decrease in both bending strength and elastic modulus. This decline is attributed to the introduction of porosity due to the reduction of NiO to Ni, thereby weakening the overall structure and compromising the mechanical strength of the support. The related mechanical data are listed in Table 5.1.

Table 5.1. Result of the ring-on-ring test at room temperature. E is the elastic modulus. σ_b is the average bending strength. σ_c and m are characteristic strength and Weibull modulus with confidence interval obtained from Weibull analysis.

	Porosity (%)	E (GPa)	σ_b (MPa)	σ_c (MPa)	m	No. of test
1400	25.6 ± 1.9	39 ± 7	50 ± 7	53^{56}_{51}	$7.6^{9.3}_{5.5}$	25
1450	8.5 ± 1.4	87 ± 30	106 ± 24	116^{124}_{108}	$5.3^{6.5}_{3.8}$	25
1500	1.7 ± 0.7	149 ± 51	158 ± 41	174^{189}_{159}	$4.3^{5.3}_{3.1}$	25
1450_reduced	29.0 ± 1.4	35 ± 9	54 ± 12	59^{63}_{55}	$5.4^{6.7}_{3.9}$	25

Figure 5.4b illustrates a strong correlation between the magnitude of bending strength and elastic modulus with the level of porosity. Although various microstructural changes can occur with increasing sintering temperature, porosity appears to be the dominant factor influencing the mechanical performance across the investigated sample set. To visualize this macroscopic trend, the porosity dependence of the Young's modulus and bending strength was described by the Equation 5.1 and 5.2 [217,218]:

$$E = E_0 \cdot \exp(-a \cdot P) \qquad (5.1)$$

$$\sigma_b = \sigma_0 \cdot \exp(-b \cdot P) \qquad (5.2)$$

where E_0 and σ_0 are the elastic modulus and bending strength when the porosity is 0. The experimental data can be fitted with E_0 = 149 GPa, a = 0.05, σ_0 = 163 MPa and b = 0.05. This empirical fitting is not intended to serve as a detailed physical model but rather to capture a general trend observed in the experimental data. It emphasizes the strong influence of porosity on mechanical strength while acknowledging that other sintering-related factors, e.g., grain connectivity or local composition changes, may also play a secondary role.

Strength is commonly employed as the critical design criterion for the mechanical limits of brittle ceramic materials. However, the measured strength values exhibit significant statistical scatter due to the influence of flaw size distribution. This inherent variability can be effectively characterized by Weibull statistics [219], which has become one of the most prevalent statistical tools for analyzing fracture strength in ceramic materials, particularly for defect-dominated failure mechanisms. The two-parameter Weibull distribution is mathematically expressed as [220]:

$$P_f = 1 - \exp\left[-\left(\frac{\sigma}{\sigma_c}\right)^m\right] \qquad (5.3)$$

where P_f represents the cumulative failure probability at applied stress σ, σ_c denotes the characteristic strength corresponding to 63.2% failure probability, and m is the Weibull modulus quantifying strength distribution uniformity. A higher m value indicates superior reliability through narrower strength distribution, while lower m values reflect increased strength variability caused by diverse critical flaws.

Figure 5.5 presents the Weibull statistical analysis with 90% confidence intervals for the bending strength of BZCY-Y15/NiO(Ni) fuel electrode supports processed under different sintering conditions. The failure probability (P_f) was logarithmically transformed according to classical two-parameter Weibull methodology for linear regression analysis. The Weibull parameters derived in Table 5.1 reveal an inverse correlation between sintering temperature and Weibull modulus. Specimens sintered at elevated temperatures exhibited decreased Weibull moduli, indicating broader strength distributions.

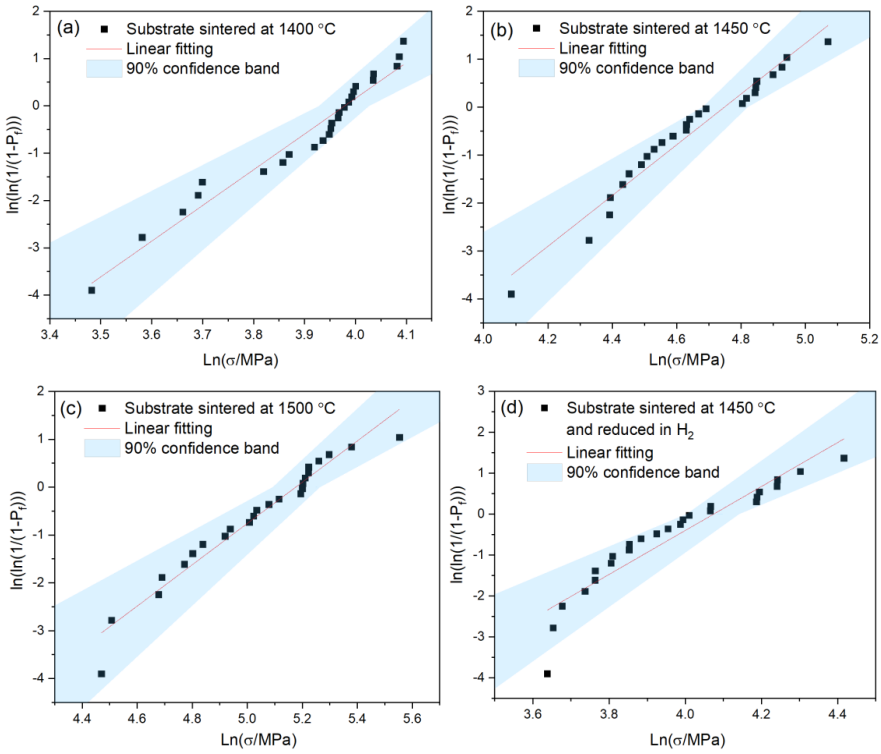

Figure 5.5. Weibull plots with confidence intervals. (a)1400, (b) 1450, (c)1500 and (d)1450_re.

This trend suggests fundamental microstructural differences that 1400 °C-sintered specimens demonstrated relatively uniform porosity distribution acting as stress-concentrating failure origins, resulting in tighter strength clustering. Conversely, higher temperature processing appears to promote anomalous critical flaws, potentially through exaggerated grain growth or heterogeneous pore

coalescence. These irregular defects create weak links in the microstructure, introducing greater strength variability and consequently reducing the Weibull modulus.

To investigate the critical flaws responsible for strength degradation and elucidate the origin of increased strength dispersion in high-temperature sintered specimens, the fracture surface was characterized by SEM, as illustrated in Figure 5.6. The fracture surface of specimens sintered at 1400 °C (Fig. 6a) reveals agglomerated BZCY-Y15 particles without detectable macroscopic pores. When the sintering temperature increased to 1450 °C (Fig. 6b), elongated continuous pores were observed along the periphery of these BZCY agglomerates. This phenomenon became more pronounced with further temperature elevation to 1500 °C (Fig. 6c), where extensive pore networks developed.

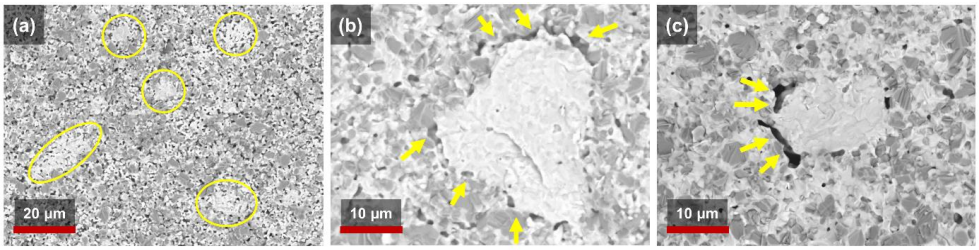

Figure 5.6. SEM images of the fracture surface of BZCY-Y15/NiO fuel electrode support sintered at (a) 1400 °C, (b) 1450 °C and (c) 1500 °C. The yellow circles in (a) mark the agglomeration of BZCY particles, and the arrows in (b) and (c) mark the elongated continuous pores around the BZCY material phase.

The formation mechanism can be attributed to differential sintering rates between the BZCY-Y15 agglomerates and surrounding matrix particles during thermal processing. This mismatch induces heterogeneous shrinkage, generating localized stress concentrations that evolve into elongated pores. Such pores act as preferential stress concentrators under mechanical loading, serving as critical failure initiation sites. Crucially, the stochastic spatial distribution of these pores introduces inherent variability in strength-limiting flaw sizes and geometries. This microstructural heterogeneity provides an explanation for both the widened strength distribution and reduced Weibull modulus observed in higher temperature sintered specimens.

To evaluate the operational reliability of BZCY-Y15/NiO fuel electrode supports, the high-temperature fracture strength of specimens sintered at 1450 °C was investigated at protonic ceramic fuel cell operating temperatures. Mechanical testing was conducted at 500 °C and 600 °C as well as on reduced-state specimens. Due to the time-intensive nature of high-temperature testing, a limited dataset of three samples per condition was acquired. The measured bending strength and elastic modulus values are summarized in Table 5.2, with comparative analysis against room-temperature performance.

Table 5.2. Comparison of the room-temperature and high-temperature mechanical properties of pre-reduction and post-reduction samples sintered at 1450 °C.

	Testing temperature (°C)	E (GPa)	σ_b (MPa)	No. of test
1450	RT	87 ± 30	106 ± 24	25
	500	121 ± 12	137 ± 26	3
	600	87 ± 13	121 ± 6	3
1450_reduced	RT	35 ± 9	54 ± 12	25
	500	33 ± 5	61 ± 13	3
	600	41 ± 12	65 ± 14	3

Notably, both bending strength and elastic modulus exhibited no degradation across the evaluated temperature range compared to ambient conditions. There appears to be even a tendency towards a slight improvement. This anomalous behavior may originate from two potential factors: (1) statistical uncertainty inherent to small sample amount, and (2) thermally induced hydration or dehydration of the BZCY phase that could potentially influence the mechanical performance [221,222]. However, the mechanistic relationship between hydration kinetics and mechanical response remains ambiguous and warrants further investigation. Nevertheless, the results show that the BZCY-Y15/NiO substrate is not expected to exhibit special high temperature mechanical failures in the operating condition.

5.3 Comparison with YSZ/NiO substrate

A comparison of the characteristic strengths between 1450 °C-sintered BZCY-Y15/NiO and conventional YSZ/NiO oxygen-ion conductor half-cells is summarized in Table 5.3. Specimens sintered at 1450 °C were selected for this comparative analysis due to their optimal porosity for fuel electrode support applications and compatibility with commonly used co-sintering temperatures for electrolyte integration. Notably, the BZCY-Y15/NiO system demonstrates significantly lower bending strength than YSZ/NiO counterparts, particularly in the reduced state. This mechanical deficiency poses twofold challenge: the pre-reduction weakness increases susceptibility to structural failure during manufacturing and stack assembly, while the post-reduction strength degradation raises concerns about long-term operational stability, especially during thermocycling. These observations align with prior reports highlighting low mechanical properties in BZCY-Y15/NiO substrate [14,169,223]. The bending strength of 50 MPa in our 1400 °C sample and 106 MPa in our 1450 °C sample is reasonably consistent with the 58.5 MPa reported by Huang et al. [169] and 55.3 MPa reported by Wang et al. [223], given differences in porosity and testing methods. Despite the growing interest in scaling up BZCY-based protonic ceramic electrochemical cells, mechanical reliability remains an under addressed issue that could hinder their technological advancement.

Table 5.3. Comparison of characteristic strengths (MPa) of BZCY-Y15/NiO (1450 °C) and conventional YSZ/NiO fuel electrode supports

Condition	BZCY-Y15/NiO	YSZ/NiO [141]	YSZ/NiO [164]
Oxidized	116	175	240
Reduced	59	165	157

Fractographic analysis in Figure 5.6 suggests potential optimization pathways through microstructural engineering. Improved compositional homogeneity achieved via optimized processing parameters may mitigate heterogeneous shrinkage-induced defects. Furthermore, tuning of the Zr/Ce ratio in BZCY could influence sintering behavior [53,207], possibly leading to enhanced mechanical properties, although this remains speculative and requires validation. An alternative approach proposed by Huang et al. [169] involves a bilayer architecture combining YSZ/NiO as the structural support and BZCY/NiO as the functional electrode layer. This hybrid design improves mechanical robustness compared to BZCY/NiO systems while maintaining comparable electrochemical performance. Another strength enhancing idea might be the use of fiber reinforcement which will be the topic of the PhD thesis of F. Lang at IMD-2.

5.4 Summary

This chapter presents a comprehensive mechanical evaluation of BZCY-Y15/NiO fuel electrode supports for proton-conducting ceramic cells. Both bending strength and elastic modulus increased with higher sintering temperature, primarily due to reduced porosity and improved densification. However, significant mechanical degradation was observed following reduction, attributed to the formation of internal pores resulting from the NiO-to-Ni transformation. Weibull statistical analysis revealed that higher sintering temperatures led to more heterogeneous flaw distributions, reducing mechanical reliability. SEM analysis of fracture surfaces confirmed that abnormal pore networks acted as critical stress concentrators in high-temperature specimens. Despite recent advancements, the mechanical strength of BZCY/NiO remains notably inferior to that of conventional YSZ/NiO systems, particularly in the reduced condition, posing serious challenges for scale-up to stack-relevant sizes and long-term structural stability and reliability. Future efforts should focus on microstructural optimization, compositional tuning (e.g., Zr/Ce ratio), and the development of hybrid support architectures to enhance mechanical robustness in real-world applications.

6 Deposition of Thin and Uniform Electrolyte Layer via Wet Powder Spraying

Among various powder deposition methods for preparing ceramic oxide thin films, tape casting and screen printing are the most commonly used techniques for fabricating the electrolyte layer for SOCs [144,224–229]. This is mainly for two reasons. First, these methods produce films with a thickness well-suited for SOCs electrolyte layers, typically around 10 µm. Secondly, both methods are scalable for large-scale production. Wet powder spraying (WPS) also shares these two advantages, but its potential for fabricating electrolyte layers has been largely underestimated. Research on using WPS to prepare SOCs electrolyte layers is much less extensive compared to tape casting and screen printing [126,131,146–148,159,160,226,230–235]. Moreover, WPS can be applied not only to planar SOC but also to tubular SOC designs.

The process of depositing thin electrolyte powder layers via WPS involves numerous parameters that require exploration. The first key step is the preparation of the suspension used for spraying. In most studies, organic functional additives such as dispersants and binders are essential. Dispersants are used to maintain the stability of the suspension and prevent powder agglomeration in the liquid. Binders enhance the adhesion between powder particles. More importantly, an appropriate amount of binder can alleviate drying stress after coating, preventing drying cracks. However, these organic additives decompose during sintering, leaving behind pores that have negative impact on the densification of the film.

The WPS technique introduced in this chapter utilizes a suspension composed solely of ethanol and ceramic powder, simplifying the preparation process and reducing overall manufacturing costs. The suspension does not need to maintain long-term stability or resist agglomeration. Ultrasonic treatment before spraying is sufficient to disperse the powder and meet the requirements for WPS, avoiding the need for dispersants. Although omitting binders introduces the challenge of drying cracks, this can be addressed by adjusting the spraying parameters. When the suspension has a high solid content and the liquid loading rate during spraying is high, a large amount of suspension will be deposited on the substrate during each spraying pass. In this case, the drying process of the wet layer is similar to that of screen printing or tape casting, where the coating dries from the surface first and then gradually throughout the entire layer. This creates a gradient of drying stress, making drying cracks likely. Under these conditions, the use of binders is necessary. However, for depositing relatively thin electrolyte layers, WPS parameters can be modified to fundamentally alter the drying process. Specifically, by significantly reducing the solid content of the suspension and the liquid loading rate. After each spraying pass, a very thin deposited wet layer dries individually before the next spraying pass. This approach

significantly reduces drying stress along the thickness direction. The desired layer thickness can be finally achieved through multiple spraying passes.

Based on this WPS process, various parameters were explored, which is the main focus of this chapter. The aim is to achieve a sintered electrolyte layer that is dense and crack-free. The occurrence of drying cracks in the coating layer after WPS directly determines whether cracks will appear after sintering. This chapter investigates the effects of spraying parameters on the quality of the dried coating layers.

6.1 Parameters Involved in the WPS Technique

Before optimizing the spray parameters, it's essential to first identify which parameters need to be considered. Figure 6.1 illustrates the movement trajectory of the nozzle during the WPS spraying process. The parameters involved in this process include temperature, humidity, atomizing air pressure, liquid loading rate, nozzle moving speed, nozzle size, solid concentration in the suspension, particle size distribution of the powder used, and nozzle-sample distance. Among these, temperature and humidity undoubtedly affect the evaporation rate of the coating layer. Unfortunately, these two factors are not fully controllable in the used lab and equipment and experiments can only be conducted under as consistent temperature and humidity conditions as possible. Based on extensive experimental experience, whether cracks appear in the dried layer does not seem to be particularly sensitive to temperature and humidity in the special case used here.

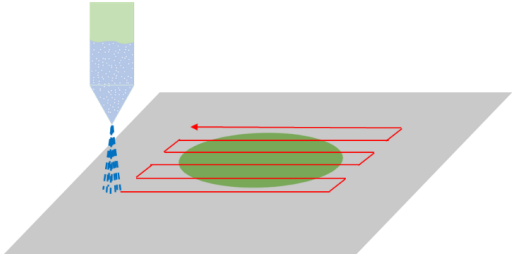

Figure 6.1. The movement trajectory of the nozzle during a single spraying pass in the WPS process.

Among the remaining parameters, it’s impractical to consider all of them simultaneously, as too many variables would increase the complexity of the experiment. Many parameters can be initially set within reasonable ranges based on empirical knowledge. For example, the air pressure must not be too high. otherwise, the spraying velocity will become excessive, causing the spray to disperse outward upon reaching the substrate. Conversely, the liquid atomization will be poor if the pressure is too low, or the velocity will be insufficient.

As discussed in the previous section, the liquid loading rate should be kept as low as possible. This rate is controlled by adjusting the needle lift height inside the nozzle—the lower the height, the lower the liquid output. However, if the liquid loading rate is too low, the gap between the needle tip and the nozzle outlet becomes minimal, which may cause the outlet to clog with powder during spraying, making liquid discharge difficult. Therefore, the liquid loading rate must strike a balance: it should be as low as possible while ensuring that the nozzle does not clog and can spray liquid evenly throughout the process.

The nozzle moving speed also affects the amount of suspension deposited with each spraying pass. A higher speed results in less liquid being deposited. This speed is also set within a reasonable range based on experience. Table 6.1 shows the preliminary fixed parameters used for the experiment.

Table 6.1. Fixed spraying parameters set in the WPS experiment.

Air pressure	Nozzle moving speed	Liquid loading rate	Nozzle size
0.16 bar	200 mm/s	0.033 ml/s	0.3 mm

Based on the fixed parameters mentioned above, a detailed study was conducted on the remaining parameters: solid concentration in the suspension, powder particle size distribution, and nozzle-sample distance.

6.2 Impact of Solid Concentration in the Suspension

For the remaining three parameters, the study first focused on solid concentration in the suspension. Self-prepared $BaZr_{0.16}Ce_{0.64}Y_{0.1}Yb_{0.1}O_{3-d}$ powder synthesized via the sol-gel method was used for this investigation. The nozzle height was fixed at 10 cm, and the solid concentration in the suspension was set at 0.5 wt%, 1 wt%, and 2 wt%, respectively. To ensure consistent coating thickness, the number of spraying passes was adjusted to 60, 40, and 20, respectively.

Figure 6.2 shows the SEM images of the coating surface after drying, as well as the electrolyte surface and cross section after sintering. It can be observed that when the concentration was 0.5 wt%, no cracks appeared in the dried coating layer or in the sintered electrolyte. At a concentration of 1 wt%, fine cracks began to form. These small cracks were not fully visible after sintering. However, the electrolyte surface was not entirely smooth, exhibiting small pits. When the solid concentration increased to 2 wt%, the drying cracks became more pronounced and larger. These larger cracks extended during sintering, leading to peeling off and curling of the electrolyte layer.

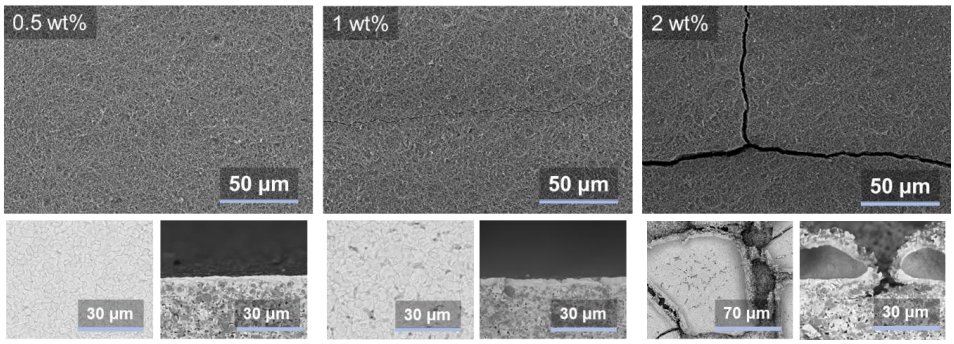

Figure 6.2. SEM images of the coating surface after drying, as well as the surface and cross section of the electrolyte after sintering, with solid concentrations in the suspension of 0.5 wt%, 1 wt%, and 2 wt%, respectively.

When a suspension containing ceramic powders is deposited onto a rigid substrate, solvent evaporation induces capillary forces due to the liquid's surface tension [236]. These forces tend to pull the particles together, causing shrinkage of the film. However, the rigid substrate constrains this shrinkage, resulting in the buildup of tensile stress within the film. Once the stress exceeds a critical value, the film cracks during drying. The magnitude of this stress increases with film thickness, and the maximum film thickness below which no cracking occurs is defined as the critical cracking thickness [237,238]. Therefore, during one spraying pass, a higher solid concentration in the suspension leads to a thicker dried layer, increased thickness in turn increases the likelihood of cracking. This explains why drying cracks become more pronounced and severe at higher solid concentrations.

Thus, increasing solid concentration poses the risk of forming drying cracks. However, if the solid loading is too low, achieving the desired coating thickness requires an excessive number of spraying passes, which increases the processing time and spraying cost. Therefore, further exploration of other parameters is needed to achieve higher solid concentration while avoiding crack formation.

6.3 Impact of Powder Particle Size Distribution

To ensure that the deposited layer remains crack-free while maintaining a solid concentration of at least 2 wt% in the suspension, the particle size distribution of the powders was then considered. As shown in Figure 6.3a, the self-made $BaZr_{0.16}Ce_{0.64}Y_{0.1}Yb_{0.1}O_{3-d}$ powder A exhibits a bimodal particle size distribution. Meanwhile, four other powder sets were also evaluated. Figures 6.3b and 6.3c depict the particle size distributions of Powder B (commercial $BaZr_{0.7}Ce_{0.2}Y_{0.1}O_{3-d}$) and Powder C (commercial $BaZr_{0.16}Ce_{0.64}Y_{0.1}Yb_{0.1}O_{3-d}$), respectively. Figure 3d shows the distribution of Powder D, which is a 1:1 mixture of Powders A and B, while Figure 3e represents Powder E, a 1:1 mixture of Powders A and C.

It is evident that the latter four powders all exhibit nearly monomodal and continuous particle size distributions.

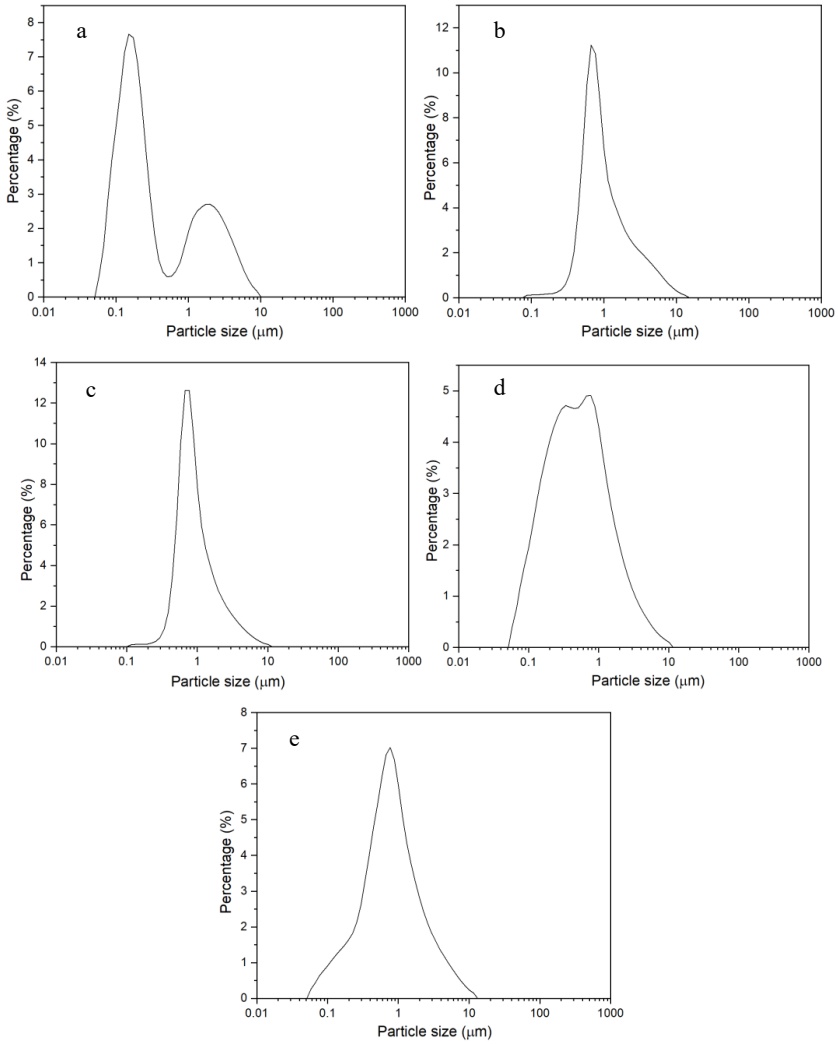

Figure 6.3. Particle size distribution of (a) powder A: self-made $BaZr_{0.16}Ce_{0.64}Y_{0.1}Yb_{0.1}O_{3-d}$, (b) powder B: commercial powder $BaZr_{0.7}Ce_{0.2}Y_{0.1}O_{3-d}$, (c) Powder C: commercial powder $BaZr_{0.16}Ce_{0.64}Y_{0.1}Yb_{0.1}O_{3-d}$, (d) powder D: 1:1 mixture of powder A and B, (e) powder E: 1:1 mixture of powder A and C.

Subsequently, coatings were sprayed using the suspension made of these five powders, maintaining a solid concentration of 2 wt% and a nozzle height of 10 cm. Figure 6.4 presents SEM images of the dried coating surfaces. It is clearly evident from Figures 6.4b–d that when the particle size distribution is continuous, the coating surface remains free of drying cracks. This highlights a strong correlation between the particle size distribution of the powder and the occurrence of cracks in the coating. During

the drying process, differences in drying rates between larger and smaller particles can result in variations in internal drying stress. When the particle size distribution is uneven, localized drying stress concentrations can occur, leading to the formation of drying cracks. If the particle size distribution is more uniform, the stress distribution will also become more even, thereby preventing the formation of drying cracks. Zhou et al. [231] observed the same phenomenon that no cracks were found after drying the suspension with a monomodal PSD, whereas the bimodal PSD led to cracking after drying.

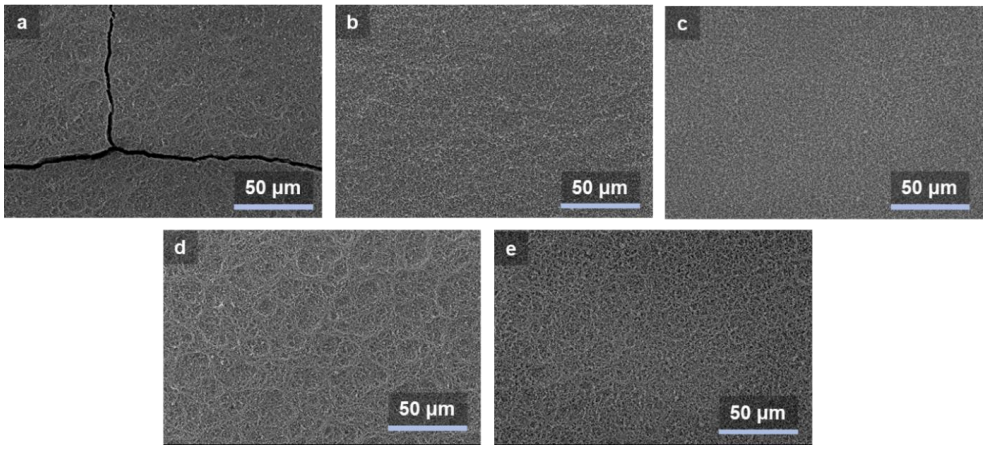

Figure 6.4. SEM images of the dried coating surfaces sprayed using powders with different particle size distributions. (a) powder A: self-made $BaZr_{0.16}Ce_{0.64}Y_{0.1}Yb_{0.1}O_{3-d}$, (b) powder B: commercial powder $BaZr_{0.7}Ce_{0.2}Y_{0.1}O_{3-d}$, (c) powder C: commercial powder $BaZr_{0.16}Ce_{0.64}Y_{0.1}Yb_{0.1}O_{3-d}$, (d) powder D: 1:1 mixture of powder A and B, (e) powder E: 1:1 mixture of powder A and C.

6.4 Impact of the Nozzle-Sample Distance

Further investigations were carried out related to the nozzle-sample distance. In this experiment, powder D from the previous section was used, with a solid concentration of 2 wt% in the suspension. The coating quality was studied at nozzle distances of 10 cm and 12 cm. It can be observed from Figure 6.5 that when the height was increased to 12 cm, drying cracks appeared on the coating surface. This phenomenon is closely related to the drying state of the spray when it reaches the substrate. A larger nozzle distance prolongs the flight time of the droplets, leading to more solvent evaporation in the air before deposition. As a result, the droplets arrive at the substrate in a more solidified or partially dried state, which hinders the proper rearrangement of powder particles and promotes the formation of internal stresses during film drying.

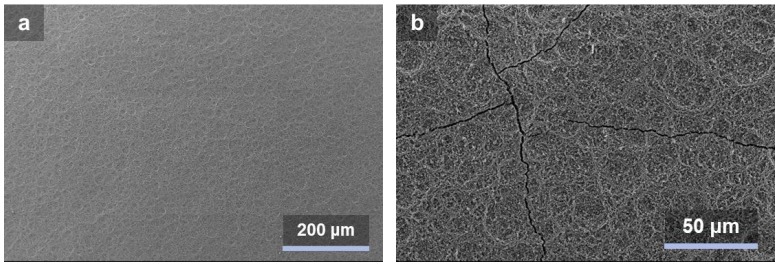

Figure 6.5. SEM images of the coating surfaces sprayed with different nozzle heights. (a) 10 cm, (b) 12 cm. 2 wt% of powder D in ethanol was used as the spraying suspension.

6.5 Summary

This chapter explores the development and optimization of a simplified, binder-free wet powder spraying (WPS) process for depositing thin, uniform, and crack-free BZCYYb electrolyte layers. Unlike conventional deposition methods such as tape casting and screen printing, the WPS method presented here employs only ethanol and ceramic powder, eliminating the need for organic additives such as dispersants and binders. This not only reduces fabrication complexity and cost, but also minimizes the residual porosity caused by binder burnout during sintering.

A key innovation in this WPS approach is the use of a low solid content suspension combined with a reduced liquid loading rate, enabling thin individual wet layers that dry completely between each spraying pass. This significantly alleviates drying-induced tensile stress and mitigates the risk of crack formation. A comprehensive investigation was conducted into the effects of three critical spraying parameters, solid concentration, particle size distribution, and nozzle-sample distance, on the quality of both dried coatings and sintered electrolyte layers.

The study found that high solid concentrations (e.g., 2 wt%) tend to increase the thickness of each sprayed layer, raising internal capillary stresses during drying and leading to cracks. However, by optimizing the particle size distribution, especially shifting from bimodal to monomodal or continuous distributions, the drying stress can be evenly distributed across the coating, effectively preventing crack formation even at higher solid loadings. This finding underscores the crucial role of powder characteristics in the mechanical stability of thin films during drying.

Additionally, the nozzle-sample distance was shown to impact the evaporation dynamics and droplet solidification during flight. Increasing the distance beyond 10 cm caused premature drying of droplets before they reached the substrate, thereby restricting particle rearrangement and leading to crack

formation upon drying. A nozzle height of 10 cm was identified as optimal for maintaining coating integrity.

Together, these results demonstrate that a carefully tuned WPS process can successfully produce dense, defect-free electrolyte layers suitable for solid oxide cell applications. The findings offer valuable guidelines for scaling the WPS technique toward industrial-level fabrication while maintaining film quality and consistency.

7 Co-Sintering of Thin Electrolyte with Different Fuel Electrodes

Sintering of Ba-based proton conductors has long been recognized as a major technical barrier to the development of PCCs, due to their high refractory nature and the issue of barium evaporation [100,239–251]. When thin Ba-based electrolyte layers are co-sintered with fuel electrodes, the process becomes even more complex. Additional factors come into play, including cations exchange between the electrolyte and the fuel electrode, as well as the influence of substrate shrinkage on the sintering process. The main objective of this chapter is to gain deeper insight into the sintering behavior of half-cells, aiming to achieve a dense electrolyte layer suitable for full-cell characterization.

This chapter is divided into two main sections. The first part investigates the sintering behavior of BZCYYb electrolytes on various Ba-based fuel electrodes, highlighting the impact of substrate shrinkage on Ba evaporation and its subsequent effect on electrolyte densification. The second section focuses on the sintering of BZCYYb electrolyte on SZCY/NiO substrates, with particular emphasis on Sr diffusion and its role in compensating Ba loss and influencing the sintering behavior of BZCYYb.

7.1 Ba-based Fuel Electrodes

7.1.1 Ba Evaporation Issue

To understand Ba evaporation during the sintering process, the sintering behavior of $BaZr_{0.16}Ce_{0.64}Y_{0.1}Yb_{0.1}O_3$ (BZCYYb) bulk samples was studied. 0.5 wt.% NiO was added to the BZCYYb as a sintering aid, and the samples were sintered at 1450 °C for 5 hours.

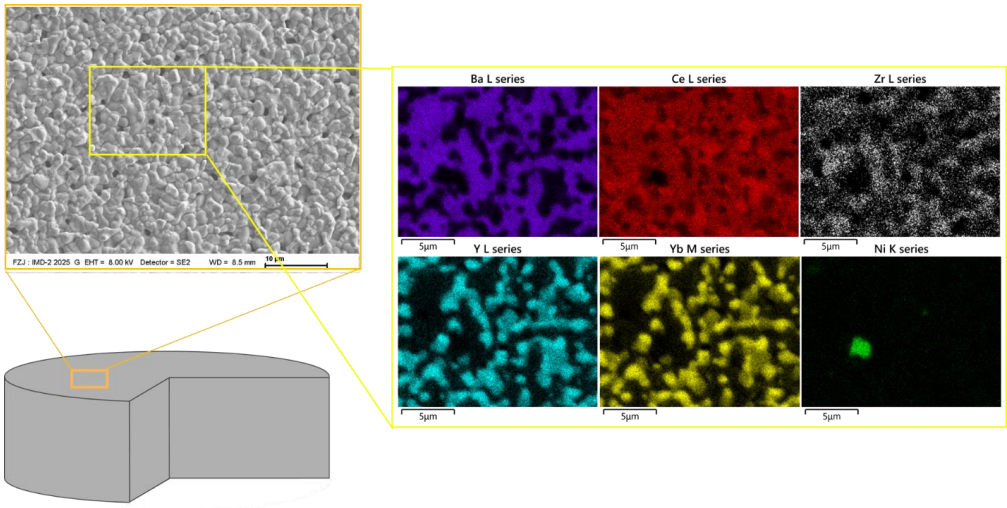

Figure 7.1. Surface SEM image and EDS mapping of the sintered BZCYYb pellet.

The surface microstructure of the bulk sample was first examined, as shown in Figure 7.1. The surface morphology of the BZCYYb pellet was found to be porous. EDS mapping revealed that the surface was filled with Y-Yb-rich secondary phases. This is a direct result of Ba evaporation during the sintering process. Consequences of Ba loss include the formation of secondary phases, failure to achieve densification of the electrolyte, and restricted grain growth.

Furthermore, the cross section of the sintered BZCYYb sample was studied to investigate the distribution of Ba evaporation from the surface to the interior of the bulk sample. As shown in Figure 7.2, a large amount of Y-Yb-rich secondary phases can be observed on the surface and near-surface region of the sample. Additionally, it is clearly seen that the grain size of BZCYYb in the near-surface layer is significantly smaller than that in the interior of the sample. This further highlights the inhibitory effect of secondary phases on grain growth. Based on this observation, it can be roughly estimated that the thickness of the surface layer affected by Ba evaporation is at least around 10 µm.

These results emphasize the negative impact of Ba evaporation on the sintering of BZCYYb. When testing and characterizing pellet samples, both sides of the sample will be polished before any measurements such as EIS. Therefore, Ba evaporation does not have a significant effect on the intrinsic study of the pellet samples. However, in the case of full cells that are supported by fuel electrodes, the electrolyte layer is only about 10 µm thick or even thinner. But just as shown in Figure 7.2, the near-surface region (approximately 10 µm), which is exposed to air, is strongly affected by Ba evaporation. Thus, Ba loss presents a major challenge in achieving densification of the electrolyte layer during the co-sintering of BZCYYb with the fuel electrode support.

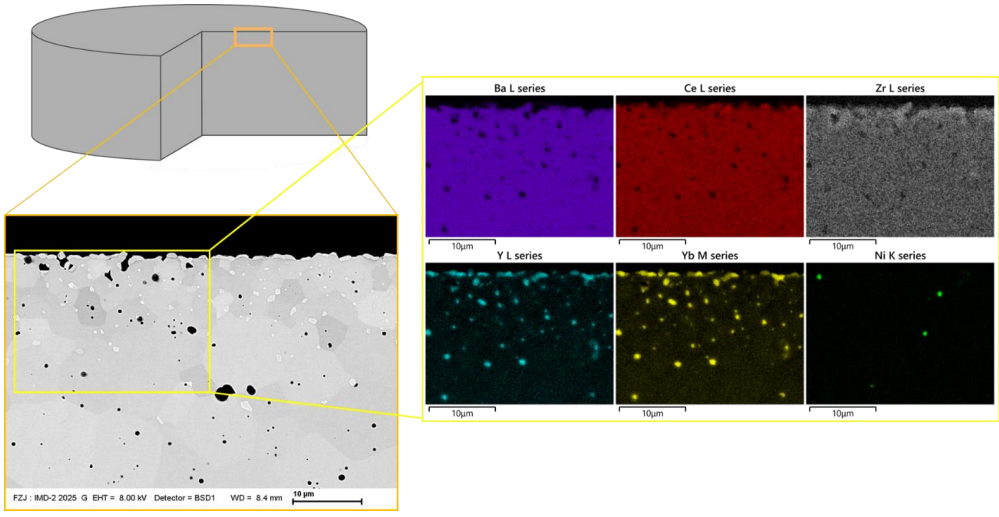

Figure 7.2. SEM images and EDS mapping of the cross section of the sintered BZCYYb pellet.

Two different substrates, BZCYYb/NiO and $BaZr_{0.65}Ce_{0.2}Y_{0.15}O_{3-\delta}$(BZCY-Y15)/NiO (the former has a high Ce content, while the latter has a high Zr content), are selected to investigate their effects on the sintering of BZCYYb electrolyte. The sintering temperature and conditions were the same as those used for the bulk sample in the previous section, i.e., 1450 °C for 5 hours, 2K/min as ramping rate. Figure 7.3 shows the microstructure of the electrolyte after sintering. It can be observed that the surface of the electrolyte is very similar to that of the bulk sample shown in Figure 7.1. The electrolyte is highly porous, and the grains have not grown sufficiently. This indicates that the sintering behavior of the electrolyte on the BZCY-Y15/NiO substrate is similar to the near-surface layer of the bulk sample, both being affected by Ba evaporation. As a result, Y-Yb-rich secondary phases form, grain growth is suppressed, and the electrolyte fails to densify. In contrast, the same electrolyte composition exhibits completely different sintering behavior on the BZCYYb/NiO substrate. As shown in Figure 7.4, the electrolyte layer achieves full densification, with no apparent formation of Y-Yb-rich secondary phases. The cross-sectional image also confirms that the electrolyte layer is dense.

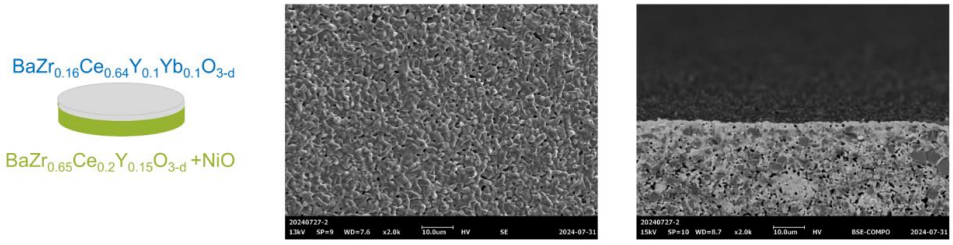

Figure 7.3. Co-sintering of BZCYYb and BZCY-Y15/NiO. SEM image of the surface (left) and cross section (right) of the half-cell sintered at 1450 °C for 5h.

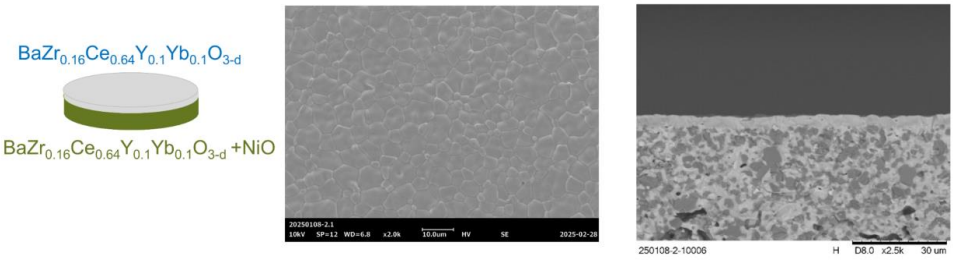

Figure 7.4. Co-sintering of BZCYYb and BZCYb-Y15/NiO. SEM image of the surface (left) and cross section (right) of the half-cell sintered at 1450 °C for 5h.

The role of substrate shrinkage in assisting electrolyte sintering must be considered first to understand the difference. Due to its higher Zr content, BZCY-Y15/NiO exhibits lower shrinkage compared to BZCYYb/NiO. As a result, the electrolyte layer experiences less shrinkage-induced stress that could aid sintering. However, the shrinkage should not be the reason to have different Ba evaporation and formation of secondary phases since both of them were sintered at the same temperature.

To demonstrate that substrate shrinkage is not the key factor influencing densification and Ba evaporation behavior, an additional experiment was conducted. The co-sintering temperature of BZCYYb with the BZCY-Y15/NiO substrate was increased to 1475 °C. At this higher sintering temperature, the shrinkage of the substrate should be larger and should better assist electrolyte densification, and also the electrolyte itself undergoes more intense sintering with higher temperature. Therefore, the electrolyte layer would be expected to be dense.

However, as shown in Figure 7.5, increasing the sintering temperature did not lead to improved densification of the electrolyte layer. On the contrary, severe Ba evaporation caused abnormal grain shapes, and a large amount of Y/Yb-rich secondary phases were observed on the surface. Thus, although substrate shrinkage can promote electrolyte sintering to some extent, it cannot explain the distinct differences in Ba evaporation and sintering behavior observed between the BZCY-Y15/NiO and BZCYYb/NiO substrates.

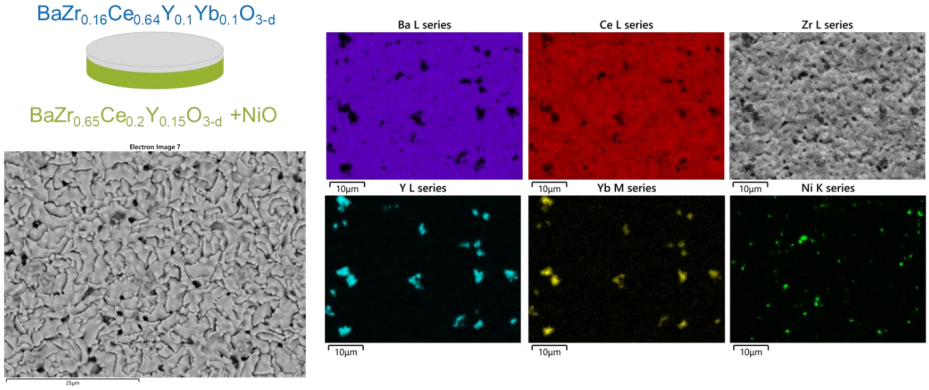

Figure 7.5. SEM image and EDS mapping of the electrolyte surface of the BZCYYb+BZCY-Y15/NiO half-cell sintered at 1475 °C for 5h.

7.1.2 Correlation Between Substrate Shrinkage and Ba Evaporation

In the research by Choi [252] et al., microstructures similar to those shown in Figure 7.3 were observed. Their study supports that under conditions of Ba evaporation, the formation of secondary phases is observed, and electrolyte densification was affected. Therefore, the next step is to investigate how different substrates affect Ba evaporation in the electrolyte.

From the shrinkage curves, it can be seen that BZCYYb/NiO exhibits higher shrinkage than BZCY-Y15/NiO across the entire temperature range. According to literature [252–256], Ba evaporation begins at approximately 1400 °C. By examining the shrinkage rates at 1400 °C in Figure 7.6, it is evident that BZCY-Y15/NiO undergoes significantly less shrinkage compared to BZCYYb/NiO. Therefore, at

1400 °C, the electrolyte layer co-sintered with the BZCY-Y15/NiO substrate experiences much less sintering-induced compressive stress than that co-sintered with BZCYYb/NiO. In other words, when Ba evaporation starts at 1400 °C, the electrolyte sintered on BZCYYb/NiO should be relatively denser than that sintered on BZCY-Y15/NiO.

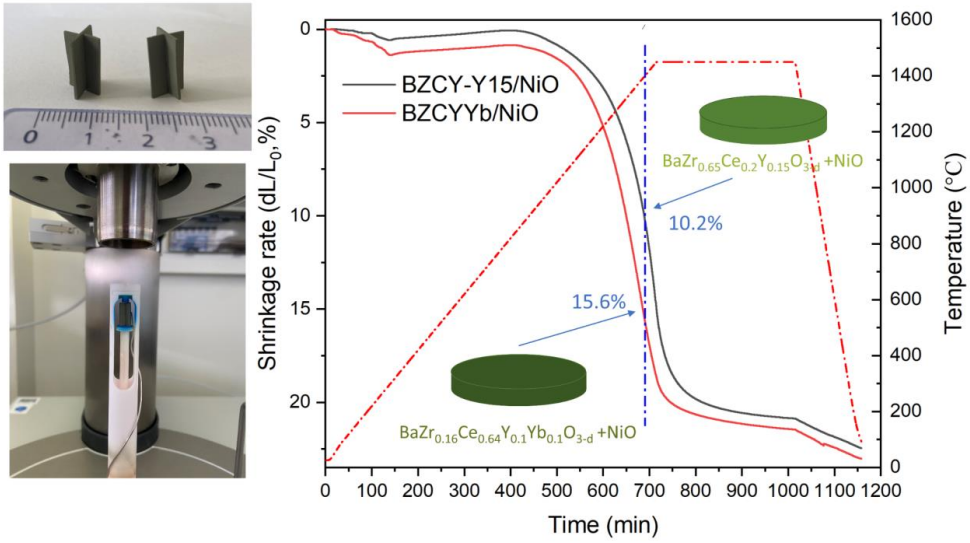

Figure 7.6. Shrinkage curve of the BZCY-Y15/NiO and BZCYYb/NiO substrate measured by the dilatometer with cross-shaped free-standing green tape.

To verify this hypothesis, another experiment was conducted. BZCYYb was co-sintered with the two different substrates at 1400 °C, with a dwelling time of only 1 minute. The surface morphology of the electrolyte after sintering under these conditions was then examined. As shown in Figure 7.7, the electrolyte sintered on the BZCYY-15/NiO substrate at 1400 °C exhibited more porosity. Image analysis using ImageJ/Fiji revealed an open porosity of 11% on the surface. In contrast, the electrolyte sintered on the BZCYYb/NiO substrate showed an open porosity of only 3%.

As previously mentioned, Ba evaporation begins at around 1400 °C. Due to the higher number of open pores in the electrolyte on the BZCY-Y15/NiO substrate, the contact area between the electrolyte and air is significantly larger, which promotes more extensive Ba evaporation. On the other hand, the electrolyte sintered on the BZCYYb/NiO substrate is already close to being dense at 1400 °C, with only a small number of open pores remaining, thus resulting in less Ba loss.

Higher Ba evaporation leads to the formation of more secondary phases in the electrolyte sintered on BZCY-Y15/NiO, which in turn hinders grain growth. In contrast, the lower level of Ba evaporation in

the electrolyte on BZCYYb/NiO prevents the formation of large amounts of secondary phases, allowing grain growth and densification to proceed more smoothly.

Intuitively, substrate shrinkage can promote electrolyte densification — the greater the substrate shrinkage, the more it assists the densification of the electrolyte. This study does not deny that principle rather, this study provides a deeper understanding of how substrate shrinkage affects Ba evaporation, which in turn influences the overall sintering process.

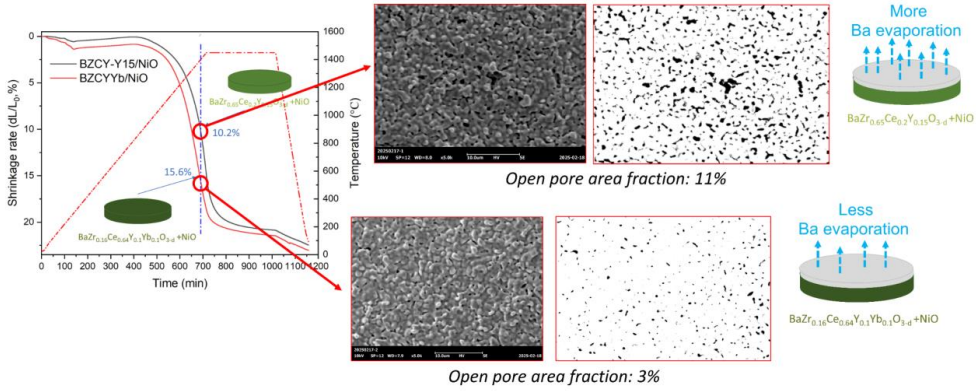

Figure 7.7. SEM images of the surface of the electrolyte co-sintered with BZCYY-15/NiO substrate (top) and BZCYYb/NiO (bottom) substrate at 1400 °C for 1 min. On the right side is the pore fraction analysis via ImageJ/Fuji software.

7.1.3 Electrochemical Performance of Full Cells

The BZCYYb electrolyte co-sintered on BZCYYb/NiO substrate, despite its ultrathin thickness, is susceptible to Ba evaporation during the sintering process. However, with the assistance of shrinkage from the underlying substrate, a highly dense electrolyte layer free from significant secondary phases was achieved, as observed in Figure 7.4. Therefore, this cell was selected for further performance evaluation under both PCFC and PCEC modes.

For the electrochemical testing, a $Ba_{0.5}La_{0.5}CoO_{3-\delta}$ BLC air electrode was used. Figure 7.8a shows an SEM image of the polished cross section of the single cell after testing. The electrolyte layer remained structurally intact, indicating good stability under operational conditions. From the cross-section, it appears that the porosity of the fuel electrode is still insufficient. While gas diffusion may not yet pose a significant limitation for button operation, further improvement of the fuel electrode's porosity will likely be necessary for future scale-up applications. Additionally, the BLC air electrode also exhibits relatively low porosity, which is another aspect that requires optimization in subsequent work.

Despite the suboptimal porosity of the electrodes, the ultrathin and dense electrolyte enabled excellent electrochemical performance, as shown in Figure 7.8. In PCFC mode, the open-circuit voltage (OCV) reached 1.06 V at 600 °C, which is comparable to OCV values typically reported for PCC [257–262]. This result demonstrates that the ultrathin electrolyte is able to maintain excellent gas-tightness due to its high densification.

Under SOFC operation, the cell achieved a remarkable power density of over 1000 mW cm^{-2} at 600 °C and 0.7 V. Even at a lower temperature of 500 °C, the power density remained as high as 473 mW cm^{-2}, reflecting efficient proton transport and low ohmic resistance of the thin electrolyte. As shown in Figure 7.8c, the PCEC performance was also outstanding. At 600 °C and an applied voltage of 1.3 V, the current density reached 2911 mA cm^{-2}, indicating highly effective electrochemical water splitting.

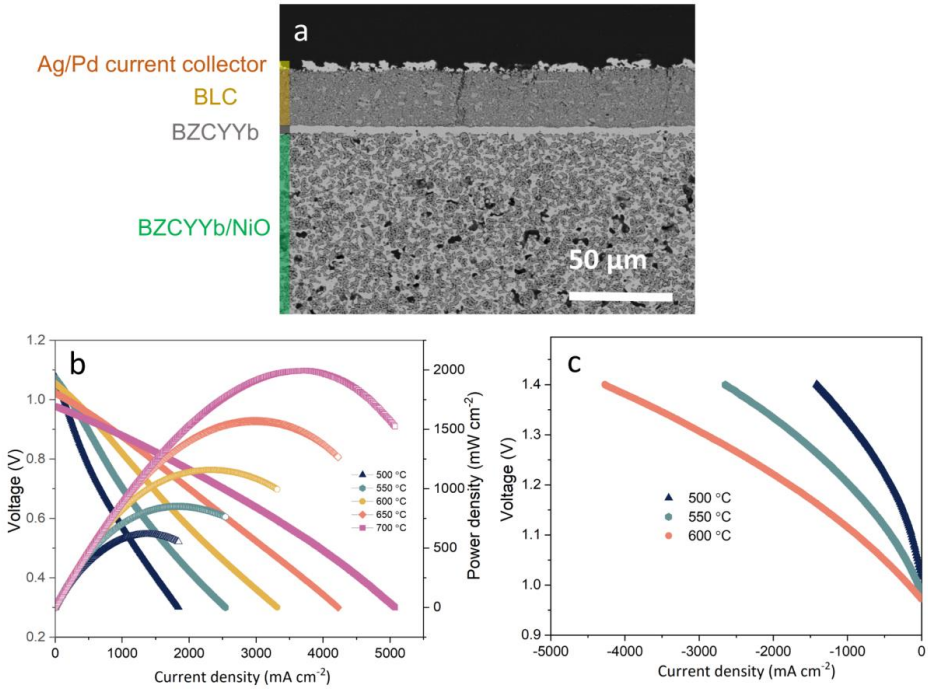

Figure 7.8. (a) SEM image of the polished cross section of the tested single cell. (b) I-V curve and power density in PCFC mode. (c) I-V curve in PCEC mode.

These results highlight the significant advantage of employing ultrathin, dense electrolytes in PCCs. With further optimization of electrode porosity and microstructure, this approach holds great promise for high-performance, low-temperature solid oxide cell applications in both fuel cell and electrolysis modes.

The excellent performance of the cell under both PCFC and PCEC modes is further evidenced by the EIS results. As shown in Figure 7.9, the total resistance is impressively low at 600 °C, with an ohmic resistance of only 0.11 Ω·cm² and a polarization resistance of merely 0.07 Ω·cm². The low ohmic resistance reflects not only the high ionic conductivity of the dense, ultrathin BZCYYb electrolyte but also the minimized interfacial resistance between the electrolyte and electrodes. The polarization resistance, which is closely related to the electrode reaction kinetics and gas transport phenomena, remains particularly low, suggesting highly active electrode surfaces and adequate gas access to reaction sites, despite the aforementioned limitations in electrode porosity.

The Arrhenius plot shown in Figure 7.10 reveals the temperature dependence of the resistive components and further clarifies the cell's transport and reaction characteristics. The activation energy for ohmic resistance is relatively low, indicative of the dominant role of proton conduction in the electrolyte. This is consistent with the protonic nature of BZCYYb, which benefits from its high proton mobility especially in humidified atmospheres. The linearity of the Arrhenius relationship confirms that the bulk conduction mechanism remains stable across the examined temperature range, without abrupt transitions or degradation-induced deviations.

At reduced temperatures, such as 500 °C, the polarization resistance becomes the dominant contributor to the total cell resistance. This behavior reflects a slowdown in the surface exchange and charge transfer reactions at the electrode interfaces. In particular, at lower temperatures, the reaction at the BLC air electrode becomes increasingly sluggish, and the limited porosity may restrict sufficient gas-phase reactant transport to active triple-phase boundaries. Additionally, the reactions on the fuel side also become kinetically hindered at these lower temperatures. The increased polarization resistance at 500 °C suggests that further improvements in electrode microstructure, especially higher porosity and optimized particle connectivity, would be necessary to sustain high performance under such conditions.

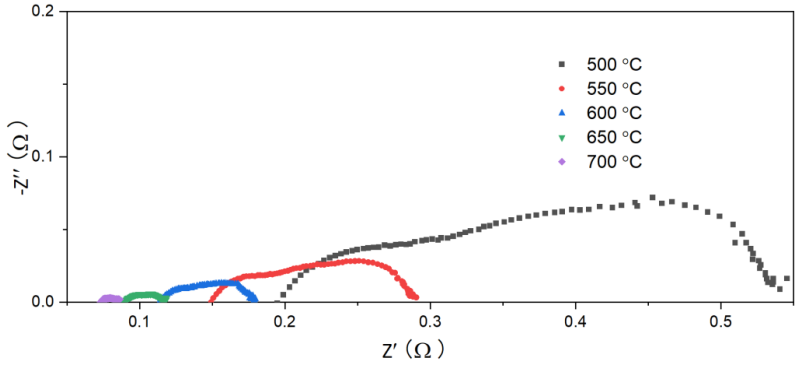

Figure 7.9. Nyquist plots of the full cell in OCV condition under different temperature.

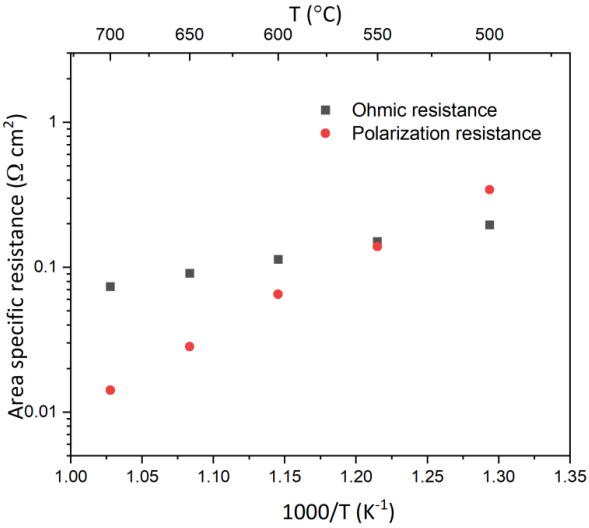

Figure 7.10. Area specific resistance of ohmic resistance and polarization resistance.

7.2 Sr-Based Fuel Electrode

7.2.1 Compensation of Ba Loss by Sr Diffusion

Figure 7.11a shows the SEM image of the surface morphology of a sintered BZCYYb electrolyte layer, which was deposited via WPS on a SZCY-based fuel electrode. The BZCYYb layer appears highly dense and shows large grain sizes. The average grain size was determined to be approximately 7.6 µm using the line intersection method on ten SEM images. The sintering temperature of similar compositions in the literature is generally above 1400 °C, typically around 1450 °C. This suggests that the SZCY fuel electrode significantly promotes the sintering and grain growth of the BZCYYb electrolyte. This promotion effect can be attributed to three main factors: (1) the larger shrinkage of the SZCY/NiO substrate during sintering due to its lower sintering temperature [263], which facilitates densification of the BZCYYb layer; (2) Sr diffusion between the fuel electrode and the electrolyte layer during the sintering process, making the final composition of the electrolyte no longer pure BZCYYb but rather Sr-doped BZCYYb. This modified composition inherently has a lower sintering temperature. Studies by Lee et al. [264] and Sailaja et al. [265] have demonstrated that Sr doping in BZCY facilitates the grain growth; and (3) the compensation of Ba evaporation by Sr diffusion from the substrate, which suppresses the formation of Y-rich secondary phases and promotes larger grain growth.

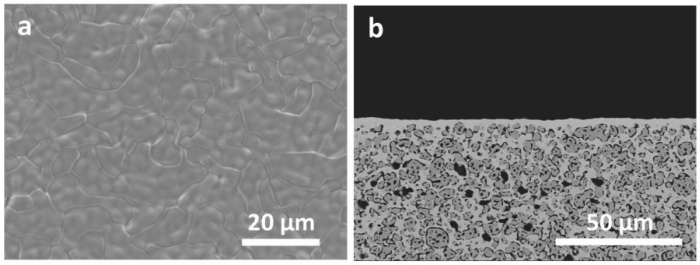

Figure 7.11. (a) SEM image of the surface of the BZCYYb electrolyte layer sintered at 1375 °C. (b) SEM image of the polished cross-section of the reduced half-cell that was sintered at 1375 °C.

Since both SZCY and BZCYYb have ABO_3-type perovskite crystal structure, the A-site element interdiffusion between Sr and Ba is inevitable [263]. This interdiffusion plays a crucial role in achieving the densification of the electrolyte layer. Sr and Ba diffusion will be further discussed through STEM characterization. The grain morphology shown in Figure 7.11a is distinct from that typically observed in sintered BZCYYb electrolyte materials [155,158,252,258,263]. To further validate the role of Sr diffusion in promoting sintering, we conducted additional experiments at a lower sintering temperature of 1350 °C, as shown in Figure 7.12. The results revealed that the grains sintered at 1350 °C were much smaller, and the electrolyte is not completely dense. Some particles have typical smaller size. The EDS mapping first confirms the Sr diffuses from the fuel electrode to almost all the electrolyte layer. And the

smaller particles, further confirmed by EDS point analysis on position 2 (the secondary phase), can be identified as Y-, Yb- and Ni-rich secondary phases together with high Sr content and the other elements. The cell sintered at 1350 °C indicating incomplete densification and compositional inhomogeneity. Therefore, the following inference can be made regarding the sintering of the BZCYYb electrolyte on SZCY. During the sintering process, the evaporation of the A-site element Ba causes the precipitation of the B-site elements Y and Yb. The Sr from the fuel electrode diffuses into the electrolyte layer, compensating for this missing of Ba. However, the diffusion rate of cations is relatively slow at 1350 °C, preventing the electrolyte layer from achieving complete homogenization.

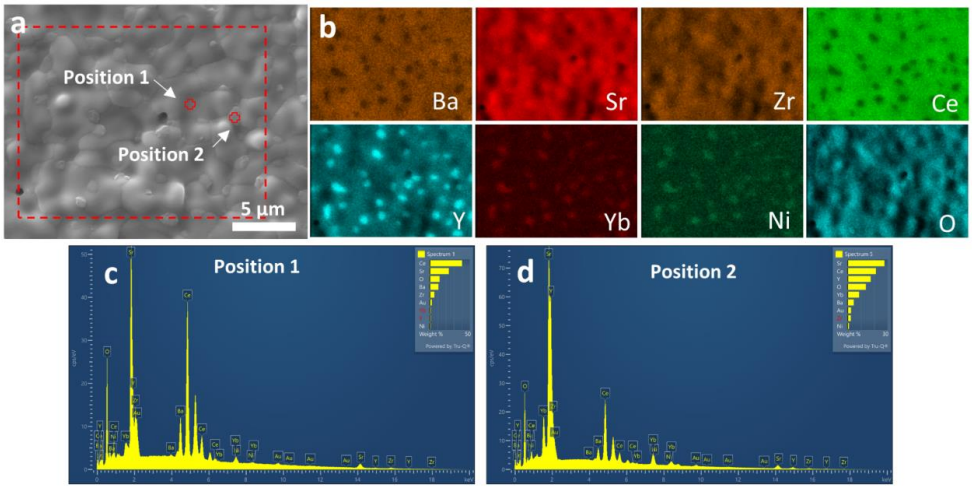

Figure 7.12. (a) SEM image of the surface of the BZCYYb electrolyte layer sintered at 1350 °C. The EDS mapping area is marked with red dashed rectangular box, and two marked areas are for the point EDS analysis. (b) EDS mapping of the selected area. EDS analysis of the point at (c) position 1 and (d) position 2.

Furthermore, no apparent secondary phases were observed in the electrolyte layer sintered at 1375 °C. This confirms that the compensation for Ba evaporation due to Sr diffusion prevents the formation of Y-rich secondary phases in the electrolyte layer sintered at 1375 °C. According to different reports [176,252,266], it is clear that Ba under-stoichiometry caused by Ba evaporation can result in the formation of Y-rich phases, and typically leads to smaller grain sizes and poor sintering behavior. This phenomenon may be related to a retarding effect of Y-rich phase on grain growth in BZCYYb. With Sr compensation from the substrate, the formation of Y-rich phase is avoided, resulting in large grains after sintering.

Figure 7.11b shows the polished cross-sectional image of the half-cell after reduction. The entire electrolyte layer is thin and dense, with no evidence of delamination issues post-reduction. A well-connected percolation pathway between the electrolyte layer and the SZCY in the fuel electrode is

observed. The fuel electrode functional layer and support layer, which exhibits higher porosity, are distinguishable.

To better investigate the microstructure of the electrolyte layer, STEM characterization was conducted on the half-cell. Figure 7.13a displays the sampling position during the FIB preparation of the STEM lamella. Two grain boundaries were deliberately included within the lamella, and the sampling region contained a narrow-grain area. In the STEM bright-field image (Figure 7.13b), as indicated by the sampling position in Figure 7.13a, two distinct vertical grain boundaries are clearly visible. There is only one grain present along the proton transport direction. Although the middle grain appears narrow on the surface, no horizontal grain boundaries were observed in the cross-section that could impede proton conduction. The local positive core charge at grain boundaries in proton-conducting ceramics typically acts as a significant barrier to proton transport, leading to much lower grain boundary conductivity compared to the bulk one [267]. However, the structure shown in Figure 7.13b lacks these grain boundary barriers, which facilitates rapid proton transport through the electrolyte. At the sampling position, the electrolyte layer thickness is approximately 3 μm.

STEM-EDS elemental analysis was performed for the region in Figure 7.13b. Peak overlapping was prevalent in the EDS spectra due to the large number of elements, such as Yb and Ni. Consequently, the Yb elemental mapping was excluded due to its unreliability. At the selected region, the electrolyte layer was in contact with NiO and SZCY particles from the fuel electrode. It is evident that Ba in the BZCYYb layer had completely interdiffused with Sr in SZCY. Although the partial overlap of Sr and Ce peaks complicated quantification, the uniform signal intensity of Ba and Sr indicates extensive interdiffusion. Moreover, the initial compositions of SZCY and BZCYYb exhibit different Zr/Ce ratios. However, EDS mapping revealed no strong compositional differences in Zr and Ce between these two particles, further confirming substantial elemental exchange between the electrolyte and SZCY in the fuel electrode. This interdiffusion altered the stoichiometry of the electrolyte from its initial composition to a new modified composition with more Sr at A-site. With Sr inclusion, it is expected to exhibit a lower sintering temperature, which further explains the dense microstructure and large grain sizes achieved at 1375 °C. However, Sr-based proton-conducting ceramics typically demonstrate lower proton conductivity compared to their Ba-based counterparts due to a reduced hydration ability [268]. This trade-off represents a compromise strategy for achieving lower sintering temperatures.

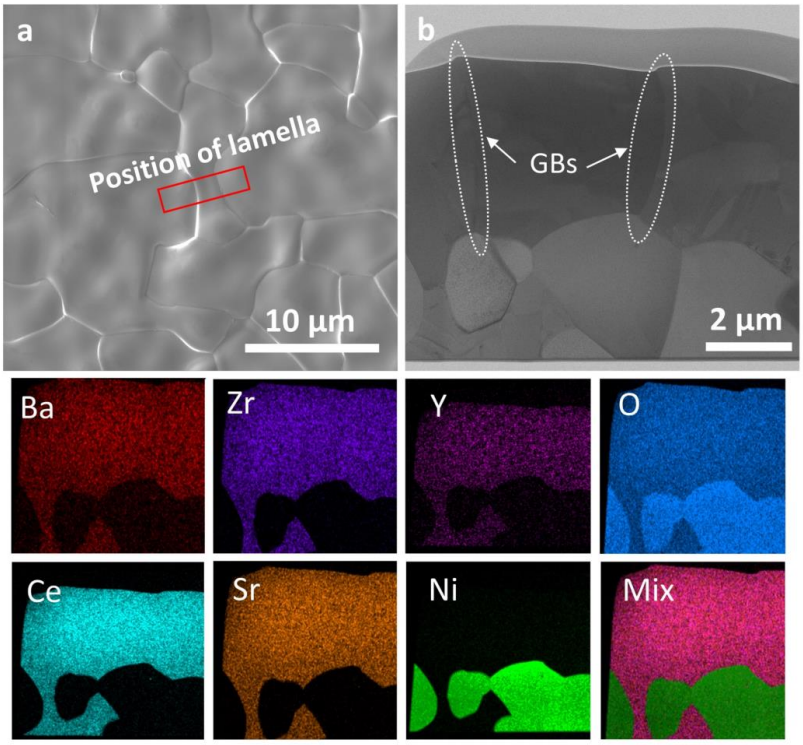

Figure 7.13. (a) SEM image of the surface of the electrolyte layer sintered at 1375 °C. The area marked by a red rectangle indicates the position where the lamella specimen was prepared by FIB. (b) STEM-bright field image of the electrolyte and fuel electrode (GBs indicate grain boundaries). (c) EDS mapping of the selected area, including Ba, Zr, Y, Ce, Sr, Ni, O.

7.2.2 Electrochemical Performance of Full cells

To perform electrochemical testing of the full cell, BLC was used as the air electrode. Figure 7.14a shows the cross-sectional fracture surface of the full cell. Figure 7.14b illustrates the voltage (V) and power density (P) as functions of current density (I) measured at different temperatures (500–700 °C) in fuel cell mode. At 600 °C, the power density achieves 422 mW/cm² at a voltage of 0.7 V. Figure 7.14c shows the EIS results of the full cell in a Nyquist plot. The ohmic resistance and polarization resistance at different temperatures can be obtained from the plots, which are further plotted as an Arrhenius plot in Figure 7.14d. At 700 °C, the ohmic resistance of the full cell is 0.19 Ω·cm². The activation energy of the ohmic resistance fitted within the temperature range of 500–700 °C is 0.32 eV, which is similar to the activation energy reported for BZCYYb compositions in the literature [158,264,269]. This relatively low activation energy suggests a favorable ion conduction pathway and indicates that the electrolyte material is well-suited for operation at intermediate temperatures.

At 700 °C, the polarization resistance is lower than the ohmic resistance. However, due to the higher activation energy, the polarization resistance dominates the total resistance when the temperature is below 650 °C. This phenomenon highlights the importance of optimizing both the electrolyte material and the electrode-electrolyte interface to reduce polarization resistance, which becomes a key limiting factor at lower temperatures. It can be observed that the activation energy of the polarization resistance varies in different temperature regions. By segmented fitting, the activation energy is found to be 1.34 eV in the range of 600–700 °C and 0.45 eV in the range of 500–600 °C. The polarization resistance obtained from the single cell includes contributions from both the anode and cathode. Nevertheless, the observed temperature-dependent transition in activation energy is likely related to the behavior of the BLC cathode. This variation, which has also been observed in materials with similar compositions [270,271], is attributed to the different dominant ion transport mechanisms in the BLC air electrode at different temperatures. Oxygen ion transport dominates at higher temperatures, while proton transport becomes dominant at relatively lower temperatures.

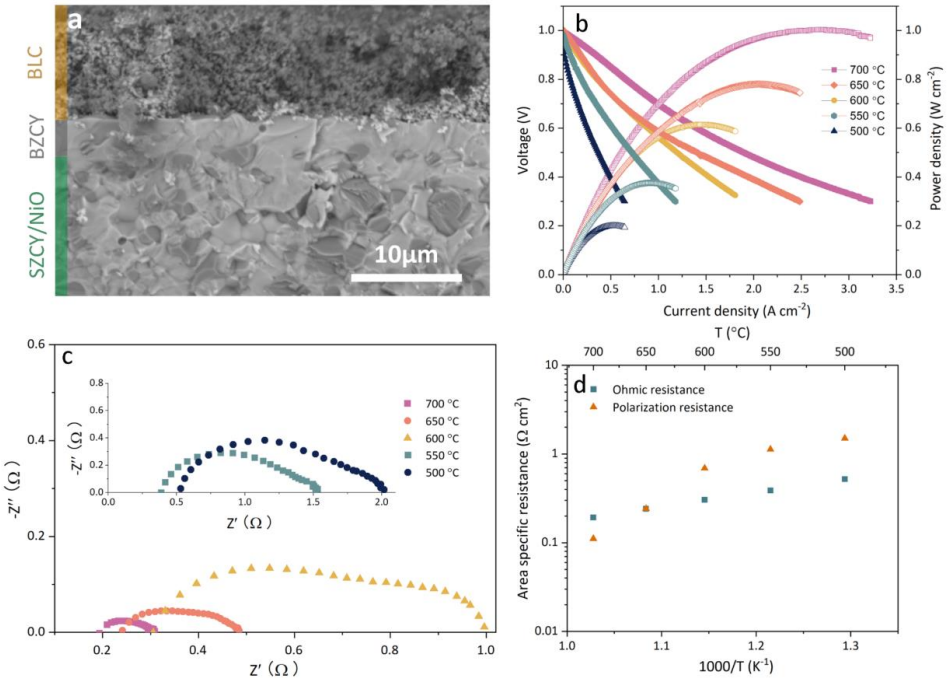

Figure 7.14. (a) SEM image of the fracture surface of the single cell sintered at 1375 °C. (b) The voltage and power density as a function of current density measured at temperature range 500 to 700 °C. (c) Nyquist plots of the full cell measured at temperature range 500 to 700 °C. (d) Arrhenius plots of the ohmic resistance and the polarization resistance.

The reduced ohmic resistance and boosted electrochemical performance brought by the thin electrolyte layer are evident, but some issues have also been exposed. Figure 7.15 shows the open-circuit voltage

(OCV) of the full cell at different temperatures. At 600 °C, the OCV is 1.01 V, slightly lower than the reported values in the literature (1.03, 1.04 V) [158,258]. However, when the temperature decreases to 500 °C, the OCV drops to 0.92 V. Although proton-conducting ceramics are known to exhibit slightly lower OCVs due to electronic leakage caused by electronic conductivity, the electronic conductivity of proton-conducting ceramics should also theoretically decrease as the temperature decreases, leading to a higher OCV. Therefore, the low OCV observed in the tested full cell should not be attributed to electronic leakage. Subsequently, the surface of the sintered electrolyte layer was extensively investigated again, and a few defects were identified that might lead to gas leakage. The insert in Figure 7.15 shows a specific defect that was discovered. Due to the thinness of the electrolyte layer, even minor defects can result in gas leakage. At high temperatures, rapid reactions may mitigate the impact of these small defects, but as the temperature decreases and gas reaction rates at the interface slow down, the leakage can cause more severe issues. This explains why the OCV decreases as the temperature is lowered.

Nevertheless, these defects are not caused by unreasonable WPS conditions. Before spraying, the substrate undergoes multiple pre-treatments, such as pre-calcination, which can lead to contamination by impurities like dust. Unlike other thin-film deposition methods, WPS involves layer-by-layer deposition of ceramic powder onto the substrate. Any dust or contamination present can be embedded during the spraying process, resulting in defects after sintering. The defect shown in the insert of Figure 7.15 strongly resembles one caused by a small contaminant covered by subsequent layers. These defects can be avoided through stricter quality control throughout the preparation process or coating in a dust-reduced or -free environment. Especially compared to the rudimentary conditions in the existing laboratory, a rigorous industrial production process can completely prevent such issues.

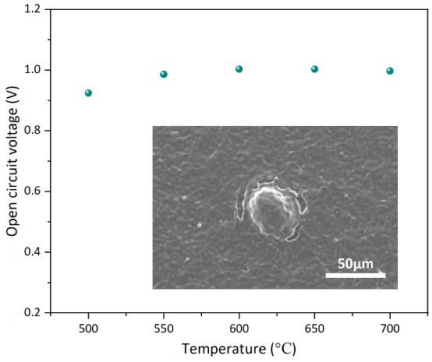

Figure 7.15. Open circuit voltage of the full cell at different measurement temperatures. Insert SEM image presenting one example of defect on the electrolyte surface that may lead to gas leakage.

7.3 Summary

This chapter systematically investigated the co-sintering behavior of ultrathin BZCYYb electrolyte layers with different fuel electrode substrates, focusing on the underlying mechanisms that affect densification, Ba evaporation, and electrochemical performance. For Ba-based fuel electrodes, it was confirmed that Ba evaporation during high-temperature sintering leads to the formation of Y/Yb-rich secondary phases, suppressed grain growth, and incomplete densification, especially when the substrate exhibits insufficient shrinkage. Among the tested substrates, BZCYYb/NiO demonstrated a favorable shrinkage profile that assisted the electrolyte in achieving high density and phase purity. Notably, denser microstructures formed before the onset of significant Ba loss were found to reduce the degree of evaporation, suggesting a strong correlation between substrate shrinkage, early densification, and Ba retention.

To further probe the relationship between substrate characteristics and electrolyte sintering, BZCYYb was also co-sintered with a Sr-based SZCY/NiO substrate. The results revealed that Sr diffusion from the substrate into the electrolyte played a critical role in compensating Ba loss, facilitating grain growth, and enabling densification at a significantly reduced sintering temperature (as low as 1375 °C). STEM-EDS characterization confirmed extensive interdiffusion at the interface, leading to modified electrolyte compositions with Sr partially occupying the A-site, which improved sinterability but potentially compromised proton conductivity due to reduced hydration capability.

Electrochemical performance tests of full cells based on both BZCYYb/NiO and SZCY/NiO fuel electrodes validated the structural observations. Cells with dense ultrathin electrolytes exhibited high power densities exceeding 1000 mW/cm² at 600 °C in PCFC mode and excellent current output under PCEC operation. Impedance measurements confirmed low ohmic and polarization resistances, while Arrhenius analysis highlighted the activation energies associated with different transport processes. Nevertheless, low OCV values at reduced temperatures were observed in Sr-based cells, primarily due to minor defects in the thin electrolyte layer introduced during the WPS process.

Overall, this chapter underscores the critical role of substrate selection and interfacial interactions in achieving dense, defect-free, and high-performance electrolyte layers through co-sintering, offering valuable insights for scaling up PCCs toward practical applications.

8 Conclusion and Outlook

This dissertation has systematically investigated the scientific and technological challenges associated with the practical implementation of proton-conducting ceramics in electrochemical energy devices. Through a combination of materials design, mechanical characterization, advanced processing, and cell-level integration, a scalable fabrication route has been established for producing ultrathin proton-conducting electrolyte layers, enabling the realization of high-performance fuel and electrolysis cells. Based on these advances, the following major conclusions have been drawn:

(1) Optimizing Y substitution in BZCY proton conductor

Increasing Y content improves hydration ability and thus proton conductivity due to higher oxygen vacancy concentration. However, excessive Y amount (>20 at.%) leads to nanoscale phase separation and secondary phase formation, as shown by SEM and XRD analysis. A composition with 20 at.% Y balances bulk and grain boundary conductivity while maintaining phase purity and sinterability. Y-induced space charge layer effects enhance grain boundary conductivity, highlighting the importance of defect chemistry control.

(2) Mechanical properties of Ba-based fuel electrode support

BZCY-Y15/NiO exhibits increased bending strength and elastic modulus with higher sintering temperature due to improved densification. However, post-reduction leads to strength degradation caused by internal pore formation during NiO reduction. Weibull analysis reveals increased Weibull modulus for the higher temperature sintered samples, resulting from inhomogeneous flaw distribution. Compared to conventional YSZ-based supports, BZCY/NiO remains mechanically weaker, necessitating improved processing control and support architecture engineering.

(3) WPS for thin electrolyte layer fabrication

The binder-free WPS process developed in this study allows for controllable deposition of ultrathin, crack-free electrolyte layers with high density after sintering. By using low solid content suspensions and optimizing spray parameters, drying stress is effectively minimized. This process eliminates organic additives, reduces cost, and offers high reproducibility. Such a simple yet effective approach has potential for industrial-scale production of proton conducting ceramic fuel and electrolysis cells.

(4) Half-cell co-sintering studies aiming for dense electrolyte

Successful co-sintering depends critically on substrate shrinkage behavior and interfacial cation dynamics. BZCYYb/NiO provided a compatible shrinkage match, enabling dense, high-quality thin electrolyte layers. Sr-doped substrates introduced beneficial Sr diffusion, which compensated for Ba loss and lowered the sintering temperature.

(5) Full Cell Performance Validation

Full cells fabricated using optimized electrolyte layers and co-sintering protocols demonstrated excellent electrochemical performance. Power densities exceeded 1000 mW/cm² at 600 °C and 0.7 V in fuel cell mode with low ohmic and polarization resistance, and current density reached 2911 mA/cm² at an applied voltage of 1.3 V in electrolysis mode.

The achievements presented in this dissertation establish a solid foundation for the advancement of proton-conducting ceramic cells (PCCs), from material development to device-level fabrication. Nevertheless, several crucial research directions remain to be addressed to further unlock the full potential of PCCs for practical and scalable energy applications.

(1) Advanced microstructural engineering

The control of porosity and microstructural uniformity in both the fuel and air electrodes remains an issue in present work. Insufficient porosity in these electrodes can hinder gas transport and limit overall cell performance. Moreover, defect control and homogenization within the BZCY phase in the BZCY/NiO fuel electrode are critical for improving the mechanical reliability of the fuel electrode. Future work should focus on eliminating local phase aggregation and tailoring the pore structure to enhance both mechanical strength and electrochemical performance.

(2) Faradaic efficiency

The deployment of ultrathin electrolyte layers, while beneficial for reducing ohmic losses, may compromise Faradaic efficiency due to increased electronic leakage. Proton-conducting electrolytes such as BZCYYb exhibit small but non-negligible electronic conductivity, which becomes more significant as the electrolyte thickness decreases. One major contributor to this issue is Ni diffusion from the fuel electrode into the thin electrolyte during high-temperature sintering, which degrades hydration capability and reduces proton concentration, meantime increasing the electronic conductivity. To address this, a promising strategy involves the deposition of a secondary, Ni-free BZCYYb layer on top of the sintered electrolyte using techniques such as physical vapor deposition or pulsed laser deposition. This additional layer, not subjected to high-temperature sintering, could retain high hydration capacity and serve as an effective electronic barrier, thereby enhancing Faradaic efficiency in both fuel cell and electrolysis modes.

(3) Scale-up and long-term operational stability

The fabrication processes developed in this work, including wet powder spraying (WPS), co-sintering strategies, and component integration, offer scalable solutions suitable for large-area PCCs manufacturing. However, scaling up introduces new challenges, such as mechanical deformation (e.g., warping) during co-sintering, which must be addressed through further optimization of substrate-

electrolyte compatibility, shrinkage matching, and sintering profiles. Additionally, although PCCs show promising initial performance, their long-term stability under continuous operation remains underexplored. To ensure commercial viability, future studies must focus on degradation mechanisms, such as electrode delamination, microstructural evolution, and performance loss over extended cycling. Systematic aging tests and operando characterization will be essential to establish reliable degradation models and lifetime prediction frameworks.

9 Appendix

9.1 References

[1] K. Hansen, B.V. Mathiesen, I.R. Skov, Full energy system transition towards 100% renewable energy in Germany in 2050, Renewable and Sustainable Energy Reviews 102 (2019) 1–13. https://doi.org/10.1016/j.rser.2018.11.038.

[2] D. Connolly, H. Lund, B.V. Mathiesen, Smart Energy Europe: The technical and economic impact of one potential 100% renewable energy scenario for the European Union, Renewable and Sustainable Energy Reviews 60 (2016) 1634–1653. https://doi.org/10.1016/j.rser.2016.02.025.

[3] B.V. Mathiesen, H. Lund, D. Connolly, H. Wenzel, P.A. Østergaard, B. Möller, S. Nielsen, I. Ridjan, P. Karnøe, K. Sperling, F.K. Hvelplund, Smart Energy Systems for coherent 100% renewable energy and transport solutions, Applied Energy 145 (2015) 139–154. https://doi.org/10.1016/j.apenergy.2015.01.075.

[4] M.B. Mogensen, M. Chen, H.L. Frandsen, C. Graves, J.B. Hansen, K.V. Hansen, A. Hauch, T. Jacobsen, S.H. Jensen, T.L. Skafte, X. Sun, Reversible solid-oxide cells for clean and sustainable energy, Clean Energy 3 (2019) 175–201. https://doi.org/10.1093/ce/zkz023.

[5] Y. Wang, Y. Ling, B. Wang, G. Zhai, G. Yang, Z. Shao, R. Xiao, T. Li, A review of progress in proton ceramic electrochemical cells: material and structural design, coupled with value-added chemical production, Energy Environ. Sci. 16 (2023) 5721–5770. https://doi.org/10.1039/D3EE03121G.

[6] S. Hossain, A.M. Abdalla, S.N.B. Jamain, J.H. Zaini, A.K. Azad, A review on proton conducting electrolytes for clean energy and intermediate temperature-solid oxide fuel cells, Renewable and Sustainable Energy Reviews 79 (2017) 750–764. https://doi.org/10.1016/j.rser.2017.05.147.

[7] E.D. Wachsman, K.T. Lee, Lowering the Temperature of Solid Oxide Fuel Cells, Science 334 (2011) 935–939. https://doi.org/10.1126/science.1204090.

[8] C. Duan, J. Huang, N. Sullivan, R. O'Hayre, Proton-conducting oxides for energy conversion and storage, Applied Physics Reviews 7 (2020) 011314. https://doi.org/10.1063/1.5135319.

[9] A. Hauch, R. Küngas, P. Blennow, A.B. Hansen, J.B. Hansen, B.V. Mathiesen, M.B. Mogensen, Recent advances in solid oxide cell technology for electrolysis, Science 370 (2020) eaba6118. https://doi.org/10.1126/science.aba6118.

[10] I.T. Bello, S. Zhai, S. Zhao, Z. Li, N. Yu, M. Ni, Scientometric review of proton-conducting solid oxide fuel cells, International Journal of Hydrogen Energy 46 (2021) 37406–37428. https://doi.org/10.1016/j.ijhydene.2021.09.061.

[11] M.K. Hossain, R. Chanda, A. El-Denglawey, T. Emrose, M.T. Rahman, M.C. Biswas, K. Hashizume, Recent progress in barium zirconate proton conductors for electrochemical hydrogen device applications: A review, Ceramics International 47 (2021) 23725–23748. https://doi.org/10.1016/j.ceramint.2021.05.167.

[12] J. Song, Y.Y. Birdja, D. Pant, Z. Chen, J. Vaes, Recent progress in the structure optimization and development of proton-conducting electrolyte materials for low-temperature solid oxide cells, Int J Miner Metall Mater 29 (2022) 848–869. https://doi.org/10.1007/s12613-022-2447-y.

[13] F. Liu, D. Ding, C. Duan, Protonic Ceramic Electrochemical Cells for Synthesizing Sustainable Chemicals and Fuels, Advanced Science 10 (2023) 2206478. https://doi.org/10.1002/advs.202206478.

[14] S. Pirou, Q. Wang, P. Khajavi, X. Georgolamprou, S. Ricote, M. Chen, R. Kiebach, Planar proton-conducting ceramic cells for hydrogen extraction: Mechanical properties, electrochemical performance and up-scaling, International Journal of Hydrogen Energy 47 (2022) 6745–6754. https://doi.org/10.1016/j.ijhydene.2021.12.041.
[15] U. Tariq, M.Z. Khan, O. Gohar, Z.U. Din Babar, F. Ali, R.A. Malik, I.A. Starostina, Samia, J. Rehman, I. Hussain, M. Saleem, A. Ghaffar, M.A. Marwat, K. Zheng, M. Motola, M.B. Hanif, Bridging the Gap between fundamentals and efficient devices: Advances in proton-conducting oxides for low-temperature solid oxide fuel cells, Journal of Power Sources 613 (2024) 234910. https://doi.org/10.1016/j.jpowsour.2024.234910.
[16] F.J.A. Loureiro, N. Nasani, G.S. Reddy, N.R. Munirathnam, D.P. Fagg, A review on sintering technology of proton conducting $BaCeO_3$-$BaZrO_3$ perovskite oxide materials for Protonic Ceramic Fuel Cells, Journal of Power Sources 438 (2019) 226991. https://doi.org/10.1016/j.jpowsour.2019.226991.
[17] H. Iwahara, H. Uchida, N. Maeda, High temperature fuel and steam electrolysis cells using proton conductive solid electrolytes, Journal of Power Sources 7 (1982) 293–301. https://doi.org/10.1016/0378-7753(82)80018-9.
[18] H. Iwahara, H. Uchida, S. Tanaka, High temperature type proton conductor based on $SrCeO_3$ and its application to solid electrolyte fuel cells, Solid State Ionics 9–10 (1983) 1021–1025. https://doi.org/10.1016/0167-2738(83)90125-X.
[19] H. Iwahara, T. Esaka, H. Uchida, N. Maeda, Proton conduction in sintered oxides and its application to steam electrolysis for hydrogen production, Solid State Ionics 3–4 (1981) 359–363. https://doi.org/10.1016/0167-2738(81)90113-2.
[20] K.D. Kreuer, Aspects of the formation and mobility of protonic charge carriers and the stability of perovskite-type oxides, Solid State Ionics 125 (1999) 285–302. https://doi.org/10.1016/S0167-2738(99)00188-5.
[21] Y. Yamazaki, R. Hernandez-Sanchez, S.M. Haile, High Total Proton Conductivity in Large-Grained Yttrium-Doped Barium Zirconate, Chem. Mater. 21 (2009) 2755–2762. https://doi.org/10.1021/cm900208w.
[22] K.D. Kreuer, St. Adams, W. Münch, A. Fuchs, U. Klock, J. Maier, Proton conducting alkaline earth zirconates and titanates for high drain electrochemical applications, Solid State Ionics 145 (2001) 295–306. https://doi.org/10.1016/S0167-2738(01)00953-5.
[23] K.D. Kreuer, Proton-Conducting Oxides, Annu. Rev. Mater. Res. 33 (2003) 333–359. https://doi.org/10.1146/annurev.matsci.33.022802.091825.
[24] S. Ricote, N. Bonanos, M.C. Marco de Lucas, G. Caboche, Structural and conductivity study of the proton conductor $BaCe_{(0.9-x)}Zr_xY_{0.1}O_{(3-\delta)}$ at intermediate temperatures, Journal of Power Sources 193 (2009) 189–193. https://doi.org/10.1016/j.jpowsour.2008.11.080.
[25] H. Iwahara, H. Uchida, K. Ono, K. Ogaki, Proton Conduction in Sintered Oxides Based on BaCeO3, J. Electrochem. Soc. 135 (1988) 529–533. https://doi.org/10.1149/1.2095649.
[26] K.H. Ryu, S.M. Haile, Chemical stability and proton conductivity of doped $BaCeO_3$–$BaZrO_3$ solid solutions, Solid State Ionics 125 (1999) 355–367. https://doi.org/10.1016/S0167-2738(99)00196-4.
[27] D. Han, K. Shinoda, S. Sato, M. Majima, T. Uda, Correlation between electroconductive and structural properties of proton conductive acceptor-doped barium zirconate, J. Mater. Chem. A 3 (2015) 1243–1250. https://doi.org/10.1039/C4TA05701E.
[28] S. Imashuku, T. Uda, Y. Nose, G. Taniguchi, Y. Ito, Y. Awakura, Dependence of Dopant Cations on Microstructure and Proton Conductivity of Barium Zirconate, J. Electrochem. Soc. 156 (2009) B1. https://doi.org/10.1149/1.2999335.
[29] E. Gilardi, E. Fabbri, L. Bi, J.L.M. Rupp, T. Lippert, D. Pergolesi, E. Traversa, Effect of Dopant–Host Ionic Radii Mismatch on Acceptor-Doped Barium Zirconate Microstructure

and Proton Conductivity, J. Phys. Chem. C 121 (2017) 9739–9747. https://doi.org/10.1021/acs.jpcc.7b02163.

[30] A. Magrez, Preparation, sintering, and water incorporation of proton conducting $Ba_{0.99}Zr_{0.8}Y_{0.2}O_3$: comparison between three different synthesis techniques, Solid State Ionics 175 (2004) 585–588. https://doi.org/10.1016/j.ssi.2004.03.045.

[31] Á. Triviño-Peláez, D. Pérez-Coll, M. Aparicio, D.P. Fagg, J. Mosa, G.C. Mather, Processing and characterisation of $BaZr_{0.8}Y_{0.2}O_{3-\delta}$ proton conductor densified at 1200 °C, J. Mater. Chem. A 10 (2022) 4428–4439. https://doi.org/10.1039/D1TA09998A.

[33] K. Katahira, Y. Kohchi, T. Shimura, H. Iwahara, Protonic conduction in Zr-substituted $BaCeO_3$, Solid State Ionics 138 (2000) 91–98. https://doi.org/10.1016/S0167-2738(00)00777-3.

[34] Z. Wu, Y. Zhang, Z. Liu, H. Ma, X. Jin, G. Yang, Y. Shi, Z. Shao, S. Li, Rapid Gas-Phase Synthesis of the Perovskite-Type $BaCe_{0.7}Zr_{0.1}Y_{0.1}Yb_{0.1}O_{3-\delta}$ Proton-Conducting Nanocrystalline Electrolyte for Intermediate-Temperature Solid Oxide Fuel Cells, ACS Appl. Mater. Interfaces 14 (2022) 47568–47577. https://doi.org/10.1021/acsami.2c11492.

[35] M. Dudek, B. Lis, R. Lach, S. Daugėla, T. Šalkus, A. Kežionis, M. Mosiałek, M. Sitarz, A. Rapacz-Kmita, P. Grzywacz, Samples of $Ba_{1-x}Sr_xCe_{0.9}Y_{0.1}O_{3-\delta}$, $0 < x < 0.1$, with Improved Chemical Stability in CO_2-H_2 Gas-Involving Atmospheres as Potential Electrolytes for a Proton Ceramic Fuel Cell, Materials 13 (2020) 1874. https://doi.org/10.3390/ma13081874.

[36] Z.U.D. Babar, M.B. Hanif, J.-T. Gao, C.-J. Li, C.-X. Li, Sintering behavior of $BaCe_{0.7}Zr_{0.1}Y_{0.2}O_{3-\delta}$ electrolyte at 1150 °C with the utilization of CuO and Bi_2O_3 as sintering aids and its electrical performance, International Journal of Hydrogen Energy 47 (2022) 7403–7414. https://doi.org/10.1016/j.ijhydene.2021.12.075.

[37] S. Wang, F. Zhao, L. Zhang, K. Brinkman, F. Chen, Stability and electrical property of $Ba_{1-x}Sr_xCe_{0.8}Y_{0.2}O_{3-\delta}$ high temperature proton conductor, Journal of Alloys and Compounds 506 (2010) 263–267. https://doi.org/10.1016/j.jallcom.2010.06.188.

[38] D. Yun, J. Kim, S.-J. Kim, J.-H. Lee, J.-N. Kim, H. Yoon, J. Yu, M. Kwak, H. Yoon, Y. Cho, C.-Y. Yoo, Structural and Electrochemical Properties of Dense Yttria-Doped Barium Zirconate Prepared by Solid-State Reactive Sintering, Energies 11 (2018) 3083. https://doi.org/10.3390/en11113083.

[39] G. Heras-Juaristi, U. Amador, J. Romero de Paz, R.O. Fuentes, A.L. Chinelatto, C. Ritter, D.P. Fagg, D. Pérez-Coll, G.C. Mather, Structures, Phase Fields, and Mixed Protonic–Electronic Conductivity of Ba-Deficient, Pr-Substituted $BaZr_{0.7}Ce_{0.2}Y_{0.1}O_{3-\delta}$, Inorg. Chem. 57 (2018) 15023–15033. https://doi.org/10.1021/acs.inorgchem.8b02956.

[40] F. Iguchi, T. Tsurui, N. Sata, Y. Nagao, H. Yugami, The relationship between chemical composition distributions and specific grain boundary conductivity in Y-doped $BaZrO_3$ proton conductors, Solid State Ionics 180 (2009) 563–568. https://doi.org/10.1016/j.ssi.2008.12.006.

[41] H. Guo, Y. Li, L. Jiang, Y. Sha, S. Guo, D. Han, Transport properties of the $Ba(Zr,Ce,Y,Yb)O_{3-\delta}$ proton conductor: the real role of co-substitution of Y and Yb, J. Mater. Chem. A (2024) 10.1039.D3TA07486B. https://doi.org/10.1039/D3TA07486B.

[42] S. Ricote, N. Bonanos, G. Caboche, Water vapour solubility and conductivity study of the proton conductor $BaCe_{(0.9-x)}Zr_xY_{0.1}O_{(3-\delta)}$, Solid State Ionics 180 (2009) 990–997. https://doi.org/10.1016/j.ssi.2009.03.016.

[43] H. Matsumoto, Y. Kawasaki, N. Ito, M. Enoki, T. Ishihara, Relation Between Electrical Conductivity and Chemical Stability of $BaCeO_3$-Based Proton Conductors with Different Trivalent Dopants, (n.d.).

[44] Z. Shi, W. Sun, Z. Wang, J. Qian, W. Liu, Samarium and Yttrium Codoped $BaCeO_3$ Proton Conductor with Improved Sinterability and Higher Electrical Conductivity, ACS Appl. Mater. Interfaces 6 (2014) 5175–5182. https://doi.org/10.1021/am500467m.

[45] N. Zakowsky, S. Williamson, J. Irvine, Elaboration of CO_2 tolerance limits of BaCe0.9Y0.1O3–δ electrolytes for fuel cells and other applications, Solid State Ionics 176 (2005) 3019–3026. https://doi.org/10.1016/j.ssi.2005.09.040.

[46] R. Sažinas, M.F. Sunding, A. Thøgersen, I. Sakaguchi, T. Norby, T. Grande, J.M. Polfus, Surface reactivity and cation non-stoichiometry in $BaZr_{1-x}Y_xO_{3-\delta}$ (x = 0–0.2) exposed to CO_2 at elevated temperature, J. Mater. Chem. A 7 (2019) 3848–3856. https://doi.org/10.1039/C8TA11021B.

[47] L. Bi, S.P. Shafi, E. Traversa, Y-doped $BaZrO_3$ as a chemically stable electrolyte for proton-conducting solid oxide electrolysis cells (SOECs), J. Mater. Chem. A 3 (2015) 5815–5819. https://doi.org/10.1039/C4TA07202B.

[48] F. Iguchi, T. Tsurui, N. Sata, Y. Nagao, H. Yugami, The relationship between chemical composition distributions and specific grain boundary conductivity in Y-doped $BaZrO_3$ proton conductors, Solid State Ionics 180 (2009) 563–568. https://doi.org/10.1016/j.ssi.2008.12.006.

[49] S.M. Haile, G. Staneff, K.H. Ryu, Non-stoichiometry, grain boundary transport and chemical stability of proton conducting perovskites, (n.d.).

[50] K.S. Knight, Structural phase transitions, oxygen vacancy ordering and protonation in doped $BaCeO_3$: results from time-of-flight neutron powder diffraction investigations, Solid State Ionics 145 (2001) 275–294. https://doi.org/10.1016/S0167-2738(01)00952-3.

[51] I. Charrier-Cougoulic, T. Pagnier, G. Lucazeau, Raman Spectroscopy of Perovskite-Type $BaCe_xZr_{1-x}O_3$($0 \leqslant x \leqslant 1$), Journal of Solid State Chemistry 142 (1999) 220–227. https://doi.org/10.1006/jssc.1998.8038.

[52] Z. Zhong, Stability and conductivity study of the $BaCe_{0.9-x}Zr_xY_{0.1}O_{2.95}$ systems, Solid State Ionics 178 (2007) 213–220. https://doi.org/10.1016/j.ssi.2006.12.007.

[53] E. Fabbri, A. Depifanio, E. Dibartolomeo, S. Licoccia, E. Traversa, Tailoring the chemical stability of $Ba(Ce_{0.8-x}Zr_x)Y_{0.2}O_{3-\delta}$ protonic conductors for Intermediate Temperature Solid Oxide Fuel Cells (IT-SOFCs), Solid State Ionics 179 (2008) 558–564. https://doi.org/10.1016/j.ssi.2008.04.002.

[54] S. Barison, M. Battagliarin, T. Cavallin, S. Daolio, L. Doubova, M. Fabrizio, C. Mortalò, S. Boldrini, R. Gerbasi, Barium Non-Stoichiometry Role on the Properties of $Ba_{1+x}Ce_{0.65}Zr_{0.20}Y_{0.15}O_{3-\delta}$ Proton Conductors for IT-SOFCs, Fuel Cells 8 (2008) 360–368. https://doi.org/10.1002/fuce.200800021.

[55] Y. Zhang, D. Xie, B. Chi, J. Pu, J. Li, D. Yan, Basic properties of proton conductor $BaZr_{0.1}Ce_{0.7}Y_{0.1}Yb_{0.1}O_{3-\delta}$(BZCYYb) material, Asia‐Pac J Chem Eng 14 (2019). https://doi.org/10.1002/apj.2322.

[56] Y. Yamazaki, R. Hernandez-Sanchez, S.M. Haile, Cation non-stoichiometry in yttrium-doped barium zirconate: phase behavior, microstructure, and proton conductivity, J. Mater. Chem. 20 (2010) 8158. https://doi.org/10.1039/c0jm02013c.

[57] L. Doubova, S. Barison, S. Boldrini, M. Fabrizio, C. Mortalò, C. Pagura, Conductivity studies of sol-gel prepared $BaCe_{0.85-x}Zr_xY_{0.15}O_{3-\delta}$ solid electrolytes using impedance spectroscopy, J Appl Electrochem 39 (2009) 2129–2141. https://doi.org/10.1007/s10800-009-9932-0.

[58] G. Zhou, Y. Li, Y. Luo, W. Huang, B. Li, Effect of A-site modification on electrical properties and chemical stability of $BaCaCe_{0.5}Zr_{0.3}Y_{0.2}O_{3-\delta}$ proton-conducting electrolyte, Ceramics International 49 (2023) 11184–11196. https://doi.org/10.1016/j.ceramint.2022.11.317.

[59] Q.-Y. Zhang, Effect of Ba non-stoichiometry in $Ba_{1-x}Zr_{0.1}Ce_{0.7}Y_{0.2}O_{3-\delta}$ on its structure defect, sinterability and hydrogen permeability, Ceramics International (2020) 10.

[60] Y. Guo, R. Ran, Z. Shao, S. Liu, Effect of Ba nonstoichiometry on the phase structure, sintering, electrical conductivity and phase stability of $Ba_{1\pm x}Ce_{0.4}Zr_{0.4}Y_{0.2}O_{3-\delta}$ ($0 \leqslant x \leqslant$

0.20) proton conductors, International Journal of Hydrogen Energy 36 (2011) 8450–8460. https://doi.org/10.1016/j.ijhydene.2011.04.037.

[61] I.-H. Kim, D.-K. Lim, Y. Namgung, H. Bae, J.-Y. Park, S.-J. Song, Electrical Properties of $BaZr_{0.5}Ce_{0.3}Y_{0.1}Yb_{0.1}O_{3-\delta}$ Proton Conductor for Reversible Proton-Conducting Solid Oxide Electrochemical Cells, SSRN Journal (2022). https://doi.org/10.2139/ssrn.4182355.

[62] R. Guo, L. Yang, Y. Wang, Y. Xiao, R. Guan, M. Wang, T. He, Enhanced sintering and electrical properties of proton-conducting electrolytes through Cu doping in $BaZr_{0.5}Ce_{0.3}Y_{0.2}O_3$, Ceramics International 48 (2022) 11793–11804. https://doi.org/10.1016/j.ceramint.2022.01.039.

[63] S. Barison, M. Battagliarin, T. Cavallin, L. Doubova, M. Fabrizio, C. Mortalò, S. Boldrini, L. Malavasi, R. Gerbasi, High conductivity and chemical stability of $BaCe_{1-x-y}Zr_xY_yO_{3-\delta}$ proton conductors prepared by a sol–gel method, J. Mater. Chem. 18 (2008) 5120. https://doi.org/10.1039/b808344d.

[64] M. Marrony. Proton-conducting ceramics: from fundamentals to applied research. CRC Press, 2015.

[65] A. Falkenstein, R.A. De Souza, W.A. Meulenberg, M. Martin, A quantitative analysis of two-fold electrical conductivity relaxation behaviour in mixed proton–oxide-ion–electron conductors upon hydration, Phys. Chem. Chem. Phys. 22 (2020) 25032–25041. https://doi.org/10.1039/D0CP03264F.

[66] D. Han, N. Hatada, T. Uda, Chemical Expansion of Yttrium-Doped Barium Zirconate and Correlation with Proton Concentration and Conductivity, J. Am. Ceram. Soc. 99 (2016) 3745–3753. https://doi.org/10.1111/jace.14377.

[67] W. Skubida, A. Niemczyk, K. Zheng, X. Liu, K. Świeczek, Crystal Structure, Hydration, and Two-Fold/Single-Fold Diffusion Kinetics in Proton-Conducting $Ba_{0.9}La_{0.1}Zr_{0.25}Sn_{0.25}In_{0.5}O_{3-a}$ Oxide, Crystals 8 (2018) 136. https://doi.org/10.3390/cryst8030136.

[68] G. Imai, T. Nakamura, K. Amezawa, Defect chemistry and thermodynamic properties of proton dissolution into $BaZr_{0.9}Y_{0.1}O_{3-\delta}$, Solid State Ionics 303 (2017) 12–15. https://doi.org/10.1016/j.ssi.2017.02.004.

[69] Y. Yamazaki, P. Babilo, S.M. Haile, Defect Chemistry of Yttrium-Doped Barium Zirconate: A Thermodynamic Analysis of Water Uptake, Chem. Mater. 20 (2008) 6352–6357. https://doi.org/10.1021/cm800843s.

[70] S.M. Choi, J.-H. Lee, J. Hong, K.J. Yoon, J.-W. Son, B.-K. Kim, H.-W. Lee, J.-H. Lee, Degradation of hydration kinetics of proton-conducting $Ba(Zr_{0.84}Y_{0.15}Cu_{0.01})O_{3-\delta}$ during conductivity-relaxation experiment, Journal of Power Sources 332 (2016) 299–304. https://doi.org/10.1016/j.jpowsour.2016.09.129.

[71] E. Kim, Y. Yamazaki, S.M. Haile, H.-I. Yoo, Effect of NiO sintering-aid on hydration kinetics and defect-chemical parameters of $BaZr_{0.8}Y_{0.2}O_3$, Solid State Ionics 275 (2015) 23–28. https://doi.org/10.1016/j.ssi.2015.01.001.

[72] J.I. Yeon, H.-I. Yoo, Hydration kinetics of proton-conducting zirconates upon a change of temperature in wet atmosphere, Solid State Ionics 181 (2010) 1323–1327. https://doi.org/10.1016/j.ssi.2010.07.030.

[73] A. Jarry, G.S. Jackson, E.J. Crumlin, B. Eichhorn, S. Ricote, The effect of grain size on the hydration of $BaZr_{0.9}Y_{0.1}O_{3-\delta}$ proton conductor studied by ambient pressure X-ray photoelectron spectroscopy, Phys. Chem. Chem. Phys. 22 (2020) 136–143. https://doi.org/10.1039/C9CP04335G.

[74] K.D. Kreuer, Th. Dippel, Yu.M. Baikov, J. Maier, Water solubility, proton and oxygen diffusion in acceptor doped BaCeO3: A single crystal analysis, Solid State Ionics 86–88 (1996) 613–620. https://doi.org/10.1016/0167-2738(96)00221-4.

[75] T. Schober, Water vapor solubility and electrochemical characterization of the high temperature proton conductor BaZr0.9Y0.1O2.95, Solid State Ionics 127 (2000) 351–360. https://doi.org/10.1016/S0167-2738(99)00283-0.
[76] T. Schober, Water vapor solubility and impedance of the high temperature proton conductor $SrZr_{0.9}Y_{0.1}O_{2.95}$, Solid State Ionics 145 (2001) 319–324. https://doi.org/10.1016/S0167-2738(01)00926-2.
[77] A. Grimaud, Propriétés de conduction mixte O2- / H+ / e- dans quelques phases dérivées de la perovskite: application aux cathodes de piles à combustible H+-SOFC, (n.d.).
[78] L. Ge, J. Jiao, Z. zhu, Q. Zhang, Y. Zheng, H. Chen, L. Guo, A facile method to fabricate proton-conducting $BaZr_{0.85}Y_{0.15}O_3$ electrolyte with a large grain size and high conductivity, Ceramics International 45 (2019) 24946–24952. https://doi.org/10.1016/j.ceramint.2019.08.202.
[79] A. Lindman, E.E. Helgee, G. Wahnström, Comparison of Space-Charge Formation at Grain Boundaries in Proton-Conducting $BaZrO_3$ and $BaCeO_3$, Chem. Mater. 29 (2017) 7931–7941. https://doi.org/10.1021/acs.chemmater.7b02829.
[80] E. Fabbri, D. Pergolesi, S. Licoccia, E. Traversa, Does the increase in Y-dopant concentration improve the proton conductivity of $BaZr_{1-x}Y_xO_{3-\delta}$ fuel cell electrolytes?, Solid State Ionics 181 (2010) 1043–1051. https://doi.org/10.1016/j.ssi.2010.06.007.
[81] S.M. Choi, J.-H. Lee, J. Hong, H. Kim, K.J. Yoon, B.-K. Kim, J.-H. Lee, Effect of sintering atmosphere on phase stability, and electrical conductivity of proton-conducting $Ba(Zr_{0.84}Y_{0.15}Cu_{0.01})O_3$, International Journal of Hydrogen Energy 39 (2014) 7100–7108. https://doi.org/10.1016/j.ijhydene.2014.02.072.
[82] Z. Liu, X. Wang, M. Liu, J. Liu, Enhancing sinterability and electrochemical properties of $Ba(Zr_{0.1}Ce_{0.7}Y_{0.2})O_{3-\delta}$ proton conducting electrolyte for solid oxide fuel cells by addition of NiO, International Journal of Hydrogen Energy 43 (2018) 13501–13511. https://doi.org/10.1016/j.ijhydene.2018.05.089.
[83] B. Wang, L. Bi, X.S. Zhao, Exploring the role of NiO as a sintering aid in $BaZr_{0.1}Ce_{0.7}Y_{0.2}O_{3-\delta}$ electrolyte for proton-conducting solid oxide fuel cells, Journal of Power Sources 399 (2018) 207–214. https://doi.org/10.1016/j.jpowsour.2018.07.087.
[84] D. Vignesh, B.K. Sonu, E. Rout, Factors Constituting Proton Trapping in $BaCeO_3$ and $BaZrO_3$ Perovskite Proton Conductors in Fuel Cell Technology: A Review, Energy Fuels 36 (2022) 7219–7244. https://doi.org/10.1021/acs.energyfuels.2c00650.
[85] H. Takahashi, I. Yashima, K. Amezawa, K. Eguchi, H. Matsumoto, H. Takamura, S. Yamaguchi, First-Principles Calculations for the Energetics of the Hydration Reaction of Acceptor-Doped $BaZrO_3$, Chem. Mater. 29 (2017) 1518–1526. https://doi.org/10.1021/acs.chemmater.6b03907.
[86] D. Han, N. Hatada, T. Uda, Microstructure, Proton Concentration and Proton Conductivity of Barium Zirconate Doped with Ho, Er, Tm and Yb, J. Electrochem. Soc. 163 (2016) F470–F476. https://doi.org/10.1149/2.0551606jes.
[87] D.R. Clark, H. Zhu, D.R. Diercks, S. Ricote, R.J. Kee, A. Almansoori, B.P. Gorman, R.P. O'Hayre, Probing Grain-Boundary Chemistry and Electronic Structure in Proton-Conducting Oxides by Atom Probe Tomography, Nano Lett. 16 (2016) 6924–6930. https://doi.org/10.1021/acs.nanolett.6b02918.
[88] K.D. Kreuer, St. Adams, W. Münch, A. Fuchs, U. Klock, J. Maier, Proton conducting alkaline earth zirconates and titanates for high drain electrochemical applications, Solid State Ionics 145 (2001) 295–306. https://doi.org/10.1016/S0167-2738(01)00953-5.
[89] K.D. Kreuer, Proton-Conducting Oxides, Annu. Rev. Mater. Res. 33 (2003) 333–359. https://doi.org/10.1146/annurev.matsci.33.022802.091825.
[90] J.M. Polfus, M.-L. Fontaine, A. Thøgersen, M. Riktor, T. Norby, R. Bredesen, Solubility of transition metal interstitials in proton conducting $BaZrO_3$ and similar perovskite oxides, J. Mater. Chem. A 4 (2016) 8105–8112. https://doi.org/10.1039/C6TA02377K.

[91] C. Kjølseth, H. Fjeld, Ø. Prytz, P.I. Dahl, C. Estournès, R. Haugsrud, T. Norby, Space–charge theory applied to the grain boundary impedance of proton conducting $BaZr_{0.9}Y_{0.1}O_{3-\delta}$, Solid State Ionics 181 (2010) 268–275. https://doi.org/10.1016/j.ssi.2010.01.014.

[92] D. Han, T. Uda, The best composition of an Y-doped $BaZrO_3$ electrolyte: selection criteria from transport properties, microstructure, and phase behavior, J. Mater. Chem. A 6 (2018) 18571–18582. https://doi.org/10.1039/C8TA06280C.

[93] Y. Yamazaki, F. Blanc, Y. Okuyama, L. Buannic, J.C. Lucio-Vega, C.P. Grey, S.M. Haile, Proton trapping in yttrium-doped barium zirconate, Nature Mater 12 (2013) 647–651. https://doi.org/10.1038/nmat3638.

[94] E. Makagon, O. Kraynis, R. Merkle, J. Maier, I. Lubomirsky, Non‐Classical Electrostriction in Hydrated Acceptor Doped $BaZrO_3$: Proton Trapping and Dopant Size Effect, Adv Funct Materials 31 (2021) 2104188. https://doi.org/10.1002/adfm.202104188.

[95] J.A. Dawson, I. Tanaka, Proton trapping in Y and Sn Co-doped $BaZrO_3$, J. Mater. Chem. A 3 (2015) 10045–10051. https://doi.org/10.1039/C5TA01450F.

[96] J. Ding, J. Balachandran, X. Sang, W. Guo, J.S. Anchell, G.M. Veith, C.A. Bridges, Y. Cheng, C.M. Rouleau, J.D. Poplawsky, N. Bassiri-Gharb, R.R. Unocic, P. Ganesh, The Influence of Local Distortions on Proton Mobility in Acceptor Doped Perovskites, Chem. Mater. 30 (2018) 4919–4925. https://doi.org/10.1021/acs.chemmater.8b00502.

[97] F.M. Draber, C. Ader, J.P. Arnold, S. Eisele, S. Grieshammer, S. Yamaguchi, M. Martin, Nanoscale percolation in doped $BaZrO_3$ for high proton mobility, Nat. Mater. 19 (2020) 338–346. https://doi.org/10.1038/s41563-019-0561-7.

[98] F.M. Draber, C. Ader, J.P. Arnold, S. Eisele, S. Grieshammer, S. Yamaguchi, M. Martin, Nanoscale percolation in doped $BaZrO_3$ for high proton mobility, Nat. Mater. 19 (2020) 338–346. https://doi.org/10.1038/s41563-019-0561-7.

[99] P. Babilo, S.M. Haile, Enhanced Sintering of Yttrium-Doped Barium Zirconate by Addition of ZnO, J American Ceramic Society 88 (2005) 2362–2368. https://doi.org/10.1111/j.1551-2916.2005.00449.x.

[100] K.-Y. Park, Y. Seo, K.B. Kim, S.-J. Song, B. Park, J.-Y. Park, Enhanced proton conductivity of yttrium-doped barium zirconate with sinterability in protonic ceramic fuel cells, Journal of Alloys and Compounds 639 (2015) 435–444. https://doi.org/10.1016/j.jallcom.2015.03.168.

[101] N. Nasani, Z. Shakel, F.J.A. Loureiro, B.B. Panigrahi, B.B. Kale, D.P. Fagg, Exploring the impact of sintering additives on the densification and conductivity of $BaCe_{0.3}Zr_{0.55}Y_{0.15}O_{3-\delta}$ electrolyte for protonic ceramic fuel cells, Journal of Alloys and Compounds 862 (2021) 158640. https://doi.org/10.1016/j.jallcom.2021.158640.

[102] S. Nikodemski, J. Tong, R. O'Hayre, Solid-state reactive sintering mechanism for proton conducting ceramics, Solid State Ionics 253 (2013) 201–210. https://doi.org/10.1016/j.ssi.2013.09.025.

[103] C. Peng, J. Melnik, J. Li, J. Luo, A.R. Sanger, K.T. Chuang, ZnO-doped $BaZr_{0.85}Y_{0.15}O_{3-\delta}$ proton-conducting electrolytes: Characterization and fabrication of thin films, Journal of Power Sources 190 (2009) 447–452. https://doi.org/10.1016/j.jpowsour.2009.01.020.

[104] C.-Y. Yoo, D.S. Yun, J.H. Joo, J.H. Yu, The effects of NiO addition on the structure and transport properties of proton conducting $BaZr_{0.8}Y_{0.2}O_3$, Journal of Alloys and Compounds 621 (2015) 263–267. https://doi.org/10.1016/j.jallcom.2014.09.207.

[105] R.M. German, P. Suri, S.J. Park, Review: liquid phase sintering, J Mater Sci 44 (2009) 1–39. https://doi.org/10.1007/s10853-008-3008-0.

[106] E. Kim, Y. Yamazaki, S.M. Haile, H.-I. Yoo, Effect of NiO sintering-aid on hydration kinetics and defect-chemical parameters of $BaZr_{0.8}Y_{0.2}O_3$, Solid State Ionics 275 (2015) 23–28. https://doi.org/10.1016/j.ssi.2015.01.001.

[107] J. Tong, D. Clark, M. Hoban, R. O'Hayre, Cost-effective solid-state reactive sintering method for high conductivity proton conducting yttrium-doped barium zirconium ceramics, Solid State Ionics 181 (2010) 496–503. https://doi.org/10.1016/j.ssi.2010.02.008.

[108] J. Jiao, Q. Li, Y. Gu, Y. Luo, L. Ge, Y. Zheng, H. Chen, L. Guo, Effect of BaO-B_2O_3 composite sintering aid on sinterability and electrical property of $BaZr_{0.85}Y_{0.15}O_3$ ceramic, Ceramics International 45 (2019) 13679–13684. https://doi.org/10.1016/j.ceramint.2019.04.062.

[109] S. Le, J. Zhang, X. Zhu, J. Zhai, K. Sun, Sintering and electrochemical performance of Y_2O_3-doped barium zirconate with Bi_2O_3 as sintering aids, Journal of Power Sources 232 (2013) 219–223. https://doi.org/10.1016/j.jpowsour.2013.01.065.

[110] N. Nasani, D. Pukazhselvan, A.V. Kovalevsky, A.L. Shaula, D.P. Fagg, Conductivity recovery by redox cycling of yttrium doped barium zirconate proton conductors and exsolution of Ni-based sintering additives, Journal of Power Sources 339 (2017) 93–102. https://doi.org/10.1016/j.jpowsour.2016.11.036.

[111] Y. Huang, R. Merkle, J. Maier, Effects of NiO addition on sintering and proton uptake of $Ba(Zr,Ce,Y)O_{3-\delta}$, J. Mater. Chem. A 9 (2021) 14775–14785. https://doi.org/10.1039/D1TA02555D.

[112] D. Han, A. Kuramitsu, T. Onishi, Y. Noda, M. Majima, T. Uda, Fabrication of protonic ceramic fuel cells via infiltration with Ni nanoparticles: A new strategy to suppress NiO diffusion & increase open circuit voltage, Solid State Ionics 345 (2020) 115189. https://doi.org/10.1016/j.ssi.2019.115189.

[113] S. Fang, S. Wang, K.S. Brinkman, Q. Su, H. Wang, F. Chen, Relationship between fabrication method and chemical stability of Ni–$BaZr_{0.8}Y_{0.2}O_3$ membrane, Journal of Power Sources 278 (2015) 614–622. https://doi.org/10.1016/j.jpowsour.2014.12.108.

[114] J. Tong, D. Clark, L. Bernau, M. Sanders, R. O'Hayre, Solid-state reactive sintering mechanism for large-grained yttrium-doped barium zirconate proton conducting ceramics, J. Mater. Chem. 20 (2010) 6333. https://doi.org/10.1039/c0jm00381f.

[115] D. Han, Y. Otani, Y. Noda, T. Onishi, M. Majima, T. Uda, Strategy to improve phase compatibility between proton conductive $BaZr_{0.8}Y_{0.2}O_{3-\delta}$ and nickel oxide, RSC Adv. 6 (2016) 19288–19297. https://doi.org/10.1039/C5RA26947D.

[116] D. Han, S. Uemura, C. Hiraiwa, M. Majima, T. Uda, Detrimental Effect of Sintering Additives on Conducting Ceramics: Yttrium‐Doped Barium Zirconate, ChemSusChem 11 (2018) 4102–4113. https://doi.org/10.1002/cssc.201801837.

[117] Y. Huang, R. Merkle, J. Maier, Effect of NiO addition on proton uptake of $BaZr_{1-x}Y_xO_{3-x}$ and $BaZr_{1-x}Sc_xO_{3-x}$ electrolytes, Solid State Ionics 347 (2020) 115256. https://doi.org/10.1016/j.ssi.2020.115256.

[118] Y. Huang, R. Merkle, D. Zhou, W. Sigle, P.A. Van Aken, J. Maier, Effect of Ni on electrical properties of $Ba(Zr,Ce,Y)O_3$ as electrolyte for protonic ceramic fuel cells, Solid State Ionics 390 (2023) 116113. https://doi.org/10.1016/j.ssi.2022.116113.

[119] Y. Zhang, R. Knibbe, J. Sunarso, Y. Zhong, W. Zhou, Z. Shao, Z. Zhu, Recent Progress on Advanced Materials for Solid-Oxide Fuel Cells Operating Below 500 °C, Adv. Mater. 29 (2017) 1700132. https://doi.org/10.1002/adma.201700132.

[120] L. Bi, S. Boulfrad, E. Traversa, Steam electrolysis by solid oxide electrolysis cells (SOECs) with proton-conducting oxides, Chem. Soc. Rev. 43 (2014) 8255–8270. https://doi.org/10.1039/C4CS00194J.

[121] S. Choi, C.J. Kucharczyk, Y. Liang, X. Zhang, I. Takeuchi, H.-I. Ji, S.M. Haile, Exceptional power density and stability at intermediate temperatures in protonic ceramic fuel cells, Nat Energy 3 (2018) 202–210. https://doi.org/10.1038/s41560-017-0085-9.

[122] F. Liu, D. Diercks, P. Kumar, A. Seong, M.H.A. Jabbar, C. Gumeci, Y. Furuya, N. Dale, T. Oku, M. Usuda, P. Kazempoor, I. Ghamarian, L. Liu, L. Fang, D. Chen, Z. Wang, S.

Skinner, C. Duan, Redesigning protonic ceramic electrochemical cells to lower the operating temperature, Sci. Adv. 11 (2025) eadq2507. https://doi.org/10.1126/sciadv.adq2507.

[123] N.H. Menzler, F. Tietz, S. Uhlenbruck, H.P. Buchkremer, D. Stöver, Materials and manufacturing technologies for solid oxide fuel cells, J Mater Sci 45 (2010) 3109–3135. https://doi.org/10.1007/s10853-010-4279-9.

[124] F. Tietz, Components manufacturing for solid oxide fuel cells, Solid State Ionics (2002).

[125] L. Blum, W.A. Meulenberg, H. Nabielek, R. Steinberger‐Wilckens, Worldwide SOFC Technology Overview and Benchmark, Int J Applied Ceramic Tech 2 (2005) 482–492. https://doi.org/10.1111/j.1744-7402.2005.02049.x.

[126] M.P. Carpanese, A. Barbucci, G. Canu, M. Viviani, $BaCe_{0.85}Y_{0.15}O_{2.925}$ dense layer by wet powder spraying as electrolyte for SOFC/SOEC applications, Solid State Ionics 269 (2015) 80–85. https://doi.org/10.1016/j.ssi.2014.11.014.

[127] M. Jabbari, R. Bulatova, A.I.Y. Tok, C.R.H. Bahl, E. Mitsoulis, J.H. Hattel, Ceramic tape casting: A review of current methods and trends with emphasis on rheological behaviour and flow analysis, Materials Science and Engineering: B 212 (2016) 39–61. https://doi.org/10.1016/j.mseb.2016.07.011.

[128] Y. Li, P.-C. Su, L.M. Wong, S. Wang, Chemical stability study of nanoscale thin film yttria-doped barium cerate electrolyte for micro solid oxide fuel cells, Journal of Power Sources 268 (2014) 804–809. https://doi.org/10.1016/j.jpowsour.2014.06.128.

[129] H. Shi, W. Zhou, R. Ran, Z. Shao, Comparative study of doped ceria thin-film electrolytes prepared by wet powder spraying with powder synthesized via two techniques, Journal of Power Sources 195 (2010) 393–401. https://doi.org/10.1016/j.jpowsour.2009.07.056.

[130] W. Feng, W. Wu, C. Jin, M. Zhou, W. Bian, W. Tang, J.Y. Gomez, R. Boardman, D. Ding, Exploring the structural uniformity and integrity of protonic ceramic thin film electrolyte using wet powder spraying, Journal of Power Sources Advances 11 (2021) 100067. https://doi.org/10.1016/j.powera.2021.100067.

[131] G. Taillades, P. Pers, V. Mao, M. Taillades, High performance anode-supported proton ceramic fuel cell elaborated by wet powder spraying, International Journal of Hydrogen Energy 41 (2016) 12330–12336. https://doi.org/10.1016/j.ijhydene.2016.05.094.

[132] Q. Wang, T. Luo, Y. Tong, M. Dai, X.-Y. Miao, S. Ricote, Z. Zhan, M. Chen, Large-area protonic ceramic cells for hydrogen purification, Separation and Purification Technology 295 (2022) 121301. https://doi.org/10.1016/j.seppur.2022.121301.

[133] R.K. Nishihora, P.L. Rachadel, M.G.N. Quadri, D. Hotza, Manufacturing porous ceramic materials by tape casting—A review, Journal of the European Ceramic Society 38 (2018) 988–1001. https://doi.org/10.1016/j.jeurceramsoc.2017.11.047.

[134] M. Perz, E. Bucher, W. Sitte, T. Griesser, New water-based sol–gel synthesis routes for LaNi0.6Fe0.4O3-δ thin films, Solid State Ionics 273 (2015) 30–34. https://doi.org/10.1016/j.ssi.2014.10.027.

[135] Y. Li, L.M. Wong, C.-C. Yu, S. Wang, P.-C. Su, Pulsed laser deposition of $Ba_{0.5}Sr_{0.5}Co_{0.8}Fe_{0.2}O_{3-\delta}$ thin film cathodes for low temperature solid oxide fuel cells, Surface and Coatings Technology 320 (2017) 344–348. https://doi.org/10.1016/j.surfcoat.2016.12.051.

[136] S. Ricote, R.J. Kee, W.G. Coors, Slip Casting and Solid-State Reactive Sintering of BCZY($BaCe_xZr_{0.9-x}Y_{0.1}O_{3-d}$)-NiO/BCZY Half-Cells, Membranes 12 (2022) 242. https://doi.org/10.3390/membranes12020242.

[137] K. Bakken, A.B. Blichfeld, I. Nylund, D. Chernyshov, J. Glaum, T. Grande, M. Einarsrud, Tailoring Preferential Orientation in $BaTiO_3$‐based Thin Films from Aqueous Chemical Solution Deposition, Chemistry Methods 2 (2022) e202100064. https://doi.org/10.1002/cmtd.202100064.

[138] B. Beyribey, J. Bayne, J. Persky, The effect of dip-coating parameters on the thickness and uniformity of BCZYZ electrolyte layer on porous NiO-BCZYZ tubular supports, Ceramics International 48 (2022) 6046–6051. https://doi.org/10.1016/j.ceramint.2021.11.141.

[139] H.-W. Lin, C.-P. Chang, W.-H. Hwu, M.-D. Ger, The rheological behaviors of screen-printing pastes, Journal of Materials Processing Technology 197 (2008) 284–291. https://doi.org/10.1016/j.jmatprotec.2007.06.067.

[140] L. Ren, X. Luo, H. Zhou, The tape casting process for manufacturing low‐temperature co‐fired ceramic green sheets: A review, J Am Ceram Soc 101 (2018) 3874–3889. https://doi.org/10.1111/jace.15694.

[141] N.H. Menzler, J. Malzbender, P. Schoderböck, R. Kauert, H.P. Buchkremer, Sequential Tape Casting of Anode‐Supported Solid Oxide Fuel Cells, Fuel Cells 14 (2014) 96–106. https://doi.org/10.1002/fuce.201300153.

[142] X. Chen, W. Ni, X. Du, Z. Sun, T. Zhu, Q. Zhong, M. Han, Electrochemical property of multi-layer anode supported solid oxide fuel cell fabricated through sequential tape-casting and co-firing, Journal of Materials Science & Technology 35 (2019) 695–701. https://doi.org/10.1016/j.jmst.2018.10.015.

[143] K. Leonard, M.E. Ivanova, A. Weber, W. Deibert, W.A. Meulenberg, T. Ishihara, H. Matsumoto, Anode supported planar 5×5 cm^2 $SrZr_{0.5}Ce_{0.4}Y_{0.1}O_{2.95}$ based solid oxide protonic fuel cells via sequential tape-casting, Solid State Ionics 379 (2022) 115918. https://doi.org/10.1016/j.ssi.2022.115918.

[144] S. Hossain, A.M. Abdalla, J.H. Zaini, C.D. Savaniu, J.T.S. Irvine, A.K. Azad, Highly dense and novel proton conducting materials for SOFC electrolyte, International Journal of Hydrogen Energy 42 (2017) 27308–27322. https://doi.org/10.1016/j.ijhydene.2017.09.067.

[145] P. Ried, C. Lorenz, A. Brönstrup, T. Graule, N.H. Menzler, W. Sitte, P. Holtappels, Processing of YSZ screen printing pastes and the characterization of the electrolyte layers for anode supported SOFC, Journal of the European Ceramic Society 28 (2008) 1801–1808. https://doi.org/10.1016/j.jeurceramsoc.2007.11.018.

[146] H. Shi, W. Zhou, R. Ran, Z. Shao, Comparative study of doped ceria thin-film electrolytes prepared by wet powder spraying with powder synthesized via two techniques, Journal of Power Sources 195 (2010) 393–401. https://doi.org/10.1016/j.jpowsour.2009.07.056.

[147] W. Feng, W. Wu, C. Jin, M. Zhou, W. Bian, W. Tang, J.Y. Gomez, R. Boardman, D. Ding, Exploring the structural uniformity and integrity of protonic ceramic thin film electrolyte using wet powder spraying, Journal of Power Sources Advances 11 (2021) 100067. https://doi.org/10.1016/j.powera.2021.100067.

[148] L. Fan, H. Xie, P.-C. Su, Spray coating of dense proton-conducting $BaCe_{0.7}Zr_{0.1}Y_{0.2}O_3$ electrolyte for low temperature solid oxide fuel cells, International Journal of Hydrogen Energy 41 (2016) 6516–6525. https://doi.org/10.1016/j.ijhydene.2016.03.001.

[149] M. Saqib, I.-G. Choi, H. Bae, K. Park, J.-S. Shin, Y.-D. Kim, J.-I. Lee, M. Jo, Y.-C. Kim, K.-S. Lee, S.-J. Song, E.D. Wachsman, J.-Y. Park, Transition from perovskite to misfit-layered structure materials: a highly oxygen deficient and stable oxygen electrode catalyst, Energy Environ. Sci. 14 (2021) 2472–2484. https://doi.org/10.1039/d0ee02799e.

[150] Z. Liu, M. Zhou, M. Chen, D. Cao, J. Shao, M. Liu, J. Liu, A high-performance intermediate-to-low temperature protonic ceramic fuel cell with in-situ exsolved nickel nanoparticles in the anode, Ceramics International 46 (2020) 19952–19959. https://doi.org/10.1016/j.ceramint.2020.05.062.

[151] N.T.Q. Nguyen, H.H. Yoon, Preparation and evaluation of $BaZr_{0.1}Ce_{0.7}Y_{0.1}Yb_{0.1}O_3$ (BZCYYb) electrolyte and BZCYYb-based solid oxide fuel cells, Journal of Power Sources 231 (2013) 213–218. https://doi.org/10.1016/j.jpowsour.2013.01.011.

[152] N. Sata, R. Costa, Protonic ceramic electrochemical cells in a metal supported architecture: challenges, status and prospects, Prog. Energy 6 (2024) 032002. https://doi.org/10.1088/2516-1083/ad3f6b.
[153] Y.S. Kim, W. Chang, H.J. Jeong, K.H. Kim, H.S. Park, J.H. Shim, High performance of protonic ceramic fuel cells with 1-μm-thick electrolytes fabricated by inkjet printing, Additive Manufacturing 71 (2023) 103590. https://doi.org/10.1016/j.addma.2023.103590.
[154] Z. Zakaria, Z. Awang Mat, S.H. Abu Hassan, Y. Boon Kar, A review of solid oxide fuel cell component fabrication methods toward lowering temperature, Int J Energy Res 44 (2020) 594–611. https://doi.org/10.1002/er.4907.
[155] H. An, H.-W. Lee, B.-K. Kim, J.-W. Son, K.J. Yoon, H. Kim, D. Shin, H.-I. Ji, J.-H. Lee, A 5 × 5 cm2 protonic ceramic fuel cell with a power density of 1.3 W cm–2 at 600 °C, Nat Energy 3 (2018) 870–875. https://doi.org/10.1038/s41560-018-0230-0.
[156] J. Dailly, M. Marrony, BCY-based proton conducting ceramic cell: 1000 h of long term testing in fuel cell application, Journal of Power Sources 240 (2013) 323–327. https://doi.org/10.1016/j.jpowsour.2013.04.028.
[157] J. Dailly, M. Ancelin, M. Marrony, Long term testing of BCZY-based protonic ceramic fuel cell PCFC: Micro-generation profile and reversible production of hydrogen and electricity, Solid State Ionics 306 (2017) 69–75. https://doi.org/10.1016/j.ssi.2017.03.002.
[158] F. Liu, H. Deng, D. Diercks, P. Kumar, M.H.A. Jabbar, C. Gumeci, Y. Furuya, N. Dale, T. Oku, M. Usuda, P. Kazempoor, L. Fang, D. Chen, B. Liu, C. Duan, Lowering the operating temperature of protonic ceramic electrochemical cells to <450 °C, Nat Energy (2023). https://doi.org/10.1038/s41560-023-01350-4.
[159] W. Feng, W. Wu, Z. Zhao, J.Y. Gomez, C.J. Orme, W. Tang, W. Bian, C. Priest, F.F. Stewart, C. Jin, D. Ding, Mathematical Model-Assisted Ultrasonic Spray Coating for Scalable Production of Large-Sized Solid Oxide Electrochemical Cells, ACS Appl. Mater. Interfaces 15 (2023) 31430–31437. https://doi.org/10.1021/acsami.3c04208.
[160] M. Wolff, K. Wilkner, D. Sebold, N.H. Menzler, Wet powder spraying – A versatile and highly effective technique for the application of spinel-type protective coatings on SOC interconnects, (n.d.).
[161] J. Laurencin, G. Delette, F. Lefebvre-Joud, M. Dupeux, A numerical tool to estimate SOFC mechanical degradation: Case of the planar cell configuration, Journal of the European Ceramic Society 28 (2008) 1857–1869. https://doi.org/10.1016/j.jeurceramsoc.2007.12.025.
[162] J.H. Yu, G.W. Park, S. Lee, S.K. Woo, Microstructural effects on the electrical and mechanical properties of Ni–YSZ cermet for SOFC anode, Journal of Power Sources 163 (2007) 926–932. https://doi.org/10.1016/j.jpowsour.2006.10.017.
[163] S. Biswas, T. Nithyanantham, S. Nambiappan Thangavel, S. Bandopadhyay, High-temperature mechanical properties of reduced NiO–8YSZ anode-supported bi-layer SOFC structures in ambient air and reducing environments, Ceramics International 39 (2013) 3103–3111. https://doi.org/10.1016/j.ceramint.2012.09.090.
[164] J. Wei, T. Osipova, J. Malzbender, M. Krüger, Mechanical characterization of SOFC/SOEC cells, Ceramics International 44 (2018) 11094–11100. https://doi.org/10.1016/j.ceramint.2018.03.103.
[165] L. Blum, L.G.J. de Haart, J. Malzbender, N. Margaritis, N.H. Menzler, Anode-Supported Solid Oxide Fuel Cell Achieves 70 000 Hours of Continuous Operation, Energy Technology 4 (2016) 939–942. https://doi.org/10.1002/ente.201600114.
[166] N. Shi, K. Zhu, Y. Xie, D. Huan, J. Hyodo, Y. Yamazaki, Investigation of Water Impacts on Surface Properties and Performance of Air‐Electrode in Reversible Protonic Ceramic Cells, (2024).
[167] W. Tang, W. Bian, H. Ding, Y. Ding, Z. Zhao, Q. Sun, S. Koomson, Y. Wang, B. Xu, P. Dong, D. Chen, J.Y. Gomez, W. Feng, W. Wu, M. Zhou, Y. Dong, H. Luo, J. Li, D.

Ding, Sintering protonic zirconate cells with enhanced electrolysis stability and Faradaic efficiency, Nat. Synth (2025). https://doi.org/10.1038/s44160-025-00765-z.

[168] H. Yang, Hydration-induced stiffness enabling robust thermal cycling of high temperature fuel cells cathode, Nature Communications (2025).

[169] Z. Huang, Y. Yang, H. Lv, C. Shi, Y. Ling, J. Zhou, S. Wang, An interesting application-oriented design of high-strength anode support for protonic ceramic fuel cells by a non-proton-conducting cermet, Journal of Power Sources 521 (2022) 230989. https://doi.org/10.1016/j.jpowsour.2022.230989.

[170] H.L. Frandsen, T. Ramos, A. Faes, M. Pihlatie, K. Brodersen, Optimization of the strength of SOFC anode supports, Journal of the European Ceramic Society 32 (2012) 1041–1052. https://doi.org/10.1016/j.jeurceramsoc.2011.11.015.

[171] Y. Xie, Measurement of Flexural Strengths of SOFC Components, Proc. Vol. 2005–07 (2005) 915–922. https://doi.org/10.1149/200507.0915PV.

[172] D. Miura, Y. Ishida, T. Miyasaka, H. Aoki, A. Shinya, Reliability of Different Bending Test Methods for Dental Press Ceramics, Materials 13 (2020) 5162. https://doi.org/10.3390/ma13225162.

[173] D. K. Shetty, A. R. Rosenfield, W. H. Duckworth, P. R. Held, A biaxial‐flexure test for evaluating ceramic strengths. Journal of the American Ceramic Society, 66(1983), 36-42.

[174] G. Pećanac, T. Bause, J. Malzbender, Ring-on-ring testing of thin, curved bi-layered materials, Journal of the European Ceramic Society 31 (2011) 2037–2042. https://doi.org/10.1016/j.jeurceramsoc.2011.05.021.

[175] J. Malzbender, R.W. Steinbrech, Fracture test of thin sheet electrolytes for solid oxide fuel cells, Journal of the European Ceramic Society 27 (2007) 2597–2603. https://doi.org/10.1016/j.jeurceramsoc.2006.11.071.

[176] Y. Zeng, M. Kindelmann, K. Leonard, L.-A. Schäfer, K. Yao, J. Malzbender, M. Müller, O. Guillon, M.E. Ivanova, N.H. Menzler, Characterization of high Zr/Ce ratio $Ba(Zr,Ce,Y)O_{3-\delta}$ proton conductors: investigating the impact of Y on the properties of materials, Phys. Chem. Chem. Phys. 27 (2025) 885–896. https://doi.org/10.1039/D4CP04384G.

[177] M. Choi, J. Paik, D. Kim, D. Woo, J. Lee, S.J. Kim, J. Lee, W. Lee, Exceptionally high performance of protonic ceramic fuel cells with stoichiometric electrolytes, Energy Environ. Sci. 14 (2021) 6476–6483. https://doi.org/10.1039/D1EE01497H.

[178] D. Han, L. Jiang, P. Zhong, Improving phase compatibility between doped $BaZrO_3$ and NiO in protonic ceramic cells via tuning composition and dopant, International Journal of Hydrogen Energy 46 (2021) 8767–8777. https://doi.org/10.1016/j.ijhydene.2020.12.075.

[179] K. Leonard, M.E. Ivanova, A. Weber, W. Deibert, W.A. Meulenberg, T. Ishihara, H. Matsumoto, Anode supported planar 5 × 5 cm^2 $SrZr_{0.5}Ce_{0.4}Y_{0.1}O_{2.95}$ based solid oxide protonic fuel cells via sequential tape-casting, Solid State Ionics 379 (2022) 115918. https://doi.org/10.1016/j.ssi.2022.115918.

[180] Z. Wang, L. Ding, S. Yu, H. Xu, X. Hao, Y. Sun, T. He, Effect of Two Different ZnO Addition Strategies on the Sinterability and Conductivity of the $BaZr_{0.4}Ce_{0.4}Y_{0.2}O_{3-\delta}$ Proton-Conducting Ceramic Electrolyte, ACS Appl. Energy Mater. 5 (2022) 3369–3379. https://doi.org/10.1021/acsaem.1c03989.

[181] Z. Liu, X. Wang, M. Liu, J. Liu, Enhancing sinterability and electrochemical properties of $Ba(Zr_{0.1}Ce_{0.7}Y_{0.2})O_{3-\delta}$ proton conducting electrolyte for solid oxide fuel cells by addition of NiO, International Journal of Hydrogen Energy 43 (2018) 13501–13511. https://doi.org/10.1016/j.ijhydene.2018.05.089.

[182] K.-R. Lee, C.-J. Tseng, S.-C. Jang, J.-C. Lin, K.-W. Wang, J.-K. Chang, T.-C. Chen, S.-W. Lee, Fabrication of anode-supported thin BCZY electrolyte protonic fuel cells using

NiO sintering aid, International Journal of Hydrogen Energy 44 (2019) 23784–23792. https://doi.org/10.1016/j.ijhydene.2019.07.097.

[183] S.J. Yang, W. Chang, H.J. Jeong, D.H. Kim, J.H. Shim, High-performance protonic ceramic fuel cells with electrolyte-electrode composite cathode functional layers, Intl J of Energy Research 46 (2022) 6553–6561. https://doi.org/10.1002/er.7591.

[184] L.Q. Le, C. Meisel, C.H. Hernandez, J. Huang, Y. Kim, R. O'Hayre, N.P. Sullivan, Performance degradation in proton-conducting ceramic fuel cell and electrolyzer stacks, Journal of Power Sources 537 (2022) 231356. https://doi.org/10.1016/j.jpowsour.2022.231356.

[185] C. Duan, D. Hook, Y. Chen, J. Tong, R. O'Hayre, Zr and Y co-doped perovskite as a stable, high performance cathode for solid oxide fuel cells operating below 500 °C, Energy Environ. Sci. 10 (2017) 176–182. https://doi.org/10.1039/C6EE01915C.

[186] J.G. Lee, A.B. Naden, C.D. Savaniu, P.A. Connor, J.L. Payne, J. M. Skelton, A.S. Gibbs, J. Hui, S. C. Parker, J.T.S. Irvine, Use of Interplay between A‐Site Non‐Stoichiometry and Hydroxide Doping to Deliver Novel Proton‐Conducting Perovskite Oxides, Adv. Energy Mater. 11 (2021) 2101337. https://doi.org/10.1002/aenm.202101337.

[187] K. Park, H. Bae, H. Kim, I. Choi, M. Jo, G. Park, M. Asif, A. Bhardwaj, K. Lee, Y. Kim, S. Song, E.D. Wachsman, J. Park, Understanding the Highly Electrocatalytic Active Mixed Triple Conducting $Na_xCa_{3-x}Co_4O_{9-\delta}$ Oxygen Electrode Materials, Advanced Energy Materials 13 (2023) 2202999. https://doi.org/10.1002/aenm.202202999.

[188] M. Saqib, I.-G. Choi, H. Bae, K. Park, J.-S. Shin, Y.-D. Kim, J.-I. Lee, M. Jo, Y.-C. Kim, K.-S. Lee, S.-J. Song, E.D. Wachsman, J.-Y. Park, Transition from perovskite to misfit-layered structure materials: a highly oxygen deficient and stable oxygen electrode catalyst, Energy Environ. Sci. 14 (2021) 2472–2484. https://doi.org/10.1039/D0EE02799E.

[189] Y. Zhang, B. Chen, D. Guan, M. Xu, R. Ran, M. Ni, W. Zhou, R. O'Hayre, Z. Shao, Thermal-expansion offset for high-performance fuel cell cathodes, Nature 591 (2021) 246–251. https://doi.org/10.1038/s41586-021-03264-1.

[190] X. Chen, N. Yu, Y. Song, T. Liu, H. Xu, D. Guan, Z. Li, W. Huang, Z. Shao, F. Ciucci, M. Ni, Synergistic Bulk and Surface Engineering for Expeditious and Durable Reversible Protonic Ceramic Electrochemical Cells Air Electrode, Advanced Materials 36 (2024) 2403998. https://doi.org/10.1002/adma.202403998.

[191] S. Zhao, W. Ma, W. Wang, Y. Huang, J. Wang, S. Wang, Z. Shu, B. He, L. Zhao, Reverse Atom Capture on Perovskite Surface Enabling Robust and Efficient Cathode for Protonic Ceramic Fuel Cells, Advanced Materials 36 (2024) 2405052. https://doi.org/10.1002/adma.202405052.

[192] E. Vøllestad, R. Strandbakke, M. Tarach, D. Catalán-Martínez, M.-L. Fontaine, D. Beeaff, D.R. Clark, J.M. Serra, T. Norby, Mixed proton and electron conducting double perovskite anodes for stable and efficient tubular proton ceramic electrolysers, Nat. Mater. 18 (2019) 752–759. https://doi.org/10.1038/s41563-019-0388-2.

[193] T. Schober, Water vapor solubility and electrochemical characterization of the high temperature proton conductor $BaZr_{0.9}Y_{0.1}O_{2.95}$, Solid State Ionics 127 (2000) 351–360. https://doi.org/10.1016/S0167-2738(99)00283-0.

[194] J.T.S. Irvine, D.C. Sinclair, A.R. West, Electroceramics: Characterization by Impedance Spectroscopy, Advanced Materials 2 (1990) 132–138. https://doi.org/10.1002/adma.19900020304.

[195] S.M. Haile, D.L. West, J. Campbell, The role of microstructure and processing on the proton conducting properties of gadolinium-doped barium cerate, J. Mater. Res. 13 (1998) 1576–1595. https://doi.org/10.1557/JMR.1998.0219.

[196] X. Li, B. Bhushan, A review of nanoindentation continuous stiffness measurement technique and its applications, Materials Characterization 48 (2002) 11–36. https://doi.org/10.1016/S1044-5803(02)00192-4.

[197] K.T. Jacob, S. Raj, L. Rannesh, Vegard's law: a fundamental relation or an approximation?, International Journal of Materials Research 98 (2007) 776–779. https://doi.org/10.3139/146.101545.

[198] G. Heras-Juaristi, D. Pérez-Coll, G.C. Mather, Temperature dependence of partial conductivities of the $BaZr_{0.7}Ce_{0.2}Y_{0.1}O_{3-\delta}$ proton conductor, Journal of Power Sources 364 (2017) 52–60. https://doi.org/10.1016/j.jpowsour.2017.08.011.

[199] M.E. Björketun, P.G. Sundell, G. Wahnström, Effect of acceptor dopants on the proton mobility in $BaZrO_3$: A density functional investigation, Phys. Rev. B 76 (2007) 054307. https://doi.org/10.1103/PhysRevB.76.054307.

[200] K. Toyoura, W. Meng, D. Han, T. Uda, Preferential proton conduction along a three-dimensional dopant network in yttrium-doped barium zirconate: a first-principles study, J. Mater. Chem. A 6 (2018) 22721–22730. https://doi.org/10.1039/C8TA08283A.

[201] K. Toyoura, T. Fujii, N. Hatada, D. Han, T. Uda, Carrier–Carrier Interaction in Proton-Conducting Perovskites: Carrier Blocking vs Trap-Site Filling, J. Phys. Chem. C 123 (2019) 26823–26830. https://doi.org/10.1021/acs.jpcc.9b08199.

[202] M. Shirpour, B. Rahmati, W. Sigle, P.A. Van Aken, R. Merkle, J. Maier, Dopant Segregation and Space Charge Effects in Proton-Conducting $BaZrO_3$ Perovskites, J. Phys. Chem. C 116 (2012) 2453–2461. https://doi.org/10.1021/jp208213x.

[203] M. Shirpour, G. Gregori, L. Houben, R. Merkle, J. Maier, High spatially resolved cation concentration profile at the grain boundaries of Sc-doped $BaZrO_3$, Solid State Ionics 262 (2014) 860–864. https://doi.org/10.1016/j.ssi.2013.11.032.

[204] M. Kindelmann, S. Escolastico, L. Almar, A. Vayyala, D. Jennings, W. Deibert, W.A. Meulenberg, W. Rheinheimer, M. Bram, J.M. Serra, J. Mayer, O. Guillon, Highly conductive grain boundaries in cold-sintered barium zirconate-based proton conductors, J. Mater. Chem. A 12 (2024) 3977–3988. https://doi.org/10.1039/D3TA07076J.

[205] M. Kindelmann, I. Povstugar, S. Kuffer, D. Jennings, J.N. Ebert, M.L. Weber, M.P. Zahler, S. Escolastico, L. Almar, J.M. Serra, P. Kaghazchi, M. Bram, W. Rheinheimer, J. Mayer, O. Guillon, Controlling Grain Boundary Segregation to Tune the Conductivity of Ceramic Proton Conductors, Advanced Energy Materials 15 (2025) 2404410. https://doi.org/10.1002/aenm.202404410.

[206] D.R. Clark, D.R. Diercks, S. Ricote, T. Tauer Dearden, N.P. Sullivan, J.W. Medlin, B.P. Gorman, R.P. O'Hayre, Understanding the effects of fabrication process on $BaZr_{0.9}Y_{0.1}O_{3-\delta}$ grain-boundary chemistry using atom probe tomography, J. Mater. Chem. C 11 (2023) 5082–5091. https://doi.org/10.1039/D2TC04093J.

[207] H.-W. Kim, J. Seo, J.H. Yu, K.S. Yun, J.H. Joo, J. Moon, H.J. Park, Effect of cerium on yttrium-doped barium zirconate with a ZnO sintering aid: Grain and grain boundary protonic conduction, Ceramics International 47 (2021) 32720–32726. https://doi.org/10.1016/j.ceramint.2021.08.168.

[208] S. Ricote, N. Bonanos, Enhanced sintering and conductivity study of cobalt or nickel doped solid solution of barium cerate and zirconate, Solid State Ionics 181 (2010) 694–700. https://doi.org/10.1016/j.ssi.2010.04.007.

[209] D. Han, X. Liu, T.S. Bjørheim, T. Uda, Yttrium‐Doped Barium Zirconate‐Cerate Solid Solution as Proton Conducting Electrolyte: Why Higher Cerium Concentration Leads to Better Performance for Fuel Cells and Electrolysis Cells, Advanced Energy Materials 11 (2021) 2003149. https://doi.org/10.1002/aenm.202003149.

[210] F. Iguchi, K. Hinata, High-Temperature Elastic Properties of Yttrium-Doped Barium Zirconate, Metals 11 (2021) 968. https://doi.org/10.3390/met11060968.

[211] E. Makagon, R. Merkle, J. Maier, I. Lubomirsky, Influence of hydration and dopant ionic radius on the elastic properties of $BaZrO_3$, Solid State Ionics 344 (2020) 115130. https://doi.org/10.1016/j.ssi.2019.115130.

[212] R. Chaim, M. Hefetz, Effect of grain size on elastic modulus and hardness of nanocrystalline ZrO_2-3 wt% Y_2O_3 ceramic, Journal of Materials Science 39 (2004) 3057–3061. https://doi.org/10.1023/B:JMSC.0000025832.93840.b0.

[213] T.Yu. Sablina, I.N. Sevostyanova, G.V. Shlyakhova, Influence of the Grain Size of $ZrO_2(Y_2O_3)$ Ceramics on the Hardness, Fracture Toughness and Formation of a Transformation-Deformation Relief in the Indentation Zone, Russ Phys J 65 (2022) 635–642. https://doi.org/10.1007/s11182-022-02679-1.

[214] H. Matsumoto, Y. Kawasaki, N. Ito, M. Enoki, T. Ishihara, Relation Between Electrical Conductivity and Chemical Stability of $BaCeO_3$-Based Proton Conductors with Different Trivalent Dopants, (n.d.) 5.

[215] Á. Triviño-Peláez, D. Pérez-Coll, J. Mosa, C. Ritter, U. Amador, G.C. Mather, Enhanced proton conductivity and stability of Ba-deficient $BaCe_{0.8}Y_{0.2}O_{3-\delta}$, Journal of Power Sources 493 (2021) 229691. https://doi.org/10.1016/j.jpowsour.2021.229691.

[216] J.N. Ebert, D. Jennings, W.S. Scheld, D. Sebold, W. Rheinheimer, Influence of Ba non-stoichiometry on the processing properties of Y- and Sc-doped BaZrO3, Journal of the European Ceramic Society 44 (2024) 6995–7005. https://doi.org/10.1016/j.jeurceramsoc.2024.04.070.

[217] E. Ryshkewitch, Compression Strength of Porous Sintered Alumina and Zirconia: 9th Communication to Ceramography, Journal of the American Ceramic Society 36 (1953) 65–68. https://doi.org/10.1111/j.1151-2916.1953.tb12837.x.

[218] R.M. Spriggs, Expression for Effect of Porosity on Elastic Modulus of Polycrystalline Refractory Materials, Particularly Aluminum Oxide, Journal of the American Ceramic Society 44 (1961) 628–629. https://doi.org/10.1111/j.1151-2916.1961.tb11671.x.

[219] J.B. Wachtman, W.R. Cannon, M.J. Matthewson, Mechanical Properties of Ceramics, 1st ed., Wiley, 2009. https://doi.org/10.1002/9780470451519.

[220] W. Weibull 1887-1979, A statistical theory of the strength of materials, Stockholm, Generalstabens litografiska anstalts förlag, Sweden, 1939. https://searchworks.stanford.edu/view/1150953.

[221] R. Sažinas, M.-A. Einarsrud, T. Grande, Toughening of Y-doped $BaZrO_3$ proton conducting electrolytes by hydration, J. Mater. Chem. A 5 (2017) 5846–5857. https://doi.org/10.1039/C6TA11022C.

[222] Z. Wang, Y. Jing, Y. Sun, W. Li, J. Yang, X. Li, Hydration induced mechanical degradation in the Y-doped $BaZrO_3$ solid oxide, Computational Materials Science 235 (2024) 112824. https://doi.org/10.1016/j.commatsci.2024.112824.

[223] Q. Wang, T. Luo, Y. Tong, M. Dai, X.-Y. Miao, S. Ricote, Z. Zhan, M. Chen, Large-area protonic ceramic cells for hydrogen purification, Separation and Purification Technology 295 (2022) 121301. https://doi.org/10.1016/j.seppur.2022.121301.

[224] H. Zhang, Y. Zhou, K. Pei, Y. Pan, K. Xu, Y. Ding, B. Zhao, K. Sasaki, Y. Choi, Y. Chen, M. Liu, An efficient and durable anode for ammonia protonic ceramic fuel cells, Energy Environ. Sci. 15 (2022) 287–295. https://doi.org/10.1039/D1EE02158C.

[225] K. Leonard, M.E. Ivanova, A. Weber, W. Deibert, W.A. Meulenberg, T. Ishihara, H. Matsumoto, Anode supported planar 5 × 5 cm^2 $SrZr_{0.5}Ce_{0.4}Y_{0.1}O_{2.95}$ based solid oxide protonic fuel cells via sequential tape-casting, Solid State Ionics 379 (2022) 115918. https://doi.org/10.1016/j.ssi.2022.115918.

[226] S.M. Choi, H. An, K.J. Yoon, B.-K. Kim, H.-W. Lee, J.-W. Son, H. Kim, D. Shin, H.-I. Ji, J.-H. Lee, Electrochemical analysis of high-performance protonic ceramic fuel cells based on a columnar-structured thin electrolyte, Applied Energy 233–234 (2019) 29–36. https://doi.org/10.1016/j.apenergy.2018.10.043.

[227] S.M. Choi, J.-H. Lee, H.I. Ji, K.J. Yoon, J.-W. Son, B.-K. Kim, H.J. Je, H.-W. Lee, J.-H. Lee, Fabrication and characterization of $Ba(Zr_{0.84}Y_{0.15}Cu_{0.01})O_3$ electrolyte-based protonic ceramic fuel cells, Ceramics International 39 (2013) 9605–9611. https://doi.org/10.1016/j.ceramint.2013.05.081.

[228] Z. Huang, Y. Yang, H. Lv, C. Shi, T. Li, Y. Ling, T. Chen, S. Wang, Large-area anode-supported protonic ceramic fuel cells combining with multilayer-tape casting and hot-pressing lamination technology, Journal of the European Ceramic Society 43 (2023) 428–437. https://doi.org/10.1016/j.jeurceramsoc.2022.09.057.

[229] Y. Ma, J. Huang, B. He, Scalable fabrication process for new structure $BaZr_{0.8}Y_{0.2}O_{3-\delta}$-based protonic ceramic fuel cells, Ceramics International 47 (2021) 14680–14688. https://doi.org/10.1016/j.ceramint.2021.01.264.

[230] J. Xiao, L. Chen, H. Yuan, L. Ji, C. Xiong, J. Ma, X. Zhu, Fabrication and characterization of $BaZr_{0.1}Ce_{0.7}Y_{0.2}O_{3-\delta}$ based anode supported solid oxide fuel cells by tape casting combined with spray coating, Materials Letters 189 (2017) 192–195. https://doi.org/10.1016/j.matlet.2016.10.114.

[231] W. Zhou, H. Shi, R. Ran, R. Cai, Z. Shao, W. Jin, Fabrication of an anode-supported yttria-stabilized zirconia thin film for solid-oxide fuel cells via wet powder spraying, Journal of Power Sources 184 (2008) 229–237. https://doi.org/10.1016/j.jpowsour.2008.06.021.

[232] J. Dailly, G. Taillades, M. Ancelin, P. Pers, M. Marrony, High performing $BaCe_{0.8}Zr_{0.1}Y_{0.1}O_{3-\delta}$-$Sm_{0.5}Sr_{0.5}CoO_{3-\delta}$ based protonic ceramic fuel cell, Journal of Power Sources 361 (2017) 221–226. https://doi.org/10.1016/j.jpowsour.2017.06.089.

[233] Y. Yoo, N. Lim, Performance and stability of proton conducting solid oxide fuel cells based on yttrium-doped barium cerate-zirconate thin-film electrolyte, Journal of Power Sources 229 (2013) 48–57. https://doi.org/10.1016/j.jpowsour.2012.11.094.

[234] E. Schüller, R. Vaßen, D. Stöver, Thin Electrolyte Layers for SOFC via Wet Powder Spraying (WPS), Adv. Eng. Mater. 4 (2002) 659–662. https://doi.org/10.1002/1527-2648(20020916)4:9<659::AID-ADEM659>3.0.CO;2-I.

[235] H. Shi, R. Ran, Z. Shao, Wet powder spraying fabrication and performance optimization of IT-SOFCs with thin-film ScSZ electrolyte, International Journal of Hydrogen Energy 37 (2012) 1125–1132. https://doi.org/10.1016/j.ijhydene.2011.02.077.

[236] A. Moorhead, L.F. Francis, Characterizing stress development and cracking of ceramic particulate coatings during drying, J Am Ceram Soc. 107 (2024) 2837–2848. https://doi.org/10.1111/jace.19644.

[237] R.C. Chiu, M.J. Cima, Drying of Granular Ceramic Films: II, Drying Stress and Saturation Uniformity, Journal of the American Ceramic Society 76 (1993) 2769–2777. https://doi.org/10.1111/j.1151-2916.1993.tb04014.x.

[238] R.C. Chiu, T.J. Garino, M.J. Cima, Drying of Granular Ceramic Films: I, Effect of Processing Variables on Cracking Behavior, Journal of the American Ceramic Society 76 (1993) 2257–2264. https://doi.org/10.1111/j.1151-2916.1993.tb07762.x.

[239] H. An, S. Im, J. Kim, B.-K. Kim, J.-W. Son, K. Joong, H. Kim, S. Yang, H. Kang, J.-H. Lee, H.-I. Ji, An unprecedented vapor-phase sintering activator for highly refractory proton conducting oxides, (n.d.).

[240] H. An, S. Im, J. Kim, B.-K. Kim, J.-W. Son, K.J. Yoon, H. Kim, S. Yang, H. Kang, J.-H. Lee, H.-I. Ji, An Unprecedented Vapor-Phase Sintering Activator for Highly Refractory Proton-Conducting Oxides, ACS Energy Lett. 7 (2022) 4036–4044. https://doi.org/10.1021/acsenergylett.2c02059.

[241] M. Kindelmann, J.N. Ebert, W.S. Scheld, W. Deibert, W.A. Meulenberg, W. Rheinheimer, M. Bram, J. Mayer, O. Guillon, Cold sintering of $BaZr_{0.7}Ce_{0.2}Y_{0.1}O_{3-\delta}$ ceramics by controlling the phase composition of the starting powders, Scripta Materialia 224 (2023) 115147. https://doi.org/10.1016/j.scriptamat.2022.115147.

[242] Y. Huang, R. Merkle, J. Maier, Effects of NiO addition on sintering and proton uptake of $Ba(Zr,Ce,Y)O_{3-\delta}$, J. Mater. Chem. A 9 (2021) 14775–14785. https://doi.org/10.1039/D1TA02555D.

[243] S. M. Choi, J. H. Lee, J. Hong, H. Kim, K. J. Yoon, B. K. Kim, J. H. Lee, Effect of sintering atmosphere on phase stability, and electrical conductivity of proton-conducting Ba $(Zr_{0.84}Y_{0.15}Cu_{0.01})O_{3-\delta}$. International Journal of Hydrogen Energy, 39(2014), 7100-7108. https://doi.org/10.1016/j.ijhydene.2014.02.072.

[244] Z. Liu, X. Wang, M. Liu, J. Liu, Enhancing sinterability and electrochemical properties of $Ba(Zr_{0.1}Ce_{0.7}Y_{0.2})O_{3-\delta}$ proton conducting electrolyte for solid oxide fuel cells by addition of NiO, International Journal of Hydrogen Energy 43 (2018) 13501–13511. https://doi.org/10.1016/j.ijhydene.2018.05.089.

[245] Exploring the impact of sintering additives on the densification and conductivity of $BaCe_{0.3}Zr_{0.55}Y_{0.15}O_{3-\delta}$ electrolyte for protonic ceramic fuel cells.pdf, (n.d.).

[246] Á. Triviño-Peláez, D. Pérez-Coll, M. Aparicio, D.P. Fagg, J. Mosa, G.C. Mather, Processing and characterisation of $BaZr_{0.8}Y_{0.2}O_{3-\delta}$ proton conductor densified at 1200 °C, J. Mater. Chem. A 10 (2022) 4428–4439. https://doi.org/10.1039/D1TA09998A.

[247] Proton Conductive $BaZr_{0.8-x}Ce_xY_{0.2}O_{3-\delta}$ Influence of NiO Sintering Additive on Crystal Structure, Hydration Behavior, and Conduction Properties.pdf, (n.d.).

[248] S. Imashuku, T. Uda, Y. Awakura, Sintering Properties of Trivalent Cation-Doped Barium Zirconate at 1600°C, Electrochem. Solid-State Lett. 10 (2007) B175. https://doi.org/10.1149/1.2766530.

[249] D. Gao, R. Guo, Structural and electrochemical properties of yttrium-doped barium zirconate by addition of CuO, Journal of Alloys and Compounds 493 (2010) 288–293. https://doi.org/10.1016/j.jallcom.2009.12.082.

[250] V.C.D. Graça, F.J.A. Loureiro, L.I.V. Holz, S.M. Mikhalev, D.P. Fagg, Toward improved chemical stability of yttrium-doped barium cerate by the introduction of nickel oxide, Journal of the American Ceramic Society n/a (n.d.). https://doi.org/10.1111/jace.18600.

[251] S. Wang, L. Zhang, L. Zhang, K. Brinkman, F. Chen, Two-step sintering of ultrafine-grained barium cerate proton conducting ceramics, Electrochimica Acta 87 (2013) 194–200. https://doi.org/10.1016/j.electacta.2012.09.007.

[252] M. Choi, J. Paik, D. Kim, D. Woo, J. Lee, S.J. Kim, J. Lee, W. Lee, Exceptionally high performance of protonic ceramic fuel cells with stoichiometric electrolytes, Energy Environ. Sci. 14 (2021) 6476–6483. https://doi.org/10.1039/D1EE01497H.

[253] Z. Liu, Y. Song, X. Xiong, Y. Zhang, J. Cui, J. Zhu, L. Li, J. Zhou, C. Zhou, Z. Hu, G. Kim, F. Ciucci, Z. Shao, J.-Q. Wang, L. Zhang, Sintering-induced cation displacement in protonic ceramics and way for its suppression, Nat Commun 14 (2023) 7984. https://doi.org/10.1038/s41467-023-43725-x.

[254] J. Li, C. Wang, X. Wang, L. Bi, Sintering aids for proton-conducting oxides – A double-edged sword? A mini review, Electrochemistry Communications 112 (2020) 106672. https://doi.org/10.1016/j.elecom.2020.106672.

[255] Y.-D. Kim, I.-H. Kim, C. Meisel, C. Herradón, P.W. Rand, J. Yang, H.S. Kim, N.P. Sullivan, R. O'Hayre, Improving tubular protonic ceramic fuel cell performance by compensating Ba evaporation via a Ba-excess optimized proton conducting electrolyte synthesis strategy, J. Phys. Energy 6 (2024) 035004. https://doi.org/10.1088/2515-7655/ad5760.

[256] R. Wang, G.Y. Lau, D. Ding, T. Zhu, M.C. Tucker, Approaches for co-sintering metal-supported proton-conducting solid oxide cells with $Ba(Zr,Ce,Y,Yb)O_{3-\delta}$ electrolyte, International Journal of Hydrogen Energy 44 (2019) 13768–13776. https://doi.org/10.1016/j.ijhydene.2019.03.181.

[257] H. Tong, M. Fu, Y. Yang, F. Chen, Z. Tao, A Novel Self‐Assembled Cobalt‐Free Perovskite Composite Cathode with Triple‐Conduction for Intermediate Proton‐Conducting Solid Oxide Fuel Cells, Adv Funct Materials 32 (2022) 2209695. https://doi.org/10.1002/adfm.202209695.

[258] W. Bian, W. Wu, B. Wang, W. Tang, M. Zhou, C. Jin, H. Ding, W. Fan, Y. Dong, J. Li, D. Ding, Revitalizing interface in protonic ceramic cells by acid etch, Nature 604 (2022) 479–485. https://doi.org/10.1038/s41586-022-04457-y.

[259] H. Tian, W. Li, Y.-L. Lee, H. Zheng, Q. Li, L. Ma, D. Bhattacharyya, X. Chen, D. Zhang, G. Li, Y. Wang, L. Li, Q. Wang, F. Xia, M. Kartal, Z. Shao, M.R. Rowles, W. Li, W.A. Saidi, C. Liu, X. Li, J. Luo, X. Li, K. He, X. Liu, Conformally coated scaffold design using water-tolerant $Pr_{1.8}Ba_{0.2}NiO_{4.1}$ for protonic ceramic electrochemical cells with 5,000-h electrolysis stability, Nat Energy (2025). https://doi.org/10.1038/s41560-025-01800-1.

[260] H. Gao, F. He, F. Zhu, J. Xia, Z. Du, Y. Huang, L. Zhu, Y. Chen, Effective Promotion of the Activity and Stability of Cathodes for Protonic Ceramic Fuel Cells, Adv Funct Materials 34 (2024) 2401747. https://doi.org/10.1002/adfm.202401747.

[261] N. Lu, Z. Zhang, Y. Wang, H.-B. Li, S. Qiao, B. Zhao, Q. He, S. Lu, C. Li, Y. Wu, M. Zhu, X. Lyu, X. Chen, Z. Li, M. Wang, J. Zhang, S.C. Tsang, J. Guo, S. Yang, J. Zhang, K. Deng, D. Zhang, J. Ma, J. Ren, Y. Wu, J. Zhu, S. Zhou, Y. Tokura, C.-W. Nan, J. Wu, P. Yu, Enhanced low-temperature proton conductivity in hydrogen-intercalated brownmillerite oxide, Nat Energy 7 (2022) 1208–1216. https://doi.org/10.1038/s41560-022-01166-8.

[262] Y. Chen, B. deGlee, Y. Tang, Z. Wang, B. Zhao, Y. Wei, L. Zhang, S. Yoo, K. Pei, J.H. Kim, Y. Ding, P. Hu, F.F. Tao, M. Liu, A robust fuel cell operated on nearly dry methane at 500 °C enabled by synergistic thermal catalysis and electrocatalysis, Nat Energy 3 (2018) 1042–1050. https://doi.org/10.1038/s41560-018-0262-5.

[263] K. Leonard, Y. Okuyama, Y. Takamura, Y.-S. Lee, K. Miyazaki, M.E. Ivanova, W.A. Meulenberg, H. Matsumoto, Efficient intermediate-temperature steam electrolysis with Y : $SrZrO_3$ –$SrCeO_3$ and Y : $BaZrO_3$ –$BaCeO_3$ proton conducting perovskites, J. Mater. Chem. A 6 (2018) 19113–19124. https://doi.org/10.1039/C8TA04019B.

[264] K.-R. Lee, C.-J. Tseng, J.-K. Chang, I.-M. Hung, J.-C. Lin, S.-W. Lee, Strontium doping effect on phase homogeneity and conductivity of $Ba_{1-x}Sr_xCe_{0.6}Zr_{0.2}Y_{0.2}O_{3-\delta}$ proton-conducting oxides, International Journal of Hydrogen Energy 38 (2013) 11097–11103. https://doi.org/10.1016/j.ijhydene.2013.01.043.

[265] J. Madhuri Sailaja, N. Murali, K. Vijay Babu, V. Veeraiah, Effect of Strontium the phase structure of $Ba_{1-x}Sr_xCe_{0.65}Zr_{0.2}Y_{0.15}O_{3-\delta}$ ($0 \leqslant x \leqslant 0.25$) proton conductor by citrate‐EDTA complexing sol‐gel method, Journal of Asian Ceramic Societies 5 (2017) 18‐30. https://doi.org/10.1016/j.jascer.2016.12.004.

[266] J.N. Ebert, D. Jennings, W.S. Scheld, D. Sebold, W. Rheinheimer, Influence of Ba non-stoichiometry on the processing properties of Y- and Sc-doped $BaZrO_3$, Journal of the European Ceramic Society 44 (2024) 6995–7005. https://doi.org/10.1016/j.jeurceramsoc.2024.04.070.

[267] M. Kindelmann, I. Povstugar, S. Kuffer, D. Jennings, J.N. Ebert, M.L. Weber, M.P. Zahler, S. Escolastico, L. Almar, J.M. Serra, P. Kaghazchi, M. Bram, W. Rheinheimer, J. Mayer, O. Guillon, Controlling Grain Boundary Segregation to Tune the Conductivity of Ceramic Proton Conductors, Advanced Energy Materials (2024) 2404410. https://doi.org/10.1002/aenm.202404410.

[268] K. Leonard, Y.-S. Lee, Y. Okuyama, K. Miyazaki, H. Matsumoto, Influence of dopant levels on the hydration properties of SZCY and BZCY proton conducting ceramics for

hydrogen production, International Journal of Hydrogen Energy 42 (2017) 3926–3937. https://doi.org/10.1016/j.ijhydene.2016.10.120.

[269] M. Zhou, Z. Liu, M. Chen, Z. Zhu, D. Cao, J. Liu, Electrochemical performance and chemical stability of proton‐conducting $BaZr_{0.8-x}Ce_xY_{0.2}O_{3-\delta}$ electrolytes, J Am Ceram Soc. (2022) jace.18500. https://doi.org/10.1111/jace.18500.

[270] R. Strandbakke, E. Vøllestad, S.A. Robinson, M.-L. Fontaine, T. Norby, $Ba_{0.5}Gd_{0.8}La_{0.7}Co_2O_{6-\delta}$ Infiltrated in Porous $BaZr_{0.7}Ce_{0.2}Y_{0.1}O_3$ Backbones as Electrode Material for Proton Ceramic Electrolytes, J. Electrochem. Soc. 164 (2017) F196–F202. https://doi.org/10.1149/2.0141704jes.

[271] R. Strandbakke, V.A. Cherepanov, A.Yu. Zuev, D.S. Tsvetkov, C. Argirusis, G. Sourkouni, S. Prünte, T. Norby, Gd- and Pr-based double perovskite cobaltites as oxygen electrodes for proton ceramic fuel cells and electrolyser cells, Solid State Ionics 278 (2015) 120–132. https://doi.org/10.1016/j.ssi.2015.05.014.

9.2 List of Abbreviation

BLC $Ba_{0.5}La_{0.5}CoO_{3-\delta}$

BSE Backscattered electrons

BZCY Y doped Ba(Zr, Ce)O3

BZCYYb $BaZr_{0.16}Ce_{0.64}Y_{0.1}Yb_{0.1}O_3$

CPE Constant phase element

EDS Energy Dispersive X-ray Spectroscopy

EIS Electrochemical Impedance Spectroscopy

FIB Focused ion beam

HAADF High-angle annular dark-field

I Current

OCV Open Circuit Voltage

P Power density

PCC(s) Proton-Conducting Ceramic Cell(s)

PCFC Protonic Ceramic Fuel Cell

PCEC Protonic Ceramic Electrolysis Cell

PSD Particle size distribution

R Resistor

SEM Scanning Electron Microscopy

SG Sol–gel

SOC(s) Solid Oxide Cell(s)

SOEC Solid Oxide Electrolysis Cell

SOFC Solid Oxide Fuel Cell

SSR(S) Solid-state reaction (sintering)

STEM Scanning Transmission Electron Microscopy

SZCY $SrZr_{0.5}Ce_{0.4}Y_{0.1}O_{3-\delta}$

TEM Transmission Electron Microscopy

TGA Thermogravimetric analysis

V Voltage

WPS Wet Powder Spraying

XRD X-ray diffraction

YSZ Yttria-Stabilized Zirconia

9.3 List of Figures

9.4 List of Table

9.5 Acknowledgement

This work was financially supported by the Chinese Scholarship Council (CSC) and the Helmholtz Research Program Materials and Technologies for the Energy Transition (MTET), whose support is gratefully acknowledged.

I would first like to express my deepest gratitude to my supervisor and 'Doktorvater', Prof. Norbert H. Menzler, for his invaluable guidance, patience, and encouragement throughout my doctoral studies. His scientific insight and academic rigor have been an inspiration to me.

My sincere thanks go to Dr. Mariya Ivanova for her direct guidance in the laboratory, for her support in scientific discussion and paper revision, and for her kind assistance in my daily life. I am also deeply grateful to Dr. Jürgen Malzbender for providing expertise and guidance in the mechanical property measurements, and to Prof. Matsumoto Hiroshige and Prof. Kwati Leonard from Kyushu University for hosting my three-month research stay in Japan and for their guidance in the electrochemical testing of full cells. I would also like to thank Prof. Olivier Guillon for his academic support.

I extend my appreciation to my colleagues at IMD for their valuable experimental assistance, theoretical discussions, and technical guidance: Laura Schäfer (laboratory guidance and scientific discussion), Dr. Christian Lenser (EIS and scientific discussion), Dr. Moritz Kindelmann (TEM characterization and scientific discussion), Kai Yao (scientific discussion), Volker Bader (sintering of numerous samples over the past four years), Marie Theres Gerhards (TGA measurements), Jan-Philipp Treitz (laboratory procurement and support in WPS experiments), Dr. Yoo Jung Sohn (XRD characterization and scientific discussion), Dr. Doris Sebold (SEM characterization), Ralf Kauert (guidance in tape casting), Andrea Hilgers (PSD measurements), Dr. Michael Müller (thermo-chemical stability tests), Tatjana Osipova (ring-on-ring bending tests).

My heartfelt thanks also go to the warm and supportive members of the IMD-SOC group: Denise Ramler, Martin Hilger, Dr. Christian Dellen, Suraj R. Chamakura, Werner Herzhof, Dr. Stefan Kucharski, Severin Kuffer, Nantje Kügler, Irmgard Mingers, Stephan Sarner, Franziska Winterhalder, Yavuz Selim Ayhan, Muhammad Shirjeel Khan, Shivam Kumar Dwivedi, for their assistance both in the laboratory and in daily life. I am equally grateful to my Chinese colleagues at IMD-2, Dr. Qianli Ma, Ruijie Ye, Dapeng Zhou, Wenyu Zhou, Huiyu Zhang, Xiaochen Liu, Fanlin Zeng, Yiming Guo, for their help and companionship.

I owe my deepest gratitude to my parents, for nearly thirty years of unconditional love, guidance, and support in all my decisions. Most of all, I wish to thank my life partner, my gentle harbor, and my

greatest source of strength, my wife, Caiyun Gao, for her endless patience, for accepting all my negative emotions, and for sharing every joy with me.

During my doctoral journey, the world witnessed the COVID-19 pandemic, the Russia–Ukraine conflict, and the Israel–Palestine conflict. In closing, I sincerely hope for a future where peace prevails, free from the shadows of war and disease.

Band / Volume 688
Model Perovskite Oxide Electrocatalysts for the Oxygen Evolution Reaction and their Material Sustainability Evaluation
L. Heymann (2026), vi, 174 pp
ISBN: 978-3-95806-878-0

Band / Volume 689
Development of an oxygen ion conducting solid oxide electrolysis cell based on gadolinium-doped cerium oxide as fuel electrode and electrolyte material
D. Ramler (2026), ix, 162 pp
ISBN: 978-3-95806-879-7

Band / Volume 690
Design of Local Multi-Energy Systems: Impact of Coupled Energy Vector Integration and Grid Service Participation
P. S. Glücker (2026), xxviii, 145 pp
ISBN: 978-3-95806-880-3

Band / Volume 691
A Parallel-in-Space Simulator for Accelerating Power System Simulation on Graphics Processing Units
J. Zhang (2026), 112 pp
ISBN: 978-3-95806-882-7

Band / Volume 692
Entwicklung von Reparaturmethoden für einkristalline Bauteile mittels thermischer Spritzverfahren
M. L. Létang (2026), X, 211 pp
ISBN: 978-3-95806-883-4

Band / Volume 693
Assessing the Environmental Implications of Offshore Wind Energy Advancements on the Future German Electricity Sector
A. Benitez (2026), xi, 176 pp
ISBN: 978-3-95806-885-8

Band / Volume 694
Entwicklung von Korrosionsschutzschichten für Protonen-Austausch-Membran-Wasserelektrolyseure
T. Sievert (2026), 201 pp
ISBN: 978-3-95806-888-9

Band / Volume 695
Hierarchical Modeling of Electrocatalytic Reactions from a Local Perspective
X. Zhu (2026), ix, 121 pp
ISBN: 978-3-95806-889-6

Band / Volume 696
Nanocrystalline Silicon Carbide in Transparent Passivating Contact Solar Cells
A. Eberst (2026), xiii, 225 pp
ISBN: 978-3-95806-891-9

Band / Volume 697
Theory of Electronic and Ionic Perturbations at Supported Electrocatalyst Nanoparticles
Y. Zhang (2026), XI, 131 pp
ISBN: 978-3-95806-896-4

Band / Volume 698
Aufbau und Einsatz eines on-board Messsystems zur Untersuchung der Abgaszusammensetzung von Fahrzeugen betrieben mit konventionellen und alternativen Kraftstoffen
V. Polinowski (2026), VIII, 269 pp
ISBN: 978-3-95806-897-1

Band / Volume 699
Ab Initio-based large-scale Atomistic Simulations of Cathode Materials for Secondary Batteries: From Computational Methodologies to Applications towards improved Structural and Chemical Stability
K. Köster (2026), x, 204, x pp
ISBN: 978-3-95806-898-8

Band / Volume 700
Materials Design, Processing and Application of Proton-Conducting Oxides for Electrochemical Energy Conversion
Y. Zeng (2026), vii, 117 pp
ISBN: 978-3-95806-899-5

Weitere ***Schriften des Verlags im Forschungszentrum Jülich*** unter
http://wwwzb1.fz-juelich.de/verlagextern1/index.asp

Energie & Umwelt / Energy & Environment
Band / Volume 700
ISBN 978-3-95806-899-5

Mitglied der Helmholtz-Gemeinschaft

JÜLICH
Forschungszentrum